N° d'ordre : 2015 ISAL 0003 Année 2015

Thèse

Conception, fabrication et caractérisation d'un microphone MEMS

(Conception, fabrication and characterization of a MEMS microphone)

Présentée devant
L'institut national des sciences appliquées de Lyon

pour obtenir
Le grade de docteur

Formation doctorale : Acoustique
École doctorale : MEGA - Mécanique, Énergétique, Génie Civil, Acoustique
Préparée au CEA Grenoble en collaboration avec le LVA de l'INSA LYON

Par

Jarosław Czarny
(Master of Science, Engineer)

Soutenue le 27 janvier devant la Commission d'examen

Jury MM.

Directeurs de thèse:	J-L. Guyader	Professeur (INSA de Lyon)
	E. Redon	Maître de Conférences (Université de Bourgogne)
Rapporteurs:	B. Dubus	Directeur de Recherche (CNRS)(IEMN)
	N. Joly	Maître de Conférences HDR (Université du Maine)
Examinateurs:	M. Collet	Directeur de Recherche (CNRS)(E. C. de Lyon)
	M. Ouisse	Professeur (ENSMM)
	T. Verdot	Docteur Ingénieur (CEA-LETI)
Invité:	A. Walther	Docteur Ingénieur (Infineon Technologies AG)

Abstract

Electret microphones dedicated to consumer electronics and medical applications (hearing aids) have reached the miniaturization limits. Since the release of the first microphone based on Silicon micromachining, electret microphones are constantly replaced by MEMS microphones. MEMS (Micro-Electro-Mechanical Systems) microphones use Silicon that provides exceptional mechanical characteristics along with good electric properties and mature fabrication technology. Regardless of the transduction principle (capacitive, piezoresistive, piezoelectric, optical), all of the MEMS microphones reported in the state of the art literature are based on a membrane deflecting out of the plane of the base wafer. Most of the reported microphones and all of the commercially available MEMS use capacitive transduction. Downscaling of capacitive microphones is problematic, since the sensitivity depends on capacitance value. Moreover capacitive sensors suffer of high sensitivity to parasitic capacitance and nonlinearity.
The drawbacks of capacitive detection may be overcome with use of piezoresistive properties of Silicon nanowires. Unlike the classical piezoresistors integrated into silicon membrane, suspended nanowires do not suffer of leakage current. Further improvement of piezoresistive detection is possible since the longitudinal piezoresistive coefficient rises inversely proportional to nanowire section.

This thesis presents the considerations of novel MEMS microphone architecture that uses microbeams which deflect in the plane of the base wafer. Signal transduction is achieved by piezoresistive nanogauges integrated in the microsystem and attached to the microbeams. Acoustic pressure fluctuations lead to the deflection of the microbeams which produces a stress concentration in the nanogauges. Accurate simulations of the discussed transducer couple acoustic, mechanical and electric behavior of the system. Due to micrometric dimensions of the MEMS acoustic system, thermal and viscous dissipative effects have to be taken into account. To reliably predict the sensor behavior two acoustic models are prepared: the complete Finite Element Model based on the full set of linearized Navier-Stokes equations and the approximative model based on the Lumped Elements (Equivalent Cirtuit Representation). Both models are complementary in the design process to finally retrieve the frequency response and the noise budget of the sensor.

The work is completed by the description of the technological process and the challenges related to the prototype microfabrication. Then the approach to the MEMS microphone characterization in pressure-field and free-field is presented.

Résumé

Les microphones à électret dédiés à l'électronique grand public et les applications médicales (les audioprothèses) ont atteint les limites de la miniaturisation. Depuis la sortie du premier microphone basé sur une technologie microsystème sur silicium (MEMS: Micro-Electro-Mechanical Systems), les microphones à électret sont progressivement remplacés par les microphones MEMS. Les MEMS utilisent le silicium car il offre des caractéristiques mécaniques exceptionnelles avec de bonnes propriétés électriques et la technologie de fabrication est maintenant bien maîtrisée. La plupart des microphones MEMS qui sont décrits dans la littérature sont constitués d'une membrane qui vibre en dehors du plan du capteur, et utilisent la transduction capacitive. La miniaturisation de tels microphones est limitée car leur sensibilité est liée à la valeur de la capacité qui dépend de la taille de la membrane. En outre, les capteurs capacitifs sont très sensibles aux capacités parasites et aux non-linéarités.

Cette thèse présente une nouvelle architecture de microphone MEMS qui utilise des micro-poutres qui vibrent dans le plan capteur. La transduction du signal est réalisée par des nanojauges piézorésistives intégrées dans le microsystème et attachées aux micro-poutres. Ce système de détection original ne présente pas les inconvénients de la détection capacitive et à la différence des piézorésistors classiques intégrés dans la membrane de silicium, les nanofils suspendus permettent d'éliminer les courants de fuite. De plus, l'amélioration de la détection est possible puisque le coefficient piézo-résistif longitudinal est inversement proportionnel à la section du nanofil.

Les fluctuations de pression acoustique entraînent les déviations des micro-poutres qui produisent une concentration de contraintes dans les nanogauges. Le comportement du capteur, que l'on cherche à modéliser, est lié à des phénomènes mécaniques, acoustiques et électriques qui sont couplés. En raison des dimensions micrométriques du MEMS, les effets des dissipations thermique et visqueuse doivent être pris en compte dans le comportement acoustique. Pour prédire de façon fiable le comportement du capteur, deux modèles vibroacoustiques sont utilisés: un modèle éléments finis basé sur l'ensemble des équations de Navier-Stokes linéarisées et un modèle approché basé sur un schéma à constantes localisées (représentation par circuit électrique équivalent). Les deux modèles sont complémentaires dans le processus de conception pour déterminer la réponse en fréquence et le taux de bruit du capteur.

Le travail est complété par la description des processus technologiques et les défis liés à la fabrication du prototype. Puis deux approches pour la caractérisation fonctionnelle du microphone MEMS sont présentées, la première en tube d'impédance, la seconde en champ libre.

Acknowledgements

First of all I would like to show my gratitude to all the people that I had a pleasure to work with during my PhD. I am very grateful that during this time I was never left alone and every arising difficulties could have been discussed with more experienced co-workers.

J'aimerais tout d'abord remercier mon directeur de thèse, Jean Louis Guyader d'avoir accepté ma candidature. Les remerciements vont aussi à Emmanuel Redon and Thierry Verdot, qui ont bien eu la gentillesse de m'avoir suporté durant ces trois années. J'ai particulièrement apprécié toutes les discussions que nous avons pu avoir et tous les conseils que je pu en tirer. Je remercie aussi Arnaud Walther, d'avoir eu confiance en moi et de m'avoir donné l'opportunité de travailler sur les microphones MEMS et d'avoir encadré mon travail durant les deux premières année de ma thèse. Il m'est important de souligner le travail du jury et de rapporteurs qui ont lu mon mémoire et ont contribué à l'évaluation de mon travail.

Je voudrais remercier à toutes les personnes travaillant à la division M&NEMS du Laboratoire Composants Micro Capteurs, pour leur travail en amont et qui a sensiblement contribué à la fabrication des microphones MEMS. Mes remerciements vont aussi à Hélène Lhermet, Brigitte Desloges et Audrey Berthelot, impliquées dans le projet MADNEMS, pour leur travail de gestion et de fabrication de microphones.

La conception des microphones n'aurait pas été possible sans le travail des personnes du Laboratoire Vibrations Acoustique à Lyon. Je leurs remercie aussi tout particulièrement, je remercie aussi Cécile Guianvarc'h, Thierry Verdot, Emmanuel Redon et Kerem Ege de m'avoir présenté les aspects d'acoustique.

Je remercie aussi tous mes collègues d'avoir mis une ambiance très positives au bureau et pour toutes les discussions qui s'avéraient très productives.

Dziękuję "polskiej rodzince" za wspólne wieczory, pikniki w parku i wycieczki.
Na koniec dziękuję najbliższym mi osobom. Bez waszego nieustającego wsparcia i dobrego słowa napisanie niniejszej pracy nie było by możliwe. Moje myśli wedrowały ku was przez całe trzy lata spędzone we Francji.

Contents

1 Introduction **1**
- 1.1 General introduction . . . 1
- 1.2 International context of this work . . . 6
- 1.3 The "MADNEMS" project . . . 13
- 1.4 Organization of the manuscript . . . 13

2 New architecture of a MEMS microphone **15**
- 2.1 Concept presentation . . . 15
- 2.2 Possible transduction mechanisms . . . 16
  - 2.2.1 Capacitive transduction . . . 16
  - 2.2.2 Piezoresistive transduction . . . 19
  - 2.2.3 Transduction mechanisms comparison . . . 22
- 2.3 The M&NEMS technology . . . 23
  - 2.3.1 Technological platform . . . 24
  - 2.3.2 M&NEMS sensors review . . . 24

Summary . . . 26

3 Models for simulations of acoustic phenomena in MEMS **27**
- 3.1 Propagation of sound wave in dissipative fluid . . . 27
- 3.2 Scaling effects in acoustics . . . 29
- 3.3 Full Linearized Navier-Stokes model (FLNS) . . . 32
  - 3.3.1 Boundary conditions . . . 32
  - 3.3.2 Problem formulation . . . 33
  - 3.3.3 Solving method . . . 35
  - 3.3.4 Means of FLNS model enhancement . . . 36
- 3.4 Low Reduced Frequency model (LRF) . . . 37
  - 3.4.1 Problem formulation . . . 38
- 3.5 Benchmarking . . . 41
  - 3.5.1 Finite Element Models based on Linearized Navier-Stokes equations (LNS) . . . 42
  - 3.5.2 Low Reduced Frequency model . . . 43
  - 3.5.3 Results discussion . . . 45
- 3.6 Towards Lumped Element model . . . 48
  - 3.6.1 Validation of Lumped Element model . . . 48
  - 3.6.2 Acoustic resistance of rectangular guide . . . 49

Summary . . . 51

4 Sensor design considerations **52**
4.1 Architecture properties of considered MEMS . . . 52
4.2 Transduction chain - assemble of the microphone subsystems . . . 56
4.3 2D finite element analysis of MEMS with fluid-structure interaction . . 57
4.3.1 Structure of the model . . . 57
4.3.2 Discussion on the MEMS chip acoustic properties . . . 59
4.3.3 Influence of MEMS chip-scale packaging on the microphone response 63
4.4 Detailed discussion on the mechanical system . . . 66
4.4.1 Analytical model . . . 66
4.4.2 FEM model . . . 68
4.5 Truss structured beam - from 3D to 2D simulations . . . 72
4.6 Electrical system transfer function . . . 76
4.7 Sensitivity . . . 76
4.8 Noise budget . . . 78
4.8.1 Origins of the noises . . . 78
4.8.2 Equivalent circuit representation of the microphone for the noise budgeting . . . 81
4.8.3 Total transduction chain noise . . . 83
4.9 Influence of overetch on the microphone response . . . 85
4.10 Tolerance to mechanical shocks and sound pressure overload . . . 87
Summary of sensor specifications and discussion . . . 89

5 Technological implementation **92**
5.1 Process flow . . . 92
5.2 Advances and difficulties encountered in microfabrication . . . 95
5.3 Out-of-plane deflection of MEMS . . . 96
5.4 Chip scale packaging . . . 98
5.4.1 Technology overview . . . 98
5.4.2 Proposed solution . . . 102
Summary . . . 104

6 Approach to MEMS microphone calibration **105**
6.1 Selection of suitable calibration methods . . . 105
6.2 Specimen description . . . 106
6.3 Influence of experimental setup on microphone response . . . 108
6.4 Pressure-field investigations with use of impedance tube . . . 110
6.4.1 Pressure-field experimental setup and measurements . . . 112
6.5 Free-field investigations in anechoic chamber . . . 115
Summary . . . 118

Conclusion and outlook **119**

A How COMSOL implements FLNS **121**

Bibliography **122**

Chapter 1

Introduction

1.1 General introduction

Origins of microphones dates XIX century [1], research in this area was accelerated by need of convenient and fast means of long distance communication. If we consider microphone as a electroacoustic transducer, its development dates down to 1874 when patent of E.W. Siemens on magneto-electric apparatus [2] was granted. However the invention of Siemens was not applied to microphone until late 1920's and in a meanwhile, in 1876 A.G. Bell has used liquid transmitter microphone in his telephone. Further designs of telephones used carbon microphone presented in 1877 by T.A. Edison [3]. Condenser microphone (which is the most common type in daily use) was invented by E.C. Wente [4] in 1916 and improved by G. Sessler and J. West [5] in 1960 by integration of electret material. The first commercial MEMS[1] microphone was presented in 2002 by Knowles - nearly 20 years after the report of first working condenser microphone based on silicon micromachining by G. Sessler and D. Hohm in 1983 [6].

- 1874 - E.W. Siemens patent on magneto-electric apparatus was granted,
- 1876 - A.G. Bell patent entitled "Improvement in Telegraphy" [7],
- 1877 - T.A. Edison invents carbon microphone,
- 1916 - E.C. Wente invents first stable and commercially viable condenser microphone,
- 1960 - Invention of Electret Condenser Microphone (ECM) by G. Sessler and J. West of Bell Labs,
- 1983 - G. Sessler and D. Hohm fabricates the first working silicon condenser microphone based on bulk machining of silicon,
- 2002 - Knowles releases the SiSonic - first commercial MEMS microphone.

Principle of operation

Microphone is an instrument that transduces acoustic waves into electrical signal, it operates within audible range, that is from 20 Hz to 20 kHz. Depending on the application we may distinguish microphones dedicated to sound acquisition (consumer devices and studio recording equipment) and microphones dedicated to sound measurements.

[1] MEMS stands for Micro-Electro-Mechanical System

Measurement microphones are characterized by higher performance and proportionally higher price.

Regardless of the transduction means, microphone consists of a diaphragm that is usually a membrane (fig. 1.1) anchored within a rigid housing. In order to ensure the equal static pressure level between the backvolume and surrounding, the housing is supplied with pressure equalization vent. On the occurrence of sound pressure the membrane deflection is transduced into alternative electrical signal by one of the following transduction mechanisms: electromagnetic induction, capacitance or resistance variation or piezoelectric effect.

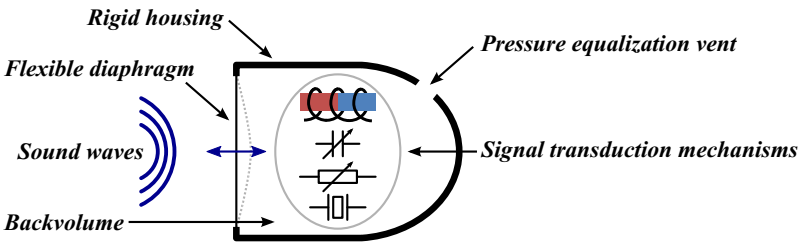

Figure 1.1: General structure of a microphone.

Means of sound pressure transduction

As we already presented, microphones use variety of mechanisms in signal transduction, microphones with conversion based on electromagnetic induction (dynamic microphones) are widely used on the stages, while measurement and MEMS microphones are mostly based on capacitive variation measurements. Moreover the MEMS technology enables integration of piezoelectric and piezoresistive materials, therefore the MEMS microphones with detection based on this materials are also reported.

Dynamic microphone consists of a flexible membrane which is connected with a coil (see fig. 1.2). On the occurrence of a sound pressure the membrane deflects and moves the coil relative to the fixed magnet. As a result, electric current proportional to the sound pressure variation flows through the coil. This kind of microphone does not need an external polarization, however the output signal has to be amplified by dedicated readout electronics.

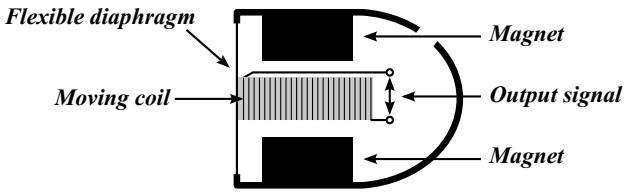

Figure 1.2: General structure of a dynamic microphone.

Another type is a **condenser microphone** that uses capacitance variations to detect a sound pressure (see fig. 1.3). In this kind of a microphone the membrane serves as an electrode which moves relative to the fixed electrode (called the backplate). With air as a dielectrical material between two electrodes one manage to measure the value of the capacitance that varies as a function of a distance between the membrane and the backplate. Initially the main drawback of capacitive detection was a need of external polarization, this problem has been solved by G. Sessler and J. West [5] by use of

permanently charged material (electret[2]) integrated into the membrane. Prepolarized condenser microphones are called the electret microphones (ECM).

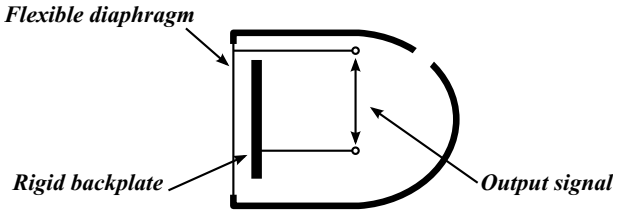

Figure 1.3: General structure of a condenser microphone.

Other popular microphones are those that use **piezoelectric and piezoresistive** effects. Regarding the fact that booth effects concerns materials that change their properties when subjected to stress (tensile or compressive), the construction of the microphone is presented on the common figure (fig. 1.4). Stress may be applied to the piezoelectric or the piezoresistive material directly by integration of the material into the membrane. The other mean to apply the stress is to transfer membrane deflection to stress-sensitive material by simple mechanisms. Since piezoelectric material generates electrical signal while stressed, microphones based on this material do not need external polarization, however the piezoresistor has to be externally polarized in order to read the resistance variations.

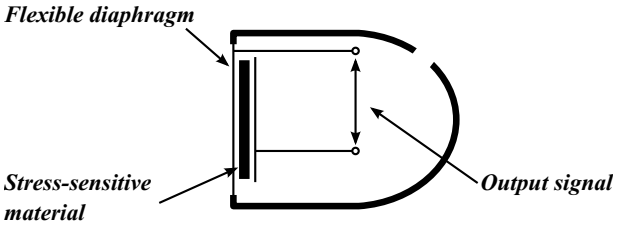

Figure 1.4: General structure of a microphone that uses the stress-sensitive materials.

Microphone specifications

We will now introduce several terms that are used in description of microphones properties. Brief introduction to the most important terminology used in microphones description can be found in papers of J. Lewis [8, 9], we recommend also the handbook prepared by Brüel & Kjær [10].

Sensitivity is a quantity that describes the output electrical signal of a microphone as a function of applied acoustic pressure. Datasheets provide the value of sensitivity at 1 kHz and sound pressure level of 94 dB (1 Pa). Sensitivity of a microphone with analog output signal is expressed in mV/Pa or in decibels referring to 1 V (dBV). Values in mV/Pa and dBV can be easily compared by use of the following formula:

$$Sensitivity_{dBV} = 20\log_{10}(Sensitivity/1[V/Pa]). \tag{1.1}$$

[2]Electret materials are fabricated by melting of dielectric material with charged particles and solidify it in electrostatic field.

Sensitivity of a microphone with digital output is expressed in dBFS (decibels referring to the full scale). To obtain value in dBFS we suppress reference pressure (94 dB) from the maximum acoustic load of a microphone.

Ideal response of a microphone is flat, however due to mechanical (solid and acoustical) properties the sensitivity may vary at the extremities of a frequency range. Variations of sensitivity with the frequency are represented by the frequency response curves normalized to 1 kHz (fig. 1.5).

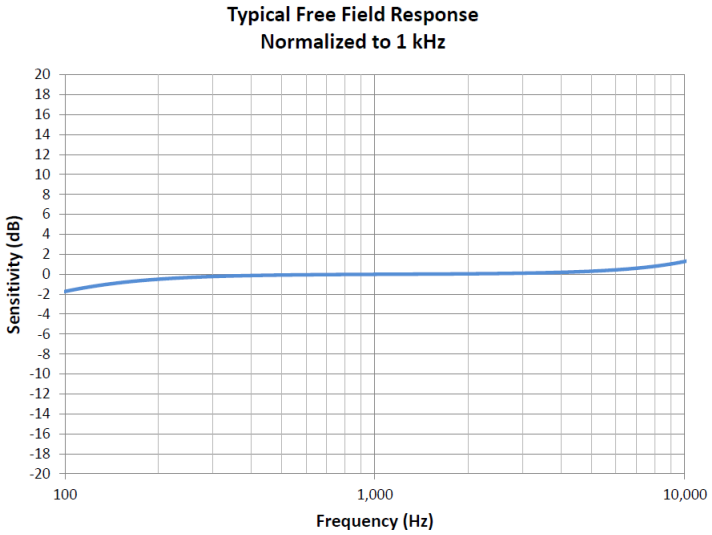

Figure 1.5: Frequency response curve of Knowles SPU0409LE5H MEMS microphone [11].

Bandwidth describes microphone capabilities to detect acoustic signal. Each microphone is characterized by its frequency range which is limited by low and high cutoff frequencies. We will show later that the low cutoff frequency is determined by the properties of acoustic vents and the housing of a microphone while the high cutoff frequency is set by a mechanical resonance of a diaphragm (membrane, beam etc.). Auditory region covers frequencies from 20 Hz up to 20 kHz, where the sound generated by speech is within 170 Hz - 4 kHz and music 50 Hz - 8.5 kHz (fig. 1.6); therefore depending on the application, microphones are designed in order to operate within full auditory region (bandwidth of 20 kHz) or a reduced bandwidth.

Signal to Noise Ratio (SNR) expressed in dBA (A-weighted[3] decibels) is a ratio between standard reference signal (94 dB at 1 kHz) and the equivalent input noise (noise floor) of a microphone. Equivalent input noise sets the lower detection limits of a microphone, it is measured in a quiet environment and it consists of sensing element noise and readout electronic noise.

Dynamic range expressed in dB is a domain of operation of the microphone within the noise floor and acoustic overload point. Acoustic overload point (also called MaxSPL or maximal acoustic load) is defined by the sound pressure level where the response of the microphone becomes nonlinear. Long-lasting exposition of microphone to the SPL

[3] A-weighting curve corresponds to the sensitivity of human ear that varies over the frequency range.

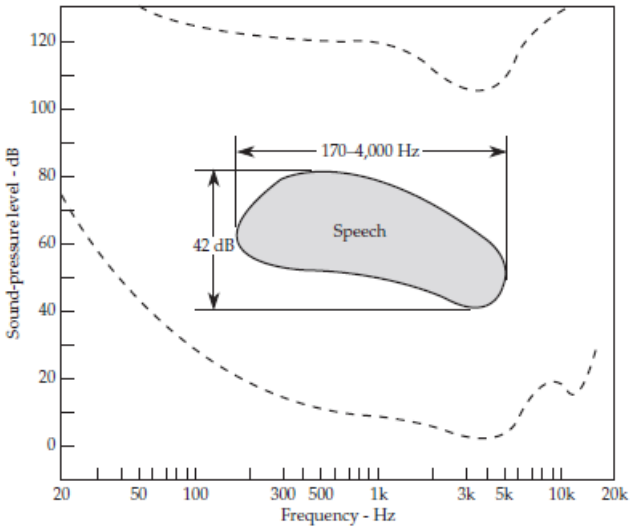

Figure 1.6: Auditory region according to F.A. Everest [12].

greater than maximal indicated value can lead to mechanical failure.
Acoustic overload point of a microphone is usually adjusted to be close to the threshold of pain which varies slightly over frequency range and is approximately 120 dB, however due to the growing demands of end users (concerts recording, aeroacoustic applications) this value tends to increase.

Directionality is a microphone property that describes the capability of detecting sound waves incidents from different directions relative to the sound port. It is represented on a polar grid plot called the "polar pattern", where the sensitivity is normalized to 0° incidence. Typically the sensitivity of a MEMS microphone does not depend on the sound source position (fig. 1.7), such response is called omnidirectional.

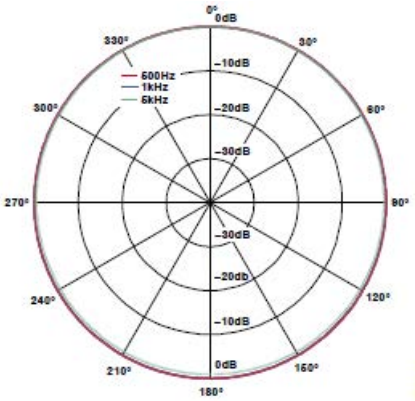

Figure 1.7: Polar pattern of omnidirectional microphone, on the example of Analog Devices MEMS microphone [9].

Total Harmonic Distortion (THD) is a ratio between total power of a signal and power of the fundamental frequency, it is expressed in percents:

$$THD = \frac{P_{total} - P_{fundamental}}{P_{fundamental}} \times 100. \tag{1.2}$$

THD is most commonly measured along with noise (THD+N). In this measurement microphone is excitated with sine wave signal. Power of harmonics is then measured by applying notch filter on the fundamental frequency (fig. 1.8). Comprehensive discussion on audio distortion measurements can be found in paper of S. Temme [13].

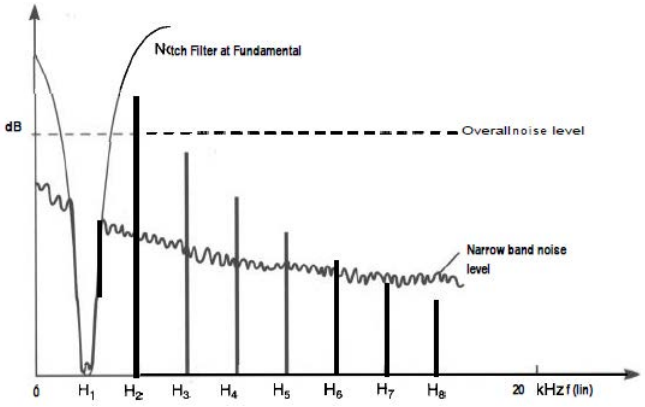

Figure 1.8: THD+N measurement with use of notch filter. From the paper of S. Temme [13].

1.2 International context of this work

Overview of a MEMS microphones

Commercial products

Micro-Electro-Mechanical Systems (MEMS) have their origins in well established semiconductors technology. It profits of electronic properties of Silicon and combines it with its exceptional mechanical characteristics in order to miniaturize wide range of transducers. It has been a long time since MEMS followed our daily life unnoticed - hidden in the ink-jet print heads, saving lives in such automotive applications as Airbags, tyre pressure monitoring systems (TPMS) and Electronics Stability Program (ESP) systems. Established MEMS devices enabled engineers to work on new designs and invent new, dedicated technological processes (example the Bosh process [14, 15]). Improvement in MEMS sensors technology enabled designers to aim consumer electronic market. After integration of accelerometers into consumer devices, the next natural step was to develop gyroscopes, magnetometers and microphones.

Despite the fact that the first working silicon microphone has been reported by G. Sessler and D. Hohm in 1983 [6] it has taken nearly 20 years when on 2002 Knowles has released SiSonic - the first commercial MEMS microphone. If we review the evolution of the international MEMS microphones market until 2013, we can define the following milestones:

- 2002 - Knowles releases the first commercial MEMS microphone,
- 2006 - Infineon enters the MEMS microphone market,

- 2006 - Akustica releases the first digital MEMS microphone which is additionally the first single chip microphone (MEMS and ASIC on the same die),
- 2007 - AAC Technologies begins mass production of MEMS microphones,
- 2009 - Bosch enters MEMS microphone market by acquiring Akustica,
- 2010 - Apple employs MEMS microphones in iPhone,
- 2011 - STMicroelectronics enters MEMS microphone market with focus on digital microphones,
- 2012 - Knowles claims to ship over 3 billions of chips since the release of its first SiSonic series,
- 2013 - InvenSense acquires MEMS microphone business line from Analog Devices.

Since the year 2002, U.S. - based Knowles has maintained the position of the leader in MEMS microphones market (fig. 1.9), however its domination has shrunk from 75% in 2011 to 50% in 2012 in favor of the other key players such as Chinese AAC Technologies, U.S. Analog devices, another Chinese company - GoerTek and French-Italian STMicroelectronics.

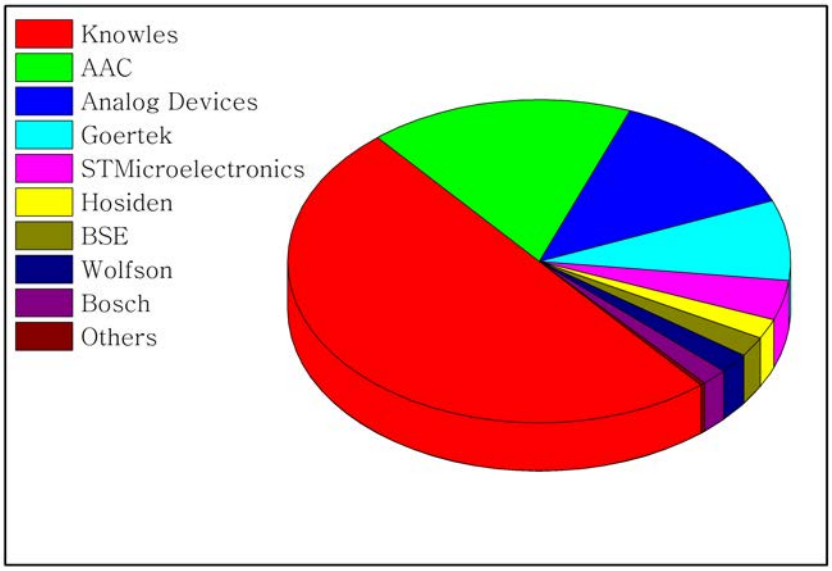

Figure 1.9: 2012 MEMS microphone market suppliers according to IHS iSuppli MEMS & Sensors Special Report.

Figure 1.10 shows MEMS microphone shipment forecast according to IHS iSuppli Research, February 2013. In addition data from the previous years starting from the year 2006 were included. On this figure we can observe the irregularity in shipment growth between the years 2010 and 2011 caused by the introduction of MEMS microphones into the iPhone 4 by Apple which has previously used exclusively ECMs and it now became the biggest buyer of MEMS microphones. Current version of Apple flag product - iPhone 5 uses 3 microphones, with two dedicated to speech acquisition and noise canceling while the third (placed at the back of the phone) is used for high definition video recording. Integration of MEMS microphones has set cellphones as the largest area of its employment (54% of microphones shipped in 2012 has been bought by two biggest

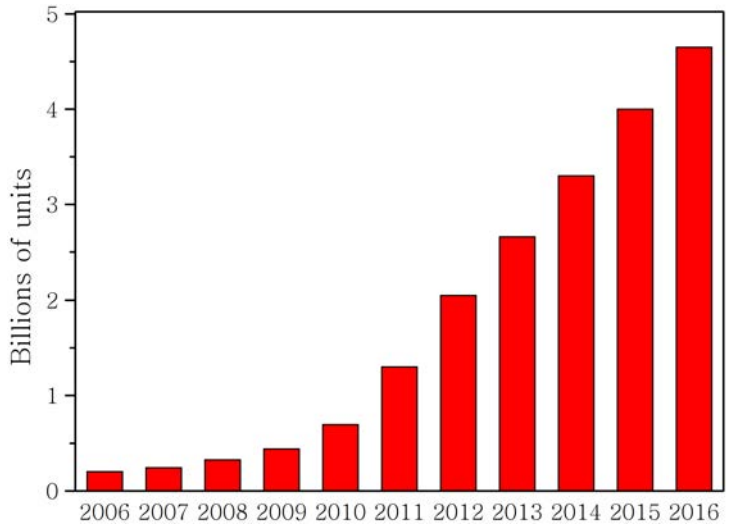

Figure 1.10: MEMS microphone shipment forecast according to IHS iSuppli Research, February 2013.

players that are Apple and Samsung). Cellphone application is followed by notebooks, headsets, media tablets and so on.

All of the commercially available MEMS microphones use capacitive means of detection. Such detection is realized by two electrodes micromachined in Silicon. One of the electrodes is rigid while the other deflects on the presence of sound pressure causing by that variation of capacitance. Packaged microphones have dimensions of single millimeters (fig. 1.11(a)), the package consist of a MEMS chip and dedicated readout electronics (ASIC) with analog or digital output (fig. 1.11(b)).

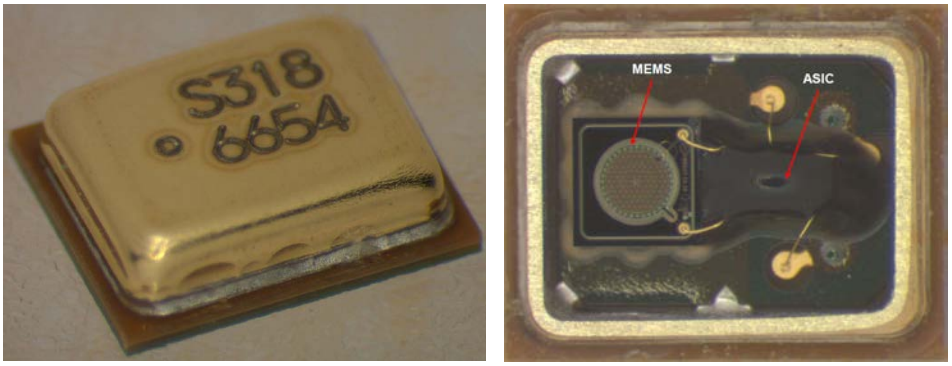

(a) Overall view (b) Top view

Figure 1.11: Knowles SPU0409LE5H microphone presented in reverse costing analysis by R. Fraux [16].

We have gathered the specifications of microphones of the key market players in table 1.1.

Table 1.1: Specifications of commercial MEMS microphones with the digital output.

Manufacturer	Specifications						
	Model	Sensitivity [dBFS/1Pa]	Bandwidth [kHz]	SNR [dBA]	MAX SPL [dB]	Current supply [μA]	Size [mm^3]
Knowles	SPK0833LM4HB	-26	0.1-10	63	122	500	4 x 3 x 1
AAC	SDM0401B-263-M02	-26	no data	60.5	no data	550	4 x 3 x 1
Analog Devices	ADMP521	-26	0.1-16	65	120	900	4 x 3 x 1
GoerTek	SD04OT263-01/02	-26	0.1-8	58	no data	600	4.7 x 3.8 x 1.3
STMicroelectronics	MP34DB01	-26	0.02-20	62.6	120	650	4 x 3 x 1

State of the art

Micromachined microphones are based on the rigid backplate and flexible membrane that deflects out of the wafer plane (fig. 1.12). Numerous surface micromachined membranes have been reported, among them those made of metalized silicon nitride [17–19], the combination of silicon nitride and polysilicon [20], polysilicon [19, 21–26] and bulk micromachined membrane reported by Y. Iguchi [27]. Regardless the design, membrane surface is in range of single square millimeters: from 0.38 mm^2 reported by A. Dehe [26] to 4.41 mm^2 reported by Y. Iguchi [27].

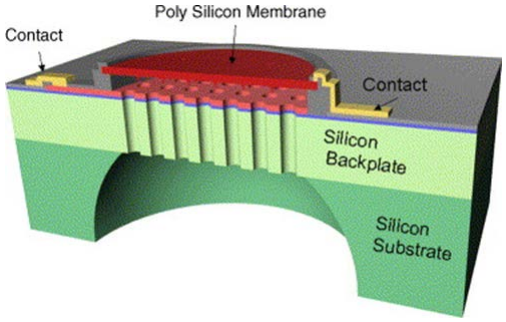

Figure 1.12: Example of state of the art condenser MEMS microphone [23].

Use of surface micromachining requires precautions in order to minimize the residual stress which preloads membrane and affects the response of a microphone. Residual stress in thin films can be caused by the mismatch of coefficient of thermal expansion, differences in technological process parameters (intrinsic stress), or in case of monocrystals - mismatch of crystal lattice. Some of the authors adjust the membrane stress by use of interlayers [20], the others by adding additional annealing steps [21], while J.W. Weigold [22] from Analog Devices, A. Dehe [23,26] from Infineon Technologies and C. Chan [25] have presented spring-suspended rigid membranes (fig. 1.13). A. Dehe has reported that employment of springs or corrugation rings increases the sensitivity from two to six times in comparison to standard clamped membrane.

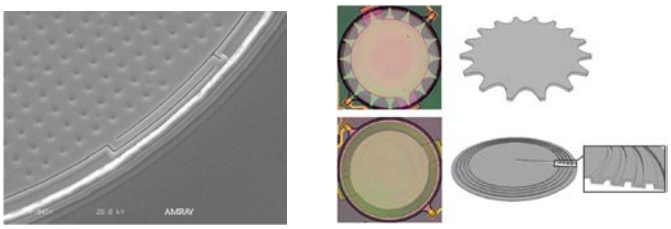

(a) By J.W. Weigold (b) By A. Dehe

Figure 1.13: Different types of spring-suspended membranes.

Measured performance and characteristics of state of the art microphones have been gathered in table 1.2. Pressure response of the reported microphones was characterized by comparison method in anechoic environment or by use of Kundt's tube. It is problematic to adequately compare these works since many crucial elements affecting microphone performance varies (membrane surface, bias voltage, acoustic port configuration - backvolume). However on figure 1.14 we have compared the SNR of some of the condenser microphones with regard to the surface of the membrane and the year of publication. SNR is proportional to the surface of the membrane, this tendency is

easily seen if we focus on the microphone reported by P. Rombach [20] where surface of the membrane equals 4 mm^2 and tree microphones reported by A. Dehe [26] where the surface of the membrane decreases from 0.95, 0.63 to 0.38 mm^2.

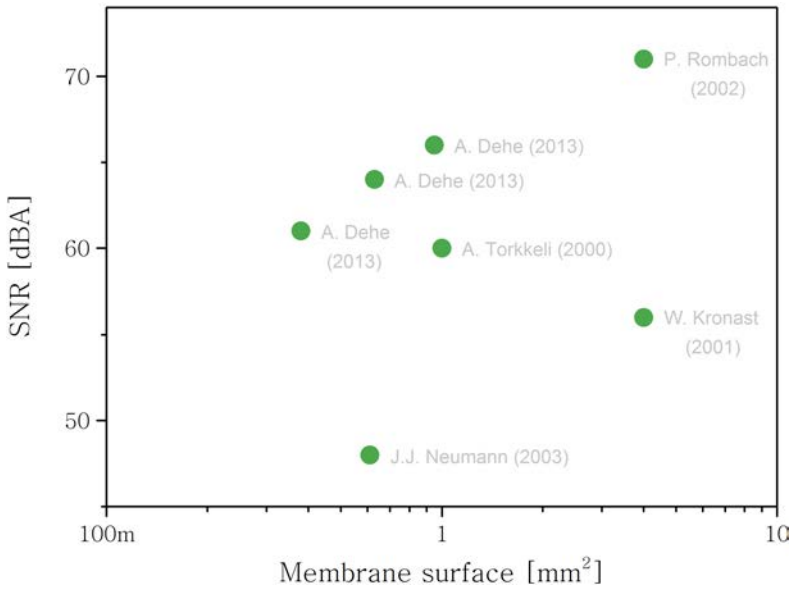

Figure 1.14: SNR with regard to the surface of the membrane and the year of publication.

It seems that the condenser MEMS microphones have reached their miniaturization limits. The limitations comes mainly from the fact that the sensitivity of the microphone decreases together with the miniaturization of the membrane. In this work we will propose the novel architecture of the microphone which improves the yield between the surface of the diaphragm and the resulting sensitivity. To investigate this new architecture the consortium of several partners has started the project MADNEMS which is described in the next subsection.

Table 1.2: Specifications of state of the art MEMS microphones

		Specifications					
Author		Year	Type	Sensitivity [dBV]	Bandwidth [kHz]	SNR [dBA]	Remarks
Y. B. Ning et al.	[17]	1996	Condenser	-43	0.10 - 20	no data	
A. Torkkeli et al.	[21]	2000	Condenser	-48	0.01 - 12	60	
M. Mullenborn et al.	[28]	2001	Condenser	-46	0.01 - 10	69	
W. Kronast et al.	[18]	2001	Condenser	-47	0.05 - 20	56	
P. Rombach	[20]	2002	Condenser	-38	0.02 - 20	71	
J.J. Neumann et al.	[29]	2003	Condenser	no data	0.02 - 10	48	
G.W. Elko et al.	[30]	2005	Condenser	no data	0.10 - 20	34 dB	unweighted SNR, directional
J.W. Weigold et al.	[22]	2006	Condenser	-47	no data	no data	
A. Dehe	[23]	2007	Condenser	-39	0.10 - 10	65	
Y. Iguchi et al.	[27]	2007	Condenser	-52	0.03 - 20	47	
T. Kasai et al.	[24]	2011	Condenser	-25 dBFS	0.02 - 20	63	digital output
C. Chiang et al.	[31]	2011	Condenser	-42	0.10 - 20	56	integrated ASIC
C. Chan et al.	[25]	2011	Condenser	-38	0.20 - 20	33	
A. Dehe et al.	[26]	2013	Condenser	-38	0.08 - 10	66	
M. Sheplak et al.	[32]	1999	Piezoresistive	-93	0.20 - 6	1	aeroacoustic application, MaxSPL 155 dB
M.L. Kuntzman et al.	[19]	2011	Optical	no data	0.04 - 10	66	
M.D. Williams	[33]	2012	Piezoelectric	-88	0.07 - 20	54	MaxSPL >172 dB

1.3 The "MADNEMS" project

My thesis was realized simultaneously to the industrial research project funded by the French National Research Agency and called the MADNEMS project (MADNEMS is abbreviation from the french phrase "Microphone A Détection par jauge NEMS" - microphone with detection realized with nanogauge). The target of the project was to develop novel MEMS microphone dedicated to the hearing aids and to the consumer electronic (especially portable devices). To prepare the prototype a consortium of several partners has been appointed:

CEA-Leti - "Laboratoire d'électronique des technologies de l'information" based in Grenoble. CEA-Leti has an extensive experience in field of MEMS, it has proposed the new concept of a MEMS microphone.

LVA - "Laboratoire Vibrations Acoustique". The laboratory of vibration and acoustics is based in Lyon and it is affiliated to the National Institute of Applied Science (INSA). It introduces the knowledge on acoustic phenomena and on characterization methods of the microphones.

IM2NP - "Institut Matériaux Microélectronique Nanosciences de Provence" based in Marseille is in charge of conception and fabrication of ASIC[4] with ultra-low power consumption.

Neurelec/Oticon Medical - Neurelec (acquired by Oticon Medical in 2013) is an industrial partner based in Sophia Antipolis technology park. An expert in field of cochlear implants that introduces its knowledge in signal processing and is in charge of final integration of the prototype into the BTE[5].

Motivation for the MADNEMS project comes from the innovative technological platform developped at CEA-Leti and called the M&NEMS. This platform based on piezoresistive detection realized with nanowires has already been proven to be relevant for fabrication of the accelerometers, gyroscopes, magnetometers and pressure sensor. High sensitivity of strain gauges in form of nanowires - called the nanogauges enabled the engineers from CEA-Leti to decrease the footprint of these sensors. Now we would like to prepare novel MEMS microphone based on the M&NEMS. Use of single technological platform for the microphone, pressure and inertial sensors may play a key role in the future integration of several sensors on one chip.

1.4 Organization of the manuscript

This thesis was prepared at CEA-Leti in collaboration with the LVA. It is the first thesis on MEMS microphone prepared at the Laboratory of Microsensors at CEA-Leti and its main target was to prepare the first prototype of the MEMS microphone to complete the M&NEMS sensors line. To initiate the research on acoustic sensors in the laboratory and to prove the new concept of the microphone there was a need to prepare the extended bibliographical research on several subjects. This bibliographical research covered the following issues:

- nomenclature used in microphone specifications,

[4] Application Specific Integrated Circuit
[5] BTE stands for Behind The Ear, it is a sound processor unit used in cochlear implant systems.

- evolution of the microphones and state of the art of the MEMS microphones,
- transduction mechanism suitable for the new architecture,
- proper tolls for simulation of the acoustic phenomena at the microscale,
- investigations on the chip-scale packaging of MEMS microphones,
- functional characterization methods.

This bibliographical research was done at the different development stages and it had a key role to competently assemble the subsystems of the microphone and prepare the first prototype that is in fabrication. The manuscript is divided into six chapters, to facilitate the reading, we present the organization of the chapters:

Chapter 1 is a general introduction to this work and it places it among the state of the art and the commercial market microphones.

Chapter 2 introduces the new concept of MEMS microphone patented by CEA-Leti and compares it to the state of the art MEMS microphones. Then we present the architecture and possible transduction mechanisms. Finally the technological platform used for sensor fabrication and the other sensors based on that technology are presented.

Chapter 3 discusses the approaches to model the acoustic phenomena in MEMS. We present models based on full set of linearized Navier-Stokes equations (state of the art and commercial solutions) and compare it with approximative Low Reduced Frequency model and Lumped Element model. This chapter is an introduction to the design considerations of proposed new MEMS microphone.

Chapter 4 consists of the microphone design considerations including the investigations of its acoustical, mechanical and electrical behavior. We designate the key factors that formulate the microphone characteristics. This considerations are completed by the discussion of the noise sources typical for MEMS microphones.

Chapter 5 gives the closer view on the process flow used in the designed microphone fabrication. Afterwards we review the chip-scale packaging used in commercial products and the in-house solution is proposed. At the end we discuss the advances in fabrication and the encountered difficulties.

Chapter 6 illustrates the work that has been done on the preparation for the functional characterization of the MEMS microphone in pressure-field and free-field conditions. While waiting for the prototype of designed microphone, the characterization methods have been validated with use of commercial MEMS microphone.

Chapter 2

New architecture of a MEMS microphone

The following chapter will present the concept of a Silicon MEMS microphone with a diaphragm that deflects in the plane parallel to a Silicon wafer (we call it the in-plane deflection). Amplitude of the diaphragm vibration is proportional to sound pressure fluctuations and can be detected by a capacitance or a resistance variation. Relevance of these detection means to the new architecture will be discussed and more suitable mechanism will be indicated. Finally the technological platform will be described and the existing sensors that are based on this technology (accelerometer, gyroscope, magnetometer and pressure sensor) will be reviewed.

2.1 Concept presentation

Presented concept is based on the invention by Ph. Robert and A. Walther of the MEMS Sensors Laboratory at CEA-Leti [34]. Microphone in this invention is described as a diaphragm enclosed between a bottom and a top wafer (fig. 2.1), where the one of the wafers is used as a base for MEMS fabrication and the second one is a lid. Acoustic vents that ensure sound pressure propagation and static pressure equalization are etched in both wafers.

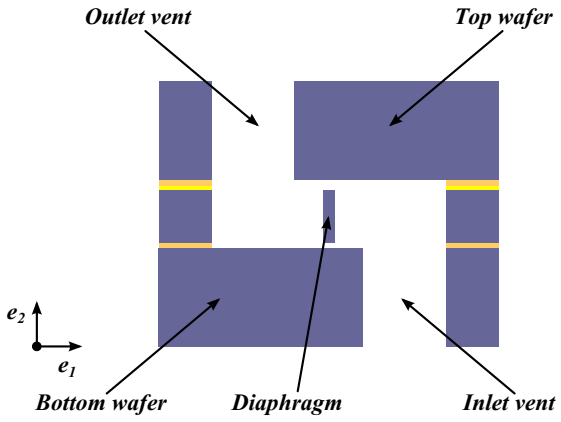

Figure 2.1: Cross-sectional view of the new MEMS microphone architecture (not to scale).

On the occurrence of sound, the pressure fluctuations propagates through the inlet

vent and reach the diaphragm which deflects proportionally to the pressure difference between inlet and outlet vents (fig. 2.2). Given concept can be modified by multiplication of the diaphragms and acoustic vents that leads to sophisticated system with higher performance.

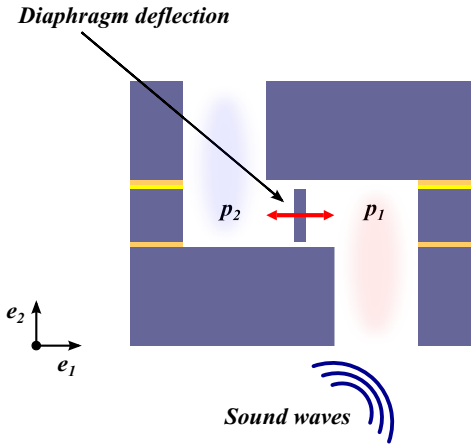

Figure 2.2: Diaphragm deflection mechanism (not to scale).

2.2 Possible transduction mechanisms

Regarding specific microphone concept and available technology of silicon micromachining two possible transduction mechanism have been identified: capacitive and piezoresistive transduction. Lets now review both of this mechanisms with emphasis on the electro-mechanical coupling and the sensitivity designation.

2.2.1 Capacitive transduction

For the considerations of electro-mechanical coupling in capacitive microphone we will use simplified model represented on figure 2.3. The model consists of the fixed electrode

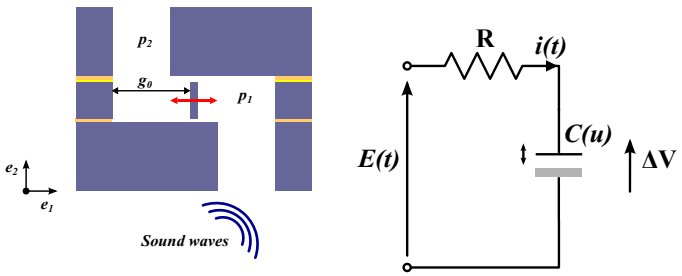

(a) Overall view (b) Electrical schematic

Figure 2.3: Capacitive transduction mechanism.

and the rigid diaphragm suspended on the springs with the stiffness k; g_0 is the initial distance between the electrodes. The diaphragm moves in-plane and it serves as an electrode with lateral surface S_d. The diaphragm displacement is denoted with u.

General governing equations

To begin the considerations we present the general governing equations, for the sake of simplicity we omit the damping:

$$m\ddot{u} + ku = F_a + F_{es}, \tag{2.1}$$

$$\frac{d}{dt}\left(C(u)\Delta V\right) = \frac{E(t) - \Delta V}{R}. \tag{2.2}$$

where m is a mass of the diaphragm and k is total stiffness of suspension springs. External forces in the system are F_a - acoustic force and F_{es} - electrostatic force:

$$F_{es} = \frac{1}{2}\frac{\partial C(u)}{\partial u}\Delta V^2 = -\frac{1}{2}\frac{\epsilon_0 S_d}{(g_0 + u)^2}\Delta V^2 \tag{2.3}$$

Governing electrical equation is expressed by the conservation of electric charge in the system. Capacitance of the sensor $C(u)$ depends on the actual position of the diaphragm according to:

$$C(u) = \frac{\epsilon_0 S_d}{g_0 + u}, \tag{2.4}$$

where ϵ_0 and S_d are permittivity of the vacuum and surface of the electrodes respectively and the displacement u is generated by the acoustic or electrostatic force.

Replacing F_{es} and $C(u)$ in equations 2.1 and 2.2 results in the following set of coupled nonlinear equations:

$$m\ddot{u} + ku = \frac{1}{2}\frac{\partial C(u)}{\partial u}\Delta V^2 + F_a, \tag{2.5}$$

$$C(u)\frac{d\Delta V}{dt} + \frac{\partial C}{\partial u}\frac{du}{dt}\Delta V = \frac{E(t) - \Delta V}{R}. \tag{2.6}$$

Static equilibrium and the pull-in voltage

We will now appoint the equilibrium points under static conditions ($E = const$, $\Delta V = E$). At the static equilibrium u is denoted U and it is a solution of:

$$kU + \frac{1}{2}\frac{\epsilon_0 S_d}{(g_0 + U)^2}E^2 = 0. \tag{2.7}$$

We may deduce that when the static polarization exceeds certain value, the electrostatic force may exceed the mechanical stiffness and the moving electrode will be pulled towards the fixed electrode. Static polarization for which the system becomes non stable and the electrodes get in contact is called the static **pull-in** voltage E_{pi}. The critical displacement of the electrode that corresponds to E_{pi} is denoted U_{pi}:

$$E_{pi} = \sqrt{\frac{k}{\epsilon_0 S_d}\left(\frac{2}{3}g_0\right)^3} \quad \text{and} \quad U_{pi} = -\frac{g_0}{3}. \tag{2.8}$$

The problem of the pull-in was thoroughly studied by V. Rochus [35], where this phenomenon has been introduced by use of a graph similar to the one presented on fig. 2.4: for the pull-in voltage only one solution is found (marked with doted line) whereas for $E < E_{pi}$ we found two solutions: stable and unstable one. Green area on fig. 2.4 represents the static polarization for which the system is stable - the sensor is operational.

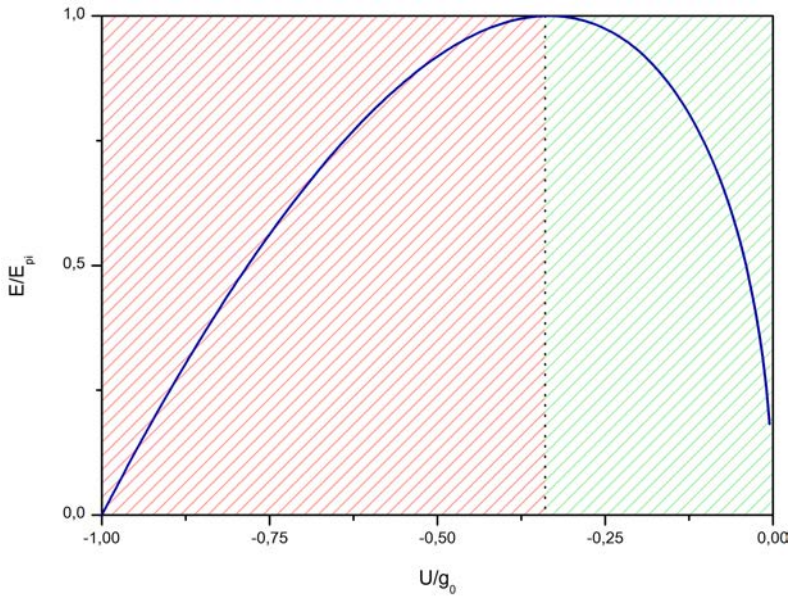

Figure 2.4: Illustration of the pull-in effect.

Electro-mechanical coupling governing equations

To study electro-mechanical coupling of the presented system, we will express the displacement u and voltage across the capacitor ΔV as a functions of time:

$$u(t) = U + \tilde{u}(t), \tag{2.9}$$

$$\Delta V(t) = E + \tilde{v}(t), \tag{2.10}$$

where U is the diaphragm displacement caused by the static voltage E; $\tilde{u}(t)$ and $\tilde{v}(t)$ are the small perturbations around U and E.

To study time-dependence of a system, the governing equations have to be linearized around the equilibrium points with use of Taylor series. Linearized governing mechanical equation become:

$$m\frac{d^2\tilde{u}}{dt^2} + k\tilde{u} = \tilde{F}_a + \frac{\epsilon_0 S_d}{(g_0+U)^3}E^2\tilde{u} - \frac{\epsilon_0 S_d}{(g_0+U)^2}E\tilde{v}, \tag{2.11}$$

We realize that the resulting stiffness k^* of a system consists of the mechanical stiffness and the electrostatic stiffness terms:

$$k^*\tilde{u} = \left(k - \frac{\epsilon_0 S_d}{(g_0+U)^3}E^2\right)\tilde{u}. \tag{2.12}$$

Linearization of the electrical equation governs the voltage fluctuations:

$$C(U)\dot{\tilde{v}} + \frac{\tilde{v}}{R} = \frac{C(U)}{(g_0+U)}E\dot{\tilde{u}}, \tag{2.13}$$

Sensitivity of capacitive sensor

Considering small harmonic pressure fluctuations $\tilde{p}$ and knowing the corresponding gap and voltage variations we can express the sensitivity of a capacitive microphone:

$$S(\omega) = \frac{\tilde{v}}{\tilde{p}} = \frac{S_d E}{k^*(g_0+U)} \cdot \left(\frac{\omega_0^2}{\omega_0^2 - \omega^2}\right) \cdot \left(\frac{RC(U)j\omega}{1 + RC(U)j\omega}\right), \tag{2.14}$$

where ω_0 denotes the resonance of the mechanical structure.

2.2.2 Piezoresistive transduction

Piezorestive effect involves the change of the conductor resistance as a function of applied stress. Piezoresistive effect exists in doped crystalline silicon and it is commonly used as a detection mechanism in MEMS sensors. One way of adoption of piezoresistive effect for sound pressure detection is integration of piezoresistor into silicon membranes. Such architecture has been already used in static pressure sensors (figure 2.5). Integra-

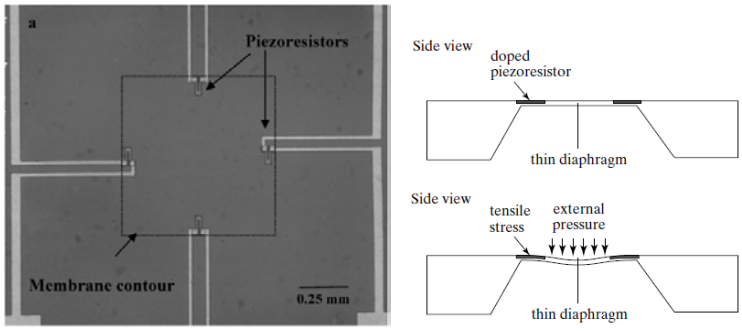

(a) MEMS piezoresistive pressure sensor [36].

(b) Stress generation inside the piezoresistors [37].

Figure 2.5: Example of MEMS piezoresistive pressure sensor.

tion of piezoresistors in this case can be achieved by selective deposition of doped silicon layer on the membrane in epitaxial process or by selective doping of silicon membrane in diffusion or ion implantation process [38]. Since the stress is distributed over the whole surface of the membrane, sensor optimization covers the stress maximization inside the piezoresistors. It can be achieved by placing piezoresistor in the maximal stress regions [39] and by keeping high ratio between the membrane and piezoresistors thickness [37]. Maximal stress in rectangular membrane occurs in the middle point of the membrane edge (tensile stress) and in the center of a membrane (compressive stress). Stress concentration regions can be additionally introduced by the special membrane features including boss [40] and trenches [41]. Integration of piezoresistors into the membrane creates p-n junction at the membrane-piezoresistors interfaces. This junction may lead to generation of leakage current. Leakage current values are negligible corresponding to piezoresistors bias current at room temperature, however it increases and may impact response of a sensor at elevated temperatures [42, 43].

Alternative design of piezoresistive sensor involves use of suspended Silicon nanowires (fig. 2.6) which serves as a piezoresistors. Piezoresistive effect in p-type nanowires fabricated on silicon-on-insulator (SOI) wafers has been studied by R. He and P. Yang [44]. They have reported that piezoresistive effect at nanoscale significantly rises compared with bulk Silicon and the nanowires seems to be a good direction towards more efficient MEMS sensors.

Electro-mechanical coupling governing equations

We may consider microphone architecture with piezoresistive nanogauge attached and stressed by diaphragm moving in-plane of SOI wafer (fig. 2.7). Mechanical governing

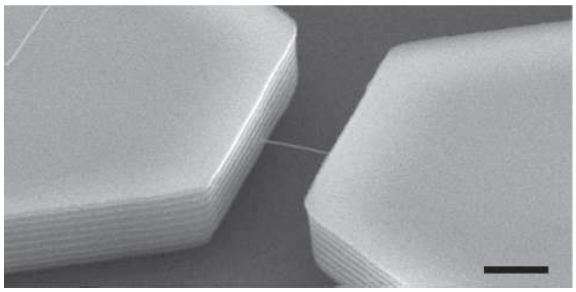

Figure 2.6: Silicon nanowire [44]. The scale bar is 2 μm.

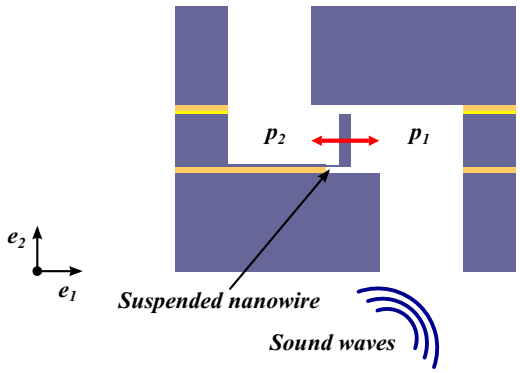

Figure 2.7: MEMS microphone with nanowire piezoresistor (not to scale).

equation for presented architecture will be as follow:

$$m\ddot{u} + (k + K_g)u = F_a, \tag{2.15}$$

where total stiffness will consist of diaphragm stiffness k and longitudinal stiffness of a nanogauge K_g.
Variation of nanogauge resistance ΔR depends proportionally on diaphragm displacement:

$$\Delta R = \pi_{pzr}\sigma_g R = \pi_{pzr}\frac{K_g u}{S_g}R, \tag{2.16}$$

where π_{pzr}, σ_g, R and S_g are piezoresistive coefficient, nanogauge longitudinal stress, nominal resistance of the nanogauge and surface of its longitudinal cross-section.

Wheatstone bridge architecture

Accurate measurements of ΔR can be carried out by use of electrical architecture called the Wheatstone bridge. It consists of two voltage dividers connected in parallel (fig. 2.8). If we feed both voltage dividers of Wheatstone bridge with current I_b and we assume that the values of resistance R are perfectly matched, then the output voltage ΔV will be null.
At the time when the resistors are not matched, the divided voltages are not equal which results in output voltage ΔV proportional to the resistance difference. Depending on the application, one to four piezoresistors can be introduced into Wheatstone bridge architecture (see fig. 2.9). Output signal for different bridge configurations is then

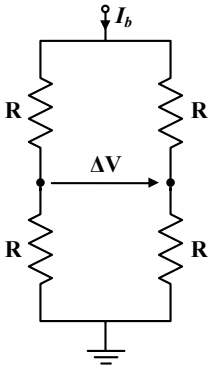

Figure 2.8: Resistors arranged into Wheatstone bridge architecture.

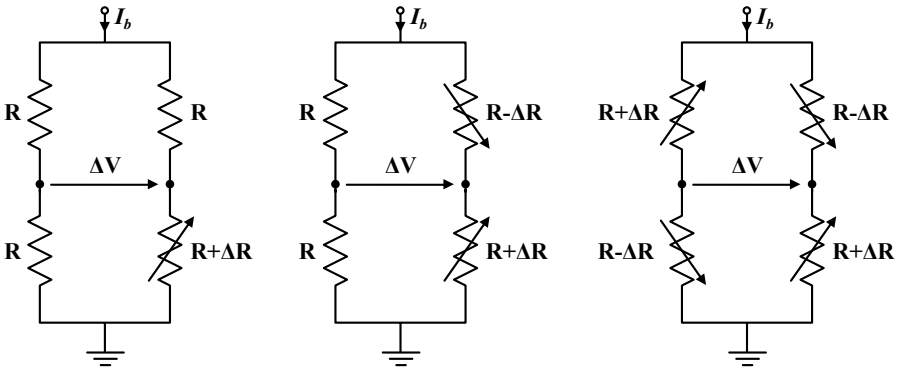

Figure 2.9: Possible Wheatstone bridge architectures for piezoresistive sensor [45].

related to the number of piezoresistors by the formulas 2.17-2.19.

$$\text{1 piezoresistor:} \quad \Delta V = \frac{I_b R}{4} \frac{\Delta R}{R + \frac{\Delta R}{4}} \approx \frac{I_b}{4} \Delta R, \tag{2.17}$$

$$\text{2 piezoresistors:} \quad \Delta V = \frac{I_b}{2} \Delta R, \tag{2.18}$$

$$\text{4 piezoresistors:} \quad \Delta V = I_b \Delta R. \tag{2.19}$$

Further considerations will be based on 4 piezoresistors configuration since it provides the highest output signal. If we now introduce ΔR into the equation 2.19, the governing equations of one-way coupled system will be given by:

$$\begin{bmatrix} F_a \\ \Delta V \end{bmatrix} = \begin{bmatrix} k + K_g \\ I_b \pi_{pzr} \frac{K_g}{S_g} R \end{bmatrix} u + \begin{bmatrix} m\ddot{u} \\ 0 \end{bmatrix} \tag{2.20}$$

Sensitivity of piezoresistive sensor

Sensitivity of piezoresistive sensor can be formulated analytically to capacitive sensor sensitivity. We start with expression of ΔV:

$$\Delta V = I_b \pi_{pzr} \frac{K_g}{S_g} R u, \tag{2.21}$$

by development of u we obtain:

$$S(\omega) = \frac{\Delta\tilde{V}}{\tilde{p}} = I_b \pi_{pzr} R \frac{S_d}{S_g} \frac{K_g}{k + K_g} \left(\frac{\omega_0^2}{\omega_0^2 - \omega^2} \right), \tag{2.22}$$

where ω_0 denotes the resonance of the mechanical structure.

2.2.3 Transduction mechanisms comparison

In the previous sections we have proposed two distinct planar microphone architectures: capacitive and piezoresistive based on suspended nanowires. Both architectures are comparable in terms of technological implementation - sensors can be fabricated basing on SOI wafers and standard microelectronic process; the main differences come from their mechanical and electric properties.

Comparison of mechanical properties

For the purpose of comparison we will imagine the diaphragm as a microbeam suspended at both extremities by the springs. Beam is considered to be rigid with stiffness k coming from the springs. Mechanical resonance frequency will be defined by the beam mass and by the total stiffness of a sensor which is stiffness k modified by introduction of negative electrostatic stiffness and longitudinal stiffness of a nanogauge for capacitive and piezoresistive detection relatively. While the longitudinal stiffness of nanogauge has a constant value defined by geometry, the electrostatic stiffness depends of static polarization of capacitor and may be used for active control of sensor resonant frequency. To set the static polarization of capacitive sensor one has to take precautions and do not exceed the pull-in voltage which will stuck the two electrodes. Since the capacitive system is two-way coupled, we may drive the displacement of a diaphragm with electrostatic force F_{es}. This possibility of actuation may be used for a self-test of a sensor which is not possible in case of piezoresistive MEMS that need integration of additional self-test electrode. Finally the capacitive sensor introduces considerably larger squeeze-film damping because of the electrodes (for example in case of comb-structures).

Sensitivity optimization

Analysis of sensitivity formulas - for capacitive (equation 2.14) and for piezoresistive (equation 2.22) sensor enable us to reveal the common rules that lead to sensitivity optimization. Therefore in both cases we need to increase the diaphragm surface and supply power. Moreover the sensitivity is amplified in the vicinity of the mechanical resonance. To profit of this mechanical amplification the value of the first mechanical resonance has to be set close to the sensor frequency range, however in such case the sensor sensitivity will vary across the bandwidth.
In case of capacitive sensor sensitivity optimization, we may simplify sensitivity formula on the assumption that electrostatic stiffness value is in general much lower than mechanical stiffness. Therefore we need to decrease the mechanical stiffness and the gap between the electrodes. Furthermore capacitive sensor output signal will be influenced over the frequency range by high-pass filter with corner frequency at $1/(2\pi RC(U))$.
If we now consider the sensitivity of piezoresistive sensor, we need to pay attention on proper design of piezoresistive nanogauge. In perfect case the stress in the nanogauge can be maximized by decrease of nanogauge section S_g and by optimization of the distribution of strain energy between the gauge and the diaphragm $K_g/(k + K_g)$.

Miscellaneous aspects and conclusion

Thanks to research on Silicon nanowires which can be fabricated on SOI wafers, piezoresistive sensors became more competitive to capacitive sensors. Unlike the classical piezoresistors integrated into silicon layer, suspended nanowires do not suffer of leakage current. Moreover further improvement of piezoresistive detection is possible since the longitudinal piezoresistive coefficient rises inversely proportional to nanowire section. Nanowire detection has an advantage on capacitive sensors in terms of high linearity of response and facility of sensor downscaling. Main features of both transduction mechanism has been summarized in table 2.1, adopted from work of D. Ettelt and Y. Deimerly [46, 47].

Table 2.1: Transduction mechanisms comparison.

	Transduction mechanism	
Feature	Condenser	Piezoresistive
Linearity	✗	✔
Downscaling	✗	✔
Technological complexity	✔	✔
Possibility of differential measurement	✔	✔
Possibility of actuation	✔	✗
Sensitivity to chip-package stress	high	low
Sensitivity to parasitic capacitance	high	low
Influence of squeeze-film damping	high	low
Temperature sensitivity	no	yes
Humidity dependent	yes	no
Sensitivity to electromagnetic interface	yes	no

2.3 The M&NEMS technology

Fundamentals of so-called M&NEMS technology have been initially presented in 2009 by Ph. Robert [48]. Name of the technology comes from combination of MEMS and NEMS structures as a components of final functional sensor. Ph. Robert has shown the application of M&NEMS concept to 3D accelerometer design. Figure 2.10 illustrates

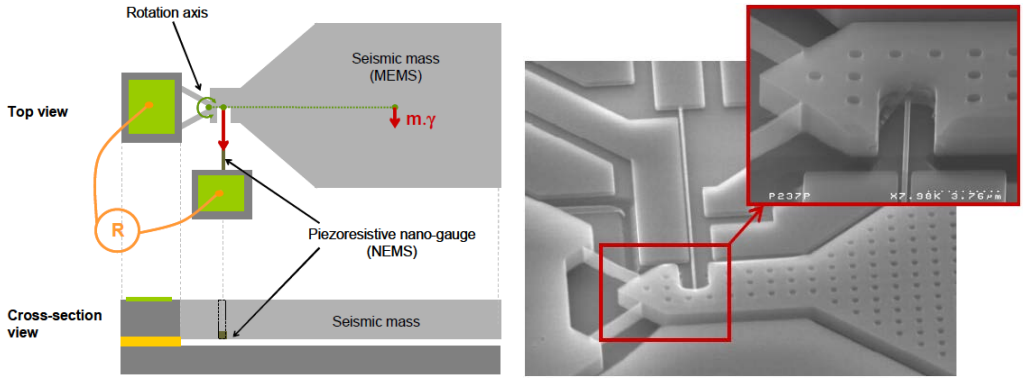

(a) Architecture of device. (b) Example of realization.

Figure 2.10: M&NEMS technology concept [48].

structure of in-plane accelerometer with inertial mass suspended on a hinge and a suspended nanogauge. Nanogauge is situated along the line between the rotation axis of the hinge and the center of inertia of the seismic mass. It is suspended between the seismic mass and the anchor in silicon substrate. On the occurrence of acceleration, the seismic mass will move rotationally with respect to the rotational axis, the inertial force will be exerted on the section of a nanogauge causing compressional or tensional longitudinal stress. Stress in the nanogauge generates resistance variation (piezoresistive effect) proportional to inertial force and amplified by factor coming from a lever effect (distance between rotation axis and center of seismic mass divided by distance between rotation axis and position of the nanogauge).

2.3.1 Technological platform

Technological platform developed at CEA-LETI, supports M&NEMS sensors fabrication on 200 mm SOI wafers. The simplified technological process (fig.2.11) begins with lithography and etching of NEMS nanowires (b), next the nanowires are protected by the oxide layer (c). Due to use of DUV lithography process, dimensions of nanogauges are limited to 250 nm. Afterward epitaxial layer of Silicon is grown (d) to be the base for DRIE of MEMS component (e). Electrical contacts are then realized by metalization of doped Silicon (e). The process is terminated with HF-vapor etching of oxide to release the MEMS structure and the nanogauges (f). Further steps may be realized for the specific designs such as magnetometers and pressure sensors. Additional steps required for M&NEMS microphone fabrication will be described later.

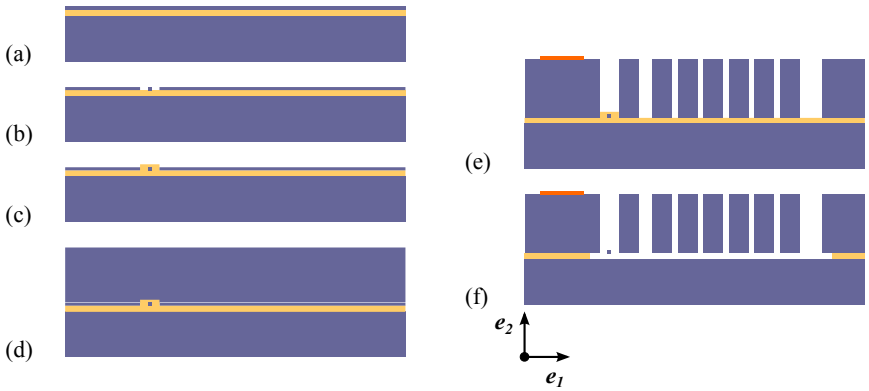

Figure 2.11: The M&NEMS technological platform.

2.3.2 M&NEMS sensors review

Since the first presentation, M&NEMS has shown the capabilities for multi-sensor integration on chip scale. Concept was proved by functional tests of 3D accelerometer. As a consequence of market demand on integrated IMU (Inertial Measurement Unit), research on magnetometer and gyroscope has been started simultaneously.
M&NEMS magnetometer [46, 49, 50] use three MEMS structures that assure magnetic field detection in 3 spacial directions (figure 2.12). In contrary to previous realizations of MEMS magnetometers based on Lorentz force (increased power consumption), it uses a permanent magnet. Permanent magnet was fabricate by sequential layer deposition of ferro- and anti-ferromagnetic materials on top of the MEMS rotating mass. Magnetic

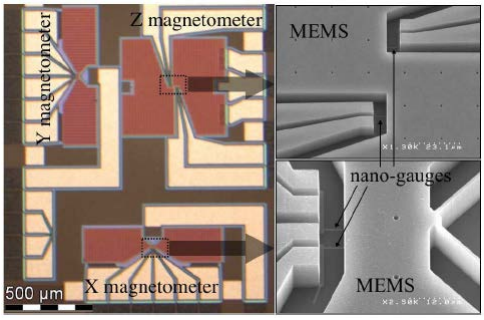

Figure 2.12: SEM image of 3D magnetometer with zoom on the nanogauges on the right side [50].

torque is then transduced into resistance variations in the way similar to acceleration sensor. It is worth to note that although both sensors are sensitive in 3 axes, the sensitivity of z-component is always noticeably lower than x- and y-component sensitivities. It is explained by higher stiffness of the hinge in case of z-direction, that in consequence reduces the stress in piezoresistive nanogauge.
MEMS gyroscope was presented on 2012 [51], it is based on dual mass structure vibrating at resonance (fig. 2.13). Actuation of structure is realized by use of comb-drive while

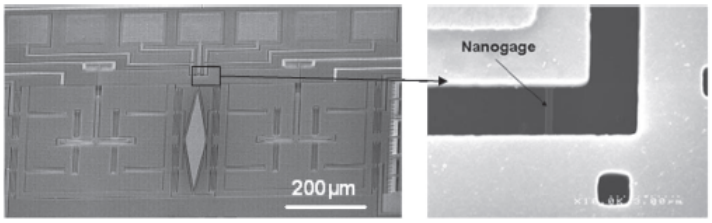

Figure 2.13: SEM image of gyroscope with zoom on nanogauge on the right side [52].

the signal coming from Coriolis force is detected by use of nanogauges. Actuation and detection may be done at the same (matched) or at different (unmatched) frequency depending on the sensitivity and noise contributions. Accelerometer works in ambient pressure, while the gyroscope as a vibrating structure requires vacuum environment. Problem of accelerometer and gyroscope chip scale integration has been investigated by Y. Deimerly [47]. Two potential solutions that have been selected and preliminary tested use resonating accelerometer or accelerometer with integrated electrostatic damping source.
Finally, the absolute pressure sensor concept has been demonstrated in 2013 [53]. Signal transduction in this sensor is based on deformations of thin Silicon membrane. These deformations are then transferred to the nanogauges by use of rotating, rigid lever arm (fig. 2.14).

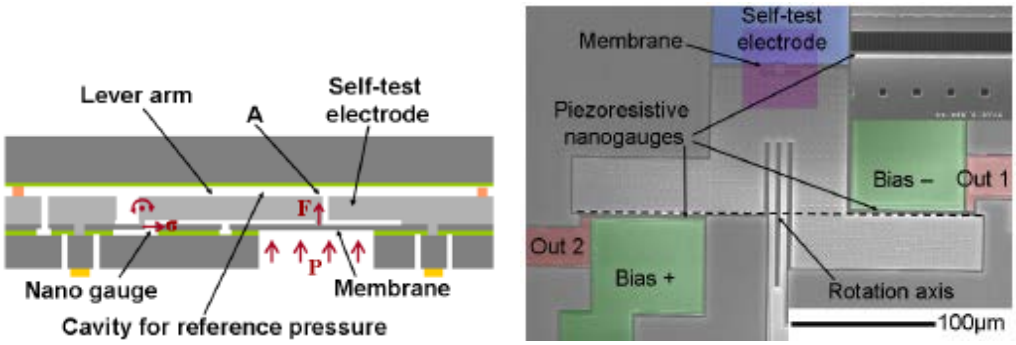

(a) Architecture of device. (b) SEM image.

Figure 2.14: M&NEMS pressure sensor [53].

Summary

Considering the fact that sensitivity of capacitive sensors decreases along with capacitance value, the further downscaling of those sensors that use relatively big comb structures became problematic. On the other hand presented M&NEMS technology seems to manage the downscaling issues while preserving the sensitivity. Fabrication and validation of individual M&NEMS sensors has been already pursued by first attempts towards multi-sensor chips. Under these circumstances use of M&NEMS technology in new architecture of MEMS microphone seems to be a natural step. So far we have briefly presented the new microphone architecture. This architecture will be investigated in chapter 4, however at the beginning we need to designate the proper tools to model the acoustic behavior of the system. This tools are discussed in the next chapter.

Chapter 3

Models for simulations of acoustic phenomena in MEMS

Comprehensive study of the new microphone architecture that was proposed in previous chapter requires proper tools to investigate the acoustic behavior. Classical acoustic approach is irrelevant in case of MEMS architecture where the scaling effects have to be considered. We start with presentation of full set of linearized Navier-Stokes equations and their implementation into the COMSOL Multiphysics finite element solver. We believe that this model approach is essential and it is the first step to understand the acoustic phenomena at the microscale. Afterward we compare the Full Linearized Navier-Stokes model (FLNS) with the approximative models: Low Reduced Frequency model (LRF) and Lumped Element model to designate the most efficient tool for MEMS microphone design.

3.1 Propagation of sound wave in dissipative fluid

As we will show later, in case of microsensor design the dissipative effects may severely impact the resultant performance. Depending on the dimensions of the acoustic duct, boundary and bulk regions may contribute to the medium properties equitably or - in the extreme cases, the boundary effects may completely prevail.
We start our discussion by introduction of the governing equations for the sound propagation in dissipative fluid.

Momentum equation

M. Bruneau [54] shows that conservation of the momentum in the dissipative fluid is governed by the linearized Navier-Stokes equations. The left side of general form represents the motion of a fluid where ρ_0 is quiscent fluid density and $\mathbf{v}$ is the particle velocity vector; while the right side consist of sum of $\bar{\bar{\sigma}}$ and $\bar{\mathbf{f}}$, which are the Cauchy stress tensor and the external body forces:

$$\rho_0 \frac{\partial \mathbf{v}}{\partial t} = \nabla \cdot \bar{\bar{\sigma}} + \bar{\mathbf{f}}. \tag{3.1}$$

We assume that the fluid is homogeneous and isotropic (this conditions were presented by M. Bruneau) and the Cauchy stress tensor comprise the acoustic pressure fluctuations and the shear stress generated by the viscous effects:

$$\bar{\bar{\sigma}} = -p\mathbf{I} + \bar{\bar{\sigma}}_v, \tag{3.2}$$

where p denotes the acoustic pressure and $\bar{\bar{\sigma}}_v$ is a viscous shear stress. To understand the viscous shear we need to imagine the elementary volume of the fluid (fig. 3.1). If we divide the fluid domain into thin layers, where each layer have a different velocity starting from zero and limited by the bulk velocity, then the portion of a fluid situated between two different layers undergoes the shear force in the manner showed on figure 3.1. Viscous

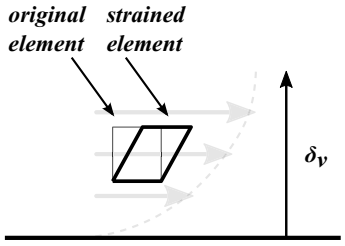

Figure 3.1: Elementary fluid element undergoing the viscous shear force.

stress is comprehensively discussed in book of M. Bruneau [54], where the final formula for $\bar{\bar{\sigma}}_v$ is given by:

$$\bar{\bar{\sigma}}_v = \mu\left(\overline{\overline{\nabla \mathbf{v}}} + \left(\overline{\overline{\nabla \mathbf{v}}}\right)^{\mathrm{T}}\right) - \left(\frac{2}{3}\mu - \eta\right)(\nabla \cdot \mathbf{v})\,\mathbf{I}, \tag{3.3}$$

where μ is the shear viscosity (dynamic viscosity) and η is the coefficient of the bulk viscosity ($\eta \approx 0.60\mu$ after A.D. Pierce [55] and R. Kampinga [56]).
In the further considerations the momentum equation for dissipative problem is presented in the following manner:

$$\boxed{\rho_0 \frac{\partial \mathbf{v}}{\partial t} = -\nabla p + \nabla \cdot \bar{\bar{\sigma}}_v + \bar{\mathbf{f}}.} \tag{3.4}$$

State equation

In the dissipative process we need to investigate the heat introduced to the system by the viscous heat flux. At this point we may also introduce the eventual external heat source that may perturb the sound propagation. Therefore the entropy of the system varies and the state equation reads:

$$\boxed{\rho_0 c_P \frac{\partial \tau}{\partial t} - \frac{\partial p}{\partial t} = -\nabla \cdot \mathbf{q} + \bar{\mathrm{Q}},} \tag{3.5}$$

where c_P and τ are the heat capacity ratio at constant pressure and the temperature fluctuations respectively, $\bar{\mathrm{Q}}$ denotes the external heat source inside the system and $\mathbf{q}$ denotes the heat flux density defined by the Fourier heat law:

$$\mathbf{q} = -\kappa \nabla \tau, \tag{3.6}$$

where κ is the thermal conductivity.

Continuity equation

We present the conservation of mass in the system knowing that the motion of fluid induces the density fluctuations (ρ):

$$\frac{\partial \rho}{\partial t} = -\rho_0 \nabla \cdot \mathbf{v}, \tag{3.7}$$

To present this term with use of pressure and temperature variations R. Kampinga [56] used the identity coming from the equation of state of the perfect gas:

$$\frac{\rho}{\rho_0} = \frac{p}{P_0} - \frac{\tau}{T_0}, \tag{3.8}$$

where P_0 and T_0 are the quiescent pressure and quiescent temperature respectively. By introducing equation 3.8 into equation 3.7 we relate the divergence of the velocity field with the pressure and temperature variations:

$$\boxed{-\frac{1}{T_0}\frac{\partial \tau}{\partial t} + \frac{1}{P_0}\frac{\partial p}{\partial t} = -\nabla \cdot \mathbf{v}.} \tag{3.9}$$

Final set of general equations

We present the propagation of sound in dissipative fluid with momentum 3.10, state 3.11 and continuity 3.12 equations:

$$\rho_0 \frac{\partial \mathbf{v}}{\partial t} = -\nabla p + \nabla \cdot \bar{\bar{\sigma}}_v + \bar{\mathbf{f}}, \tag{3.10}$$

$$\rho_0 c_P \frac{\partial \tau}{\partial t} - \frac{\partial p}{\partial t} = -\nabla \cdot \mathbf{q} + \bar{\mathrm{Q}}, \tag{3.11}$$

$$-\frac{1}{T_0}\frac{\partial \tau}{\partial t} + \frac{1}{P_0}\frac{\partial p}{\partial t} = -\nabla \cdot \mathbf{v}. \tag{3.12}$$

3.2 Scaling effects in acoustics

Relevance of viscous boundary layer

In classical acoustic problems, where the fluid is assumed to be non-dissipative, the particle velocity is proportional to the gradient of pressure. If we consider the sound wave propagation in large cavity we can indeed rely on that relation and assume that the velocity profile (that is parallel to the rigid boundary) is constant across the waveguide and the velocity field corresponds to the one in perfect fluid (fig. 3.2(a)).
However the real velocity profile at the microscale (fig. 3.2(b)) differs from the perfect one in the vicinity of the rigid boundary. Moreover the velocity of a fluid on the boundary is null (no-slip conditions) and it increases with the distance from the boundary and obtain the bulk velocity at the distance δ_v (thickness of the viscous boundary layer).

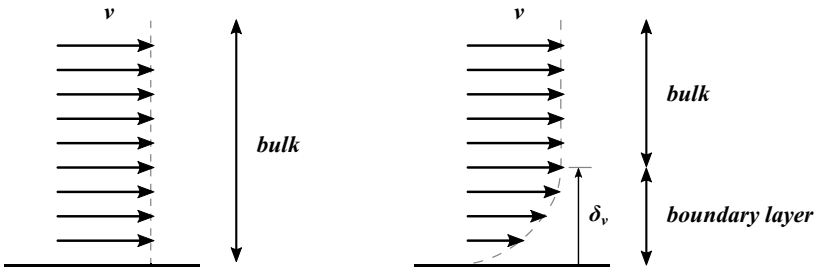

(a) Perfect fluid. (b) Real conditions.

Figure 3.2: Velocity field in the vicinity of rigid boundary, based on work of A. Lallemand [57].

Relevance of thermal boundary layer

The origins of thermal dissipation effects in sound propagation are related to uneven temperature of fluid and adjacent material. Therefore fluid-solid interface suffers from temperature gradient that generates thermal conduction. This gradient is appointed by difference between the temperature on the boundary (imposed by solid material) and the temperature of the bulk.
Similar to the viscous boundary layer, the thickness of thermal boundary layer (δ_t) is determined by the distance between the fluid-solid interface and the point where the fluid temperature is comparable to the one of the bulk material

Thicknesses of the boundary layers

The exact formulas for viscous (eq. 3.13) and thermal (eq. 3.14) boundaries thicknesses presented by N. Joly [58] are as follows:

$$\delta_v = \sqrt{\frac{2\mu}{\rho_0 \omega}} \tag{3.13}$$

$$\delta_t = \sqrt{\frac{2\kappa}{\rho_0 c_P \omega}} \tag{3.14}$$

Both viscous and thermal boundary layers thicknesses are inversely proportional to the square root of the frequency, where ω is an angular frequency ($\omega = 2\pi f$).
Dependence of the boundary layers on the frequency is presented on figure 3.3. Dashed rectangle indicates the region of the exploitation of thermoviscous effects in this thesis. Frequency range is limited by the audible bandwidth (20 Hz - 20 kHz), while the thickness axis limit the rectangle by the characteristic dimensions of MEMS devices (from single micrometers to single millimeters).
Within the audible range the thicknesses of boundary layers are as follows:

- 0.5 mm - 15 µm for the viscous effects,
- 0.6 mm - 18 µm for the thermal effects.

Although the listed dimensions are in the same order of magnitude and the thermal layer is slightly thicker, the viscous effects are believed to be of higher significance. Comparison between this effects is summarized by Prandtl number presented in work of M. Bruneau [54] and R. Kampinga [56]:

$$Pr_N = \frac{\delta_v^2}{\delta_t^2} = \frac{\mu c_P}{\kappa}. \tag{3.15}$$

For air at ambient pressure and room temperature the Prandtl number is about 0.75.

Knowing the thickness of viscous boundary layer for 20 Hz and 20 kHz, its evolution with the frequency may be additionally illustrated with use of simple geometry as on fig. 3.4. The dimensions of the geometry are 50×200 µm^2. We impose gradient of pressure 1 Pa between the shorter sides and no-slip conditions on the longer sides. When the sound propagates at frequency of 20 Hz, δ_v is much thicker than the characteristic dimension of the guide (0.5 mm $\gg$ 50 µm). The boundary layer is not distinguishable from the bulk zone and the velocity profile is parabolic. For the propagation frequency of 20 kHz δ_v becomes 15 µm and we can distinguish two boundary zones close to the walls and the bulk zone which appears in the center of the guide and where the velocity over the section is constant.

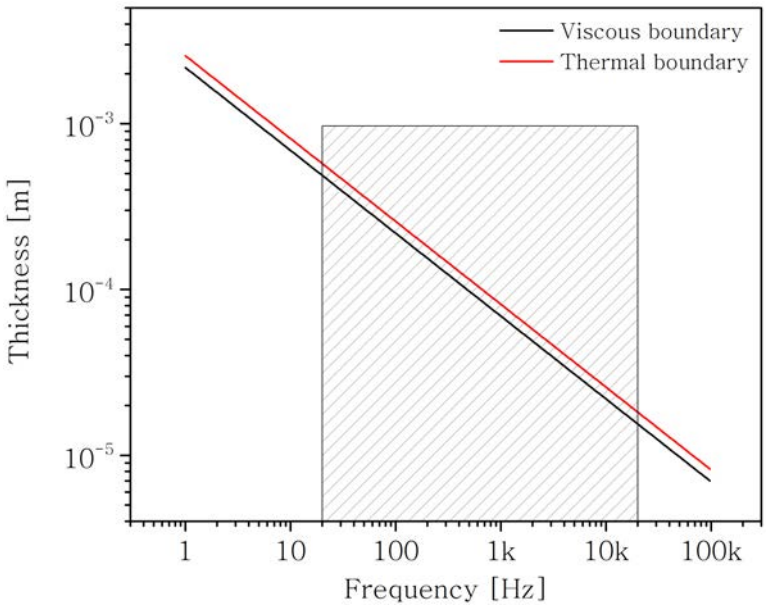

Figure 3.3: Viscous and Thermal boundary layers thicknesses as a function of frequency.

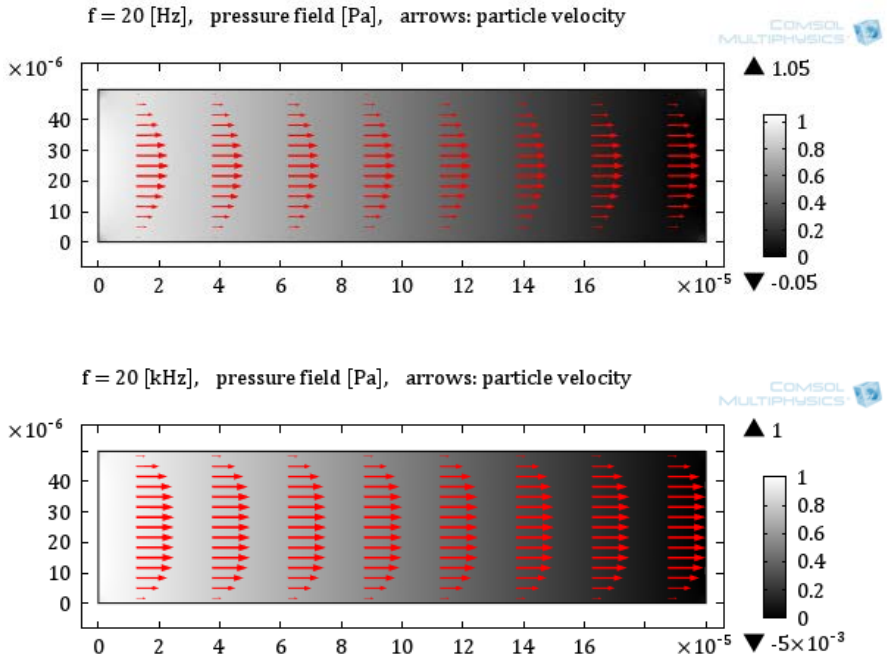

Figure 3.4: Evolution of viscous boundary layer thickness in audible range.

3.3 Full Linearized Navier-Stokes model (FLNS)

The most straightforward way of modeling the sound propagation in dissipative fluid is to implement the full set of linearized Navier-Stokes equations into FEA solver. It is making this model the most complete one: with velocity, pressure and temperature fluctuations as degrees of freedom. Such modeling approach has been chosen by R. Kampinga [56,59] that has presented comprehensive studies on FLNS model. The following procedure is then mainly based on work of R. Kampinga and some aspects of the FEA theory is based on book of O.C. Zienkiewicz [60]. Moreover it is a following of work on MEMS microphone model presented already by Laboratoire Vibrations et Acoustique (LVA-INSA de Lyon) [61,62].

Assumptions

We assume that the fluid is Newtonian[1] and use the ideal gas assumption.
Linearization assumes that the pressure and temperature variations are small relatively to quiescent values and the velocity variations are small relative to the speed of sound in the medium:

$$|p/p_0| \ll 1, \qquad |\tau/T_0| \ll 1, \qquad |\mathbf{v}/c_0| \ll 1. \tag{3.16}$$

3.3.1 Boundary conditions

The boundary conditions used in viscothermal models by N. Joly [58] and R. Kampinga [59] are of Dirichlet or Neumann type. Dirichlet type is used when we want to impose the fixed value of the variable on the boundary, while the Neumann type impose the fixed value for the gradient of variable in normal direction. Depending on the circumstances, the boundary conditions for the temperature are:

$$\tau = 0 \quad \Leftrightarrow \quad \text{isothermal wall,} \tag{3.17}$$

$$\tau = \bar{\tau} \quad \Leftrightarrow \quad \text{prescribed temperature fluctuations,} \tag{3.18}$$

$$\partial\tau/\partial n = \mathbf{q}\cdot(-\mathbf{n}) = 0 \quad \Leftrightarrow \quad \text{adiabatic wall,} \tag{3.19}$$

$$\mathbf{q}\cdot(-\mathbf{n}) = \bar{h} \quad \Leftrightarrow \quad \text{heat flux,} \tag{3.20}$$

where $\bar{h}$ denotes the external heat rate. The mechanical boundary conditions are as follows:

$$\mathbf{v} = 0 \quad \Leftrightarrow \quad \text{no-slip conditions,} \tag{3.21}$$

$$\mathbf{v} = \bar{\mathbf{v}} \quad \Leftrightarrow \quad \text{prescribed velocity with no-slip conditions,} \tag{3.22}$$

$$\bar{\bar{\sigma}}\cdot\mathbf{n} = 0 \quad \Leftrightarrow \quad \text{no normal stress,} \tag{3.23}$$

$$\bar{\bar{\sigma}}\cdot\mathbf{n} = \bar{\mathbf{t}} \quad \Leftrightarrow \quad \text{prescribed normal stress,} \tag{3.24}$$

where $\bar{\mathbf{t}}$ denotes the surface force density coming from external forces.

[1] Under assumptions of Newtonian fluid the viscous stress at every point is proportional to the rate of strain.

3.3.2 Problem formulation

It is very difficult to resolve the FLNS model analytically, however it is possible to implement the full set of governing equations into the FEA solver to obtain the estimated solution. To do so we use the procedure presented in book of O.C. Zienkiewicz [60]. In this procedure the problem is implemented into FEA in form of the weak equations. Weak formulation approach enables one to avoid the second-order and higher-order derivatives, to say colloquially - it weakens the general equations.

Domain

We know that the exact solution of the problem in the domain is obtained for:

$$0 = \bar{\mathbf{f}} - \rho_0 \frac{\partial \mathbf{v}}{\partial t} - \nabla p + \nabla \cdot \bar{\bar{\sigma}}_v, \tag{3.25}$$

$$0 = \bar{\mathrm{Q}} - \rho_0 c_P \frac{\partial \tau}{\partial t} + \frac{\partial p}{\partial t} - \nabla \cdot \mathbf{q}, \tag{3.26}$$

$$0 = \frac{1}{T_0}\frac{\partial \tau}{\partial t} - \frac{1}{P_0}\frac{\partial p}{\partial t} - \nabla \cdot \mathbf{v}. \tag{3.27}$$

This equations are then weakened by integration over the domain $\mathcal{D}$ and can be presented in the following manner:

$$\begin{aligned} &\int_{\mathcal{D}} \mathbf{v}^* \cdot \left\{ -\rho_0 \frac{\partial \mathbf{v}}{\partial t} - \nabla p + \nabla \cdot \bar{\bar{\sigma}}_v + \bar{\mathbf{f}} \right\} \mathrm{d}V \\ &+ \int_{\mathcal{D}} \frac{\tau^*}{T_0} \cdot \left\{ -\rho_0 c_P \frac{\partial \tau}{\partial t} + \frac{\partial p}{\partial t} - \nabla \cdot \mathbf{q} + \bar{\mathrm{Q}} \right\} \mathrm{d}V \\ &+ \int_{\mathcal{D}} p^* \cdot \left\{ \frac{1}{T_0}\frac{\partial \tau}{\partial t} - \frac{1}{P_0}\frac{\partial p}{\partial t} - \nabla \cdot \mathbf{v} \right\} \mathrm{d}V \;=\; 0, \end{aligned} \tag{3.28}$$

where each term is multiplied by $\mathbf{v}^*$, τ^* and p^* that are the test functions.

Boundaries

Dirichlet boundary conditions constraint the value of the variable on the boundary. Procedure of setting this condition as an addition to Neumann boundary conditions is well explained in Comsol Multiphysics Reference Manual [63]. Dirichlet boundary terms for the problem solution are as follows:

$$0 = \bar{\mathbf{v}} - \mathbf{c}_m \mathbf{v}, \tag{3.29}$$

$$0 = \bar{\tau} - \mathbf{c}_\tau \tau, \tag{3.30}$$

where $\mathbf{c}_m$ denotes the row vector that designates the spatial direction of applied velocity and $\mathbf{c}_\tau$ is a scalar (1×1 row vector) representing value 1 on the boundaries where the temperature fluctuations are imposed. This particular boundary conditions impose the constraints but in practice the imposed values vary and to maintain the allowed error we need to establish the reaction forces. Comsol Multiphysics use for this purpose variables defined only at the boundaries and called the Lagrangian multipliers. Lagrangian multipliers for our problem are: λ_m and λ_τ for mechanical and thermal boundary conditions

respectively. Lagrangian multipliers, which store the reaction forces are then introduced into the Neumann boundary conditions that become:

$$0 = \overline{\mathbf{t}} - \bar{\bar{\sigma}} \cdot \mathbf{n} - \mathbf{c}_m^{\mathrm{T}} \lambda_m, \tag{3.31}$$

$$0 = \bar{h} - \mathbf{q} \cdot (-\mathbf{n}) - \mathbf{c}_\tau^{\mathrm{T}} \lambda_\tau \tag{3.32}$$

We may now present the weak form of the terms that have to be respected on the boundary $\partial\mathcal{D}$, starting with Neumann conditions for the velocity and the temperature fluctuations (first two lines) and completing with Dirichlet conditions (third line):

$$\begin{aligned} &\int_{\partial\mathcal{D}} \mathbf{v}^* \cdot \left\{ \overline{\mathbf{t}} - \bar{\bar{\sigma}} \cdot \mathbf{n} - \mathbf{c}_m^{\mathrm{T}} \lambda_m \right\} \mathrm{d}S \\ &+ \int_{\partial\mathcal{D}} \frac{\tau^*}{T_0} \cdot \left\{ \bar{h} - \mathbf{q} \cdot (-\mathbf{n}) - \mathbf{c}_\tau^{\mathrm{T}} \lambda_\tau \right\} \mathrm{d}S \\ &+ \int_{\partial\mathcal{D}} \lambda_m^* \cdot \{ \bar{\mathbf{v}} - \mathbf{c}_m \mathbf{v} \} + \frac{\lambda_\tau^*}{T_0} \cdot \{ \bar{\tau} - \mathbf{c}_\tau \tau \} \mathrm{d}S \;=\; 0. \end{aligned} \tag{3.33}$$

Complete problem

We can arrange the weak form so the consecutive lines corresponds to the momentum, state and continuity terms, then the last line corresponds to the Dirichlet boundary conditions:

$$\begin{aligned} &\int_{\mathcal{D}} \mathbf{v}^* \cdot \left\{ -\rho_0 \frac{\partial \mathbf{v}}{\partial t} - \nabla p + \nabla \cdot \bar{\bar{\sigma}}_v + \overline{\mathbf{f}} \right\} \mathrm{d}V + \int_{\partial\mathcal{D}} \mathbf{v}^* \cdot \left\{ \overline{\mathbf{t}} - \bar{\bar{\sigma}} \cdot \mathbf{n} - \mathbf{c}_m^{\mathrm{T}} \lambda_m \right\} \mathrm{d}S \\ &+ \int_{\mathcal{D}} \frac{\tau^*}{T_0} \cdot \left\{ -\rho_0 c_P \frac{\partial \tau}{\partial t} + \frac{\partial p}{\partial t} - \nabla \cdot \mathbf{q} + \bar{\mathrm{Q}} \right\} \mathrm{d}V + \int_{\partial\mathcal{D}} \frac{\tau^*}{T_0} \cdot \left\{ \bar{h} - \mathbf{q} \cdot (-\mathbf{n}) - \mathbf{c}_\tau^{\mathrm{T}} \lambda_\tau \right\} \mathrm{d}S \\ &+ \int_{\mathcal{D}} p^* \cdot \left\{ \frac{1}{T_0} \frac{\partial \tau}{\partial t} - \frac{1}{P_0} \frac{\partial p}{\partial t} - \nabla \cdot \mathbf{v} \right\} \mathrm{d}V \\ &+ \int_{\partial\mathcal{D}} \lambda_m^* \cdot \{ \bar{\mathbf{v}} - \mathbf{c}_m \mathbf{v} \} + \frac{\lambda_\tau^*}{T_0} \cdot \{ \bar{\tau} - \mathbf{c}_\tau \tau \} \mathrm{d}S \;=\; 0. \end{aligned} \tag{3.34}$$

Foregoing equation contains the second order derivatives which can be reduced with use of Green's theorem as in work of R. Kampinga [56]. As a result we obtain:

$$\begin{aligned} &\int_{\mathcal{D}} \mathbf{v}^* \cdot \left(-\rho_0 \frac{\partial \mathbf{v}}{\partial t} \right) + (\nabla \cdot \mathbf{v}^*)\, p + \overline{\overline{\nabla \mathbf{v}^*}} \colon \bar{\bar{\sigma}}_v \, \mathrm{d}V + \int_{\mathcal{D}} \mathbf{v}^* \cdot \overline{\mathbf{f}} \, \mathrm{d}V + \int_{\partial\mathcal{D}} \mathbf{v}^* \cdot \left\{ \overline{\mathbf{t}} - \mathbf{c}_m^{\mathrm{T}} \lambda_m \right\} \mathrm{d}S \\ &+ \int_{\mathcal{D}} \frac{\tau^*}{T_0} \cdot \left(-\rho_0 c_P \frac{\partial \tau}{\partial t} + \frac{\partial p}{\partial t} \right) + \frac{\nabla \tau^* \cdot \mathbf{q}}{T_0} \, \mathrm{d}V + \int_{\mathcal{D}} \frac{\tau^*}{T_0} \cdot \bar{\mathrm{Q}} \, \mathrm{d}V + \int_{\partial\mathcal{D}} \frac{\tau^*}{T_0} \cdot \left\{ \bar{h} - \mathbf{c}_\tau^{\mathrm{T}} \lambda_\tau \right\} \mathrm{d}S \\ &+ \int_{\mathcal{D}} p^* \cdot \left(\frac{1}{T_0} \frac{\partial \tau}{\partial t} - \frac{1}{P_0} \frac{\partial p}{\partial t} \right) - p^* \cdot (\nabla \cdot \mathbf{v}) \, \mathrm{d}V \\ &+ \int_{\partial\mathcal{D}} \lambda_m^* \cdot \{ \bar{\mathbf{v}} - \mathbf{c}_m \mathbf{v} \} + \frac{\lambda_\tau^*}{T_0} \cdot \{ \bar{\tau} - \mathbf{c}_\tau \tau \} \mathrm{d}S \;=\; 0. \end{aligned} \tag{3.35}$$

3.3.3 Solving method

Weighted residuals

Exact solution of the model is presented in eq. 3.34 or 3.35, however to find this solution FEA starts with replacement of variables with its approximations. Problem solved with approximate variables gives intermediate solution that suffers of inaccuracies. In weighted residual approximation method described by O.C. Zienkiewicz [60] this inaccuracies are represented with the functions called the residuals. Residuals in our document are denoted $\mathcal{R}$ and $\mathcal{A}$, which are the functions of the same variables as the general equations defined in the domains:

$$\begin{aligned}
\mathcal{R}_{\mathbf{v}}^{(\mathcal{D})}(\tilde{\mathbf{v}},\tilde{\tau},\tilde{p}) &= -\rho_0\frac{\partial\tilde{\mathbf{v}}}{\partial t} - \nabla\tilde{p} + \nabla\cdot\bar{\bar{\sigma}}_v + \overline{\mathbf{f}},\\
\mathcal{R}_{\tau}^{(\mathcal{D})}(\tilde{\mathbf{v}},\tilde{\tau},\tilde{p}) &= -\rho_0 c_P\frac{\partial\tilde{\tau}}{\partial t} + \frac{\partial\tilde{p}}{\partial t} - \nabla\cdot\mathbf{q} + \bar{\mathrm{Q}},\\
\mathcal{R}_{p}^{(\mathcal{D})}(\tilde{\mathbf{v}},\tilde{\tau},\tilde{p}) &= \frac{1}{T_0}\frac{\partial\tilde{\tau}}{\partial t} - \frac{1}{P_0}\frac{\partial\tilde{p}}{\partial t} - \nabla\cdot\tilde{\mathbf{v}},
\end{aligned} \tag{3.36}$$

where $\tilde{\mathbf{v}}$, $\tilde{\tau}$ and $\tilde{p}$ are the arbitrary variables. Residuals for the boundaries yields:

$$\begin{aligned}
\mathcal{R}_{\mathbf{v}}^{(\partial\mathcal{D})}(\tilde{\mathbf{v}}) &= \overline{\mathbf{t}} - \bar{\bar{\sigma}}\cdot\mathbf{n} - \mathbf{c}_m^{\mathrm{T}}\tilde{\lambda}_m,\\
\mathcal{R}_{\tau}^{(\partial\mathcal{D})}(\tilde{\tau}) &= \bar{h} - \mathbf{q}\cdot(-\mathbf{n}) - \mathbf{c}_{\tau}^{\mathrm{T}}\tilde{\lambda}_{\tau},
\end{aligned} \tag{3.37}$$

$$\begin{aligned}
\mathcal{A}_{\mathbf{v}}^{(\partial\mathcal{D})}(\tilde{\mathbf{v}}) &= \bar{\mathbf{v}} - \mathbf{c}_m\tilde{\mathbf{v}},\\
\mathcal{A}_{\tau}^{(\partial\mathcal{D})}(\tilde{\tau}) &= \bar{\tau} - \mathbf{c}_{\tau}\tilde{\tau},
\end{aligned} \tag{3.38}$$

where $\tilde{\lambda}_m$ and $\tilde{\lambda}_\tau$ are the arbitrary Lagrangian multipliers. Until the solver reaches the most precise solution, subsequent arbitrary variables and Lagrangian multipliers are used. Therefore until the exact solution is found the system response is non-null and corresponds to the solution inaccuracy:

$$\begin{aligned}
\tilde{\mathcal{L}}(\tilde{\mathbf{v}^*},\tilde{\tau^*},\tilde{p^*},\tilde{\lambda_m^*},\tilde{\lambda_\tau^*},\tilde{\mathbf{v}},\tilde{\tau},\tilde{p},\tilde{\lambda_m},\tilde{\lambda_\tau}) = \ldots\\
&\int_{\mathcal{D}}\tilde{\mathbf{v}^*}\cdot\mathcal{R}_{\mathbf{v}}^{(\mathcal{D})}(\tilde{\mathbf{v}},\tilde{\tau},\tilde{p})\,\mathrm{d}V + \int_{\partial\mathcal{D}}\tilde{\mathbf{v}^*}\cdot\mathcal{R}_{\mathbf{v}}^{(\partial\mathcal{D})}(\tilde{\mathbf{v}})\,\mathrm{d}S\\
&+\int_{\mathcal{D}}\frac{\tilde{\tau^*}}{T_0}\cdot\mathcal{R}_{\tau}^{(\mathcal{D})}(\tilde{\mathbf{v}},\tilde{\tau},\tilde{p})\,\mathrm{d}V + \int_{\partial\mathcal{D}}\frac{\tilde{\tau^*}}{T_0}\cdot\mathcal{R}_{\tau}^{(\partial\mathcal{D})}(\tilde{\tau})\,\mathrm{d}S\\
&+\int_{\mathcal{D}}\tilde{p^*}\cdot\mathcal{R}_{p}^{(\mathcal{D})}(\tilde{\mathbf{v}},\tilde{\tau},\tilde{p})\,\mathrm{d}V\\
&+\int_{\partial\mathcal{D}}\tilde{\lambda_m^*}\cdot\mathcal{A}_{\mathbf{v}}^{(\partial\mathcal{D})}(\tilde{\mathbf{v}}) + \frac{\tilde{\lambda_\tau^*}}{T_0}\cdot\mathcal{A}_{\tau}^{(\partial\mathcal{D})}(\tilde{\tau})\,\mathrm{d}S,
\end{aligned} \tag{3.39}$$

where $\tilde{\mathbf{v}^*},\tilde{\tau^*},\tilde{p^*},\tilde{\lambda_m^*},\tilde{\lambda_\tau^*}$ are the arbitrary test functions.

Discretization and convergence

R. Kampinga has studied the influence of the shape functions (used in the discretization) on the stability of the solver and on the convergence. Combinations of the shape

functions for different degrees of freedom has shown that choosing the same shape functions for the velocity and the pressure result in problems with stability. The stability problems occurs mostly at low frequencies when the problem becomes incompressible. The combinations of shape functions presented by Kampinga are gathered in table 3.1, where:

- P_1 - piecewise linear,
- P_2 - quadratic,
- Q_1 - bilinear,
- Q_2 - biquadratic,
- P_1^+ - shape function space enriched by cubic bubble functions,
- P_{-1} - piecewise linear functions discontinuous over the element boundaries,
- P_2^+ - shape function space enriched by cubic bubble functions.

Table 3.1: Combinations of shape functions investigated by R. Kampinga [59].

Stokes element	shape	v, v^*	p, p^*	τ, τ^*
Taylor hood	$\triangle$	P_2	P_1	P_2
Taylor hood	$\square$	Q_2	Q_1	Q_2
Crouzeix Raviart	$\triangle$	P_2^+	P_{-1}	P_2
MINI	$\triangle$	P_1^+	P_1	P_1

R. Kampinga correlated the performance of each shape function for simple 2D geometry with different mesh sequences (triangular and quadrilateral with different refinement). He indicated the Taylor Hood and Crouzeix Raviart to be the best choices for FLNS. Moreover both velocity and temperature elements are the most efficient if we use quadratic functions.

3.3.4 Means of FLNS model enhancement

Another approach for modeling acoustic effects in dissipative fluid has been presented by N. Joly [64]. This model is dedicated for numerical studies and the full set of linearized Navier-Stokes equations is modified in order to present full acoustic problem only with use of velocity and temperature fluctuations. It means that the model employs only two out of initial four degrees of freedom and as a consequence it reduces the computation cost. Equations have been derived under assumptions of Stokesian fluid[2] which is homogenous and it is at rest. Additionally the linear behavior for the differential form of fluid state equation has been assumed.

Starting with the momentum, continuity and state equations N. Joly introduces the complementary parameters, where first two are the viscous characteristic lengths and the third one is the thermal characteristic length:

$$l_v = (\eta + 4/3\mu)/\rho_0 c_0, \tag{3.40}$$

$$l'_v = \mu/\rho_0 c_0, \tag{3.41}$$

$$l_h = \kappa/(\rho_0 c_0 c_P). \tag{3.42}$$

[2]Assumption of Stokesian fluid means that the viscous stress is proportional to the rate of strain and the heat flux is proportional to the temperature gradient.

Additionally fluctuations of the volumetric mass density and the entropy are:

$$\rho = \frac{\gamma}{c_0^2}\left(p - \frac{P_0}{T_0}\tau\right), \tag{3.43}$$

$$s = \frac{c_P}{T_0}\left(\tau - \frac{T_0}{P_0}\frac{\gamma - 1}{\gamma}p\right), \tag{3.44}$$

where γ denotes the specific heat ratio. Combination of the foregoing parameters and the expressions of density and entropy with general set of equations gives:

$$-\frac{\partial^2 v}{\partial t^2} + \left(\frac{c_0^2}{\gamma} + c_0 l_v \frac{\partial}{\partial t}\right)\nabla(\nabla \cdot v) - c_0 l_v' \frac{\partial}{\partial t}\nabla \times (\nabla \times v) - \frac{P_0}{\rho_0 T_0}\frac{\partial}{\partial t}\nabla\tau = 0, \tag{3.45}$$

$$\frac{\partial \tau}{\partial t} - \gamma l_h c_0 \nabla \cdot (\nabla\tau) + \frac{T_0}{P_0}\frac{\gamma - 1}{\gamma}\rho_0 c_0^2 \nabla \cdot v = 0. \tag{3.46}$$

The foregoing set of equations appoint the temperature and velocity perturbations however it may be completed by the expression of acoustic pressure perturbations and density perturbations related to the temperature and velocity by the following identities:

$$\frac{\partial p}{\partial t} = \frac{P_0}{T_0}\frac{\partial \tau}{\partial t} - \frac{\rho_0 c_0^2}{\gamma}\nabla \cdot v, \tag{3.47}$$

$$\frac{\partial \rho}{\partial t} = -\rho_0 \nabla \cdot v. \tag{3.48}$$

Model of N. Joly has been successfully applied for simulations of several acoustic elements [58, 65]. However, regarding the problematic of this thesis the best boundary condition for acoustic simulations is to prescribe the pressure (prescribed stress boundary condition) at the microphone inlet. This kind of boundary condition is not evident in case of the model presented by N. Joly which provides boundary conditions for temperature and velocity [58].

3.4 Low Reduced Frequency model (LRF)

In 1975 H. Tijdeman presented so-called Low Reduced Frequency model which solves the propagation of sound in viscothermal fluid enclosed by rigid cylindrical tube [66]. Later the problem was studied by W.M. Beltman [67], while R. Kampinga [56] applied LRF to solve the problem for geometry that consists of two parallel plates.

Assumptions

LRF is a simplified viscothermal model for small tubes and slits. In this model the pressure is assumed to be constant across the section and varies along the sound wave propagation direction (axial direction). On the opposite hand, the velocity and the temperature variations are considered only across the section of the duct. All three authors make the similar assumptions for the problem which can be summarized:

- homogenious medium,
- no mean flow,
- laminar flow,

- small amplitude, sinusoidal perturbations,
- cross-section much smaller than the acoustic wavelength,
- cross-section is uniform or slowly varies,
- geometry length must be large to neglect the end effects,
- no internal heat generation.

Lets rewrite the general set of equations. We consider that direction x corresponds to the propagation direction, then the v_1 corresponds to the particle velocity fluctuations in propagation direction, while the v_2 and v_3 components are considered null. We omit the divergence of the velocity, which becomes $\nabla \cdot \mathbf{v} = \partial v_1/\partial x$. Then the momentum equation is limited to the propagation direction and it gives:

$$\rho_0 j\omega v_1 - \mu \left(\frac{\partial^2 v_1}{\partial y^2} + \frac{\partial^2 v_1}{\partial z^2} \right) = -\frac{\partial p}{\partial x}. \tag{3.49}$$

We then neglige the temperature fluctuations in axial direction to obtain the modified state equation:

$$\rho_0 c_P \frac{\partial \tau}{\partial t} - \kappa \left(\frac{\partial^2 \tau}{\partial y^2} + \frac{\partial^2 \tau}{\partial z^2} \right) = \frac{\partial p}{\partial t}. \tag{3.50}$$

Finally the continuity equation is not modified:

$$-\frac{1}{T_0}\frac{\partial \tau}{\partial t} + \frac{1}{P_0}\frac{\partial p}{\partial t} = -\frac{\partial v_1}{\partial x}. \tag{3.51}$$

3.4.1 Problem formulation

Velocity and temperature fields

Further procedure is based on the approach of R. Kampinga [56] where the approximate viscothermal solutions enable one to express the velocity and temperature fluctuations with use of so-called shape functions for velocity field Ψ_v and temperature field Ψ_τ:

$$v(x, y, z, \omega) = \Psi_v(y, z, \omega) \left[-\frac{1}{\rho_0 j\omega} \frac{\partial p}{\partial x}(x, \omega) \right], \tag{3.52}$$

$$\tau(x, y, z, \omega) = \Psi_\tau(y, z, \omega) \left[\frac{p}{\rho_0 c_P}(x, \omega) \right]. \tag{3.53}$$

On first sight we may have impression that the expressions in brackets (eq. 3.52 and 3.53) are not complete and that we describe the isentropic problem, however the dissipative effects are included in the shape functions as shown below. The shape functions are the solutions of the following differential equations:

$$\Psi_v + k_v^{-2} \left[\frac{\partial^2 \Psi_v}{\partial y^2} + \frac{\partial^2 \Psi_v}{\partial z^2} \right] = 1, \tag{3.54}$$

$$\Psi_\tau + k_\tau^{-2} \left[\frac{\partial^2 \Psi_\tau}{\partial y^2} + \frac{\partial^2 \Psi_\tau}{\partial z^2} \right] = 1, \tag{3.55}$$

where k_v and k_τ are the viscothermal wave numbers defined by R. Kampinga as: $k_v^2 = -j\omega\rho_0/\mu$ and $k_\tau^2 = -j\omega\rho_0 c_P/\kappa$. This definitions correspond in fact to the thicknesses of boundary layers (see section 3.2):

$$k_v = \frac{1-j}{\delta_v(\omega)} \qquad \text{and} \qquad k_\tau = \frac{1-j}{\delta_\tau(\omega)}. \tag{3.56}$$

Analytical solutions of shape functions for several cross-sections are presented by R. Kampinga [56]. Moreover the solution of shape function for any cross-section may be computed with use of FEA. Figures 3.5 and 3.6 show the solution of velocity shape function for circular cross-section. The results obtained with COMSOL reveal the evolution of shape function with the frequency.

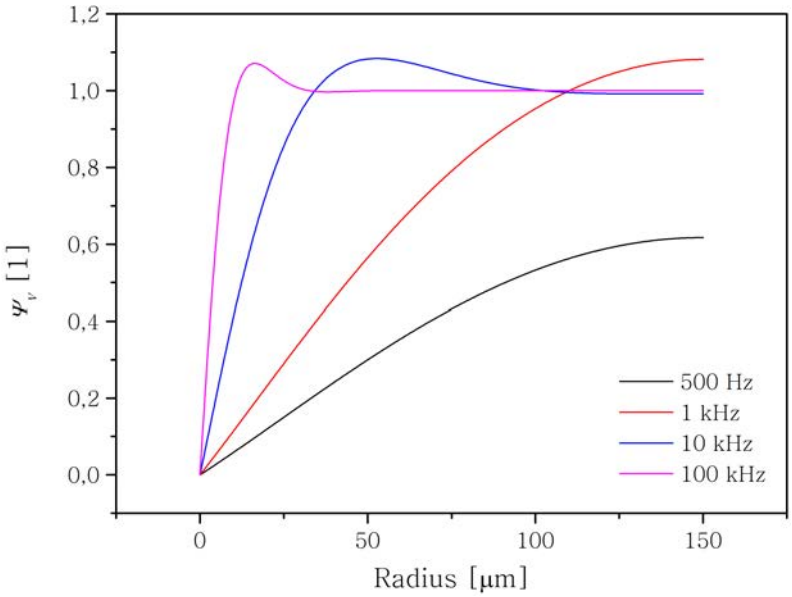

Figure 3.5: Evolution of the velocity shape function for circular vent with radius of 150 μm.

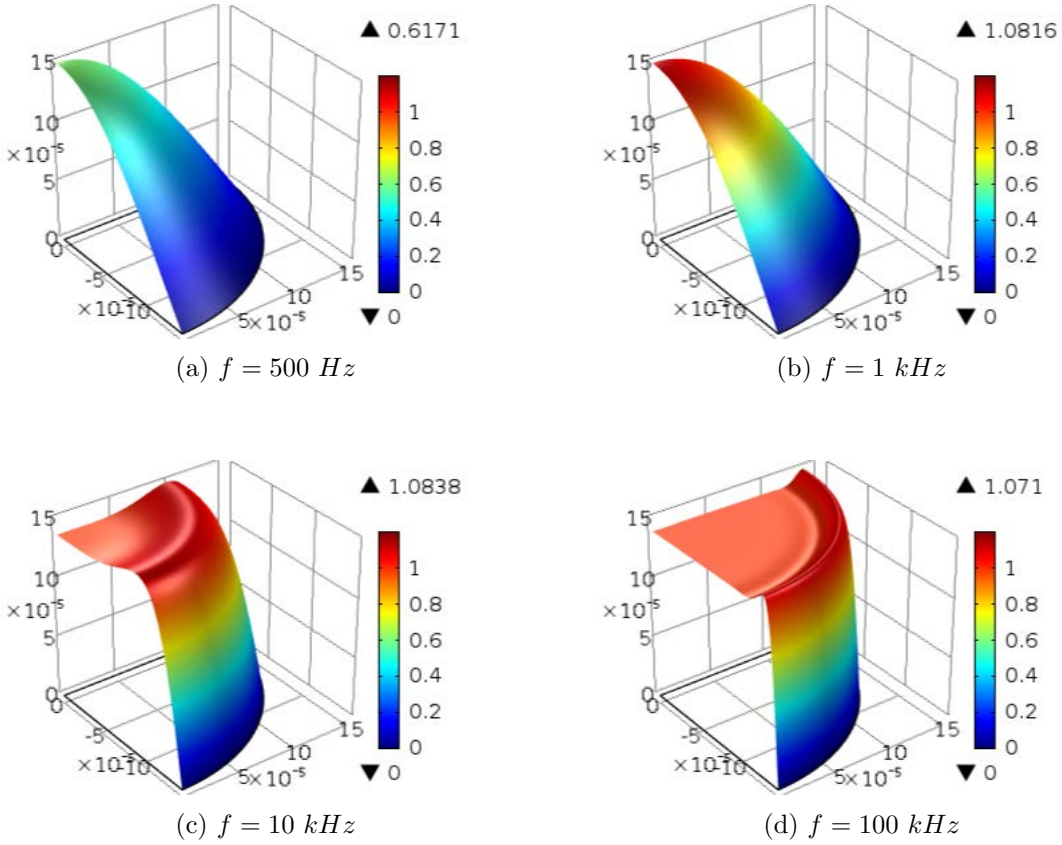

(a) $f = 500\ Hz$ (b) $f = 1\ kHz$

(c) $f = 10\ kHz$ (d) $f = 100\ kHz$

Figure 3.6: Evolution of the velocity shape function for circular vent with radius of 150 μm

Towards the pressure field

Further considerations which lead to the designation of pressure fluctuations are based on the mean values of shape functions over the section. With these mean values of shape functions for velocity and temperature $(\mathcal{Y}_v, \mathcal{Y}_\tau)$ and with modified mean temperature field $\mathcal{Y}_\tau^{'} = \gamma - (\gamma - 1)\mathcal{Y}_\tau$, R. Kampinga defines mean (lumped) velocity, temperature and density fluctuations:

$$< v >_s = -\frac{\mathcal{Y}_v}{\rho_0 j\omega}\frac{\partial p}{\partial x}, \qquad < \tau >_s = \frac{\mathcal{Y}_\tau p}{\rho_0 c_P}, \qquad < \rho >_s = \frac{\mathcal{Y}_\tau^{'} p}{c_0^2}. \tag{3.57}$$

If we consider no mean flow (as in model assumptions), the pressure field may be expressed in form of modified Helmholtz equation:

$$\frac{\partial^2 p}{\partial x^2} + k_l^2 p = 0, \tag{3.58}$$

where k_l is so-called LRF wave number defined as:

$$k_l^2 = k_0^2 \frac{\mathcal{Y}_\tau^{'}}{\mathcal{Y}_v} \qquad \text{and} \qquad k_0 = \omega / c_0. \tag{3.59}$$

Moreover with use of air acoustic impedance Z_0 R. Kampinga introduces LRF characteristic impedance Z_l:

$$Z_l^2 = \frac{Z_0^2}{\mathcal{Y}_\tau^{'}\mathcal{Y}_v} \qquad \text{and} \qquad Z_0 = \rho_0 c_0. \tag{3.60}$$

Knowing the LRF wave number we may determine the pressure field inside the domain:

$$p(x,\omega) = p_i(x,\omega) + p_r(x,\omega) = Ae^{jk_l x} + Be^{-jk_l x}, \tag{3.61}$$

where the indexes i and r denote the incident and reflected waves, A and B are the complex amplitudes. To continue we will assume that the pressure at the inlet ($p(x_1,\omega)$ denoted p_1) and the outlet ($p(x_2,\omega)$ denoted p_2) of the domain is known. We introduce the lenght of the domain $L_t = x_2 - x_1$. Then the complex amplitudes are identified:

$$\begin{bmatrix} A \\ B \end{bmatrix} = \frac{1/2j}{\sin k_l L_t} \begin{bmatrix} -e^{-jk_l x_2} & e^{-jk_l x_1} \\ e^{jk_l x_2} & -e^{jk_l x_1} \end{bmatrix} \begin{bmatrix} p_1 \\ p_2 \end{bmatrix}. \tag{3.62}$$

With the values of complex amplitudes we may describe the pressure field inside the domain:

$$p(x,\omega) = \frac{\sin k_l(x_2 - x)}{\sin k_l L_t} p_1 + \frac{\sin k_l(x - x_1)}{\sin k_l L_t} p_2 \tag{3.63}$$

and the pressure gradient:

$$-\frac{\partial p}{\partial x}(x,\omega) = k_l \left[\frac{\cos k_l(x_2 - x)}{\sin k_l L_t} p_1 - \frac{\cos k_l(x - x_1)}{\sin k_l L_t} p_2 \right]. \tag{3.64}$$

3.5 Benchmarking

Low Reduced Frequency model seems to be a good alternative that may reduce the computation cost in comparison to the FEM based on Linearized Navier-Stokes equations. To validate this model we present the benchmark where we examine the acoustic

phenomena inside the cylindrical tube (see fig. 3.7) with radius $R_t = 150$ µm and length $L_t = 0.5$ mm. Knowing the pressure p_1 and p_2 imposed at the inlet and outlet of the tube we estimate the flows to finally compare the transfer functions calculated by the subsequent models. We emphasize this geometry since R. Kampinga provided the resolution of shape functions for LRF, while FEM of LNS (Linearized Navier-Stokes) models profits on the symmetry of the tube (we can model quarter of the geometry).

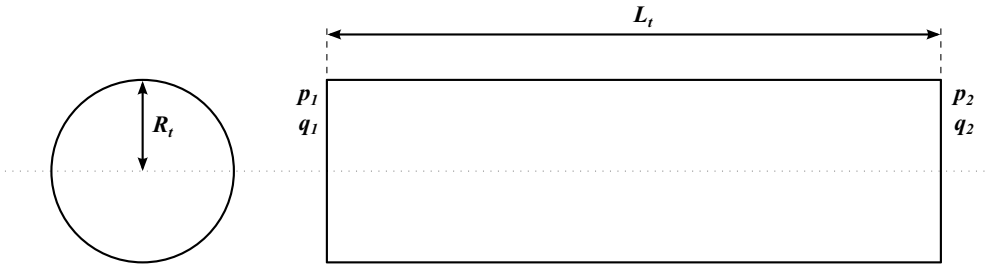

Figure 3.7: Cylindrical geometry used in acoustic models benchmark.

The constants adopted for the benchmark are gathered in table 3.2. The similar constants are used throughout this work.

Table 3.2: Constants used in acoustic simulations.

Symbol	Value	Unit	Description
T_0	298.15	$[K]$	Quiescent temperature
P_0	101325	$[Pa]$	Quiescent pressure
M_{mol}	28.8	$[g/mol]$	Molar mass of air
R	8.3144621	$[J/mol/K]$	Ideal gas constant
$r_{air} = R/M_{mol}$	288.6966	$[J/kg/K]$	Air gas constant
$\rho_0 = P_0/r_{air}/T_0$	1.1772	$[kg/m^3]$	Quiescent density
$\gamma = c_P/c_V$	1.4	[1]	Ratio of specific heats
$c_P = \gamma/(\gamma-1)r_{air}$	1010.4	$[J/kg/K]$	Specific heat at constant pressure
$c_V = 1/(\gamma-1)r_{air}$	721.7415	$[J/kg/K]$	Specific heat at constant volume
κ	25.4341	$[mW/K/m]$	Thermal conductivity
μ	18	$[\mu Pa \cdot s]$	Shear viscosity
$c_0 = \sqrt{\gamma P_0/\rho_0}$	347.1381	$[m/s]$	Speed of sound in air
$Z_0 = \rho_0 c_0$	408.6414	$[Pa \cdot s/m]$	Acoustic impedance of air

3.5.1 Finite Element Models based on Linearized Navier-Stokes equations (LNS)

In section 3.3 formulation of FLNS (Full Linearized Navier-Stokes) model has been presented. This complete model describes the acoustic phenomena by taking into account the dissipation of energy coming from the air viscosity and the thermal conductivity of air. Such model is challenging in terms of computation cost in case of the complex geometries.
In order to decrease the number of DOF (Degrees Of Freedom) we would like to compare FLNS model to the simplified one, where the energy dissipation coming from the thermal effects is neglected and the process becomes adiabatic. To obtain the simplified model all of the temperature terms from equation 3.35 are removed. In further considerations

this model is called the ALNS (Adiabatic Linearized Navier-Stokes).
Finally the models list is completed by the COMSOL Thermoacoustic module, which with minor differences (see appendix A for the details) corresponds to the FLNS.

Geometry and meshing

For the benchmark we use 3D geometry of cylindrical tube. The FEM take advantage of the geometry symmetry, thus we calculate the solution using only quarter of the cylinder (see fig. 3.8(b)). Figure 3.8 presents the mesh applied on examined geometry. For the increase of computational efficiency the swept mesh was chosen. It was created by triangular meshing of one cross-sectional face and then the reproduction of triangular mesh over the 3$^{\text{rd}}$ axis. For proper modelisation of boundary layers, the element size on the cross-section outer edge is limited to 1.5 µm (thickness of viscous boundary layer at 1 MHz is 2.18 µm) and the maximum element growth rate is set to 1.1. Complete mesh consists of 16345 domain elements and it is applicable to the simulations where the maximal frequency equals 680 kHz (limited by 7 elements per wavelength in swept mesh). As shown later, our benchmark includes the frequency up to 1 MHz, however the results for the frequencies above 680 kHz are strictly comparative (all finite elements models in the benchmark suffer of the same error).

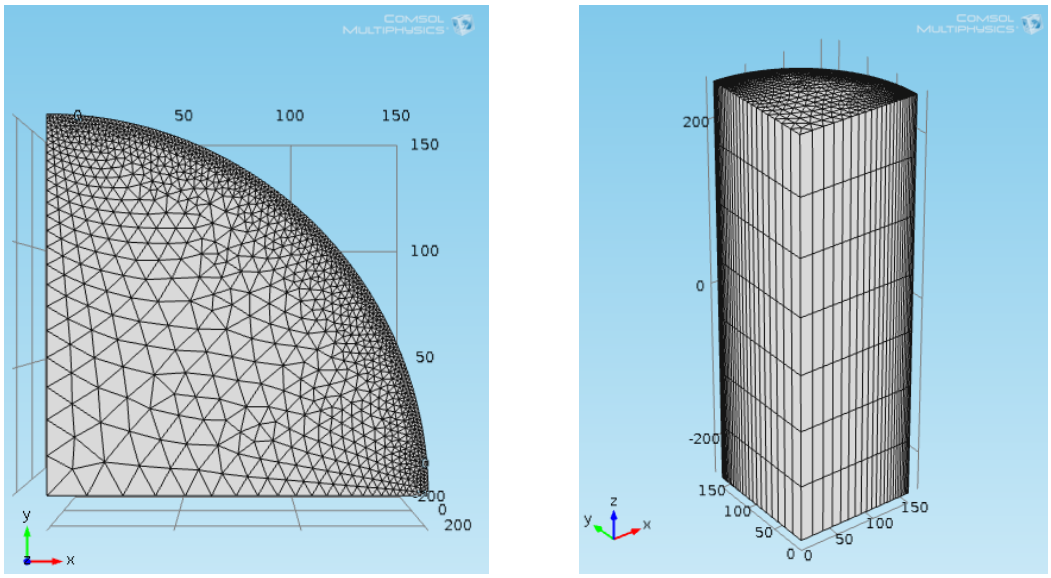

(a) Triangular mesh on geometry cross-section. (b) Sweept mesh on 3D geometry.

Figure 3.8: Meshing of 3D geometry used in acoustic models benchmark.

3.5.2 Low Reduced Frequency model

Key elements of LRF model presented in section 3.4 are the solutions of viscothermal fields Ψ_v and Ψ_τ on the geometry cross-section. For this benchmark we use the analytical solution of viscothermal fields and their mean values $\mathcal{Y}_v$ and $\mathcal{Y}_\tau$ given for cylindrical

cross-section by R. Kampinga [56]:

$$\Psi_v(r,\omega) = 1 - \frac{\mathrm{J}_0(k_v r)}{\mathrm{J}_0(k_v R_t)}, \qquad \mathcal{Y}_v = -\frac{\mathrm{J}_2(k_v R_t)}{\mathrm{J}_0(k_v R_t)}, \tag{3.65}$$

$$\Psi_v(r,\omega) = 1 - \frac{\mathrm{J}_0(k_\tau r)}{\mathrm{J}_0(k_\tau R_t)}, \qquad \mathcal{Y}_\tau = -\frac{\mathrm{J}_2(k_\tau R_t)}{\mathrm{J}_0(k_\tau R_t)}, \tag{3.66}$$

where $\mathrm{J}_0, \mathrm{J}_2$ are the Bessel functions of the first kind where the subscript denotes their order; r varies between 0 and R.
The flow rate q which equals the integral of velocity over the surface is designated from the combination of equation 3.57 and 3.64:

$$q(x,\omega) = -\frac{S_{cs}\mathcal{Y}_v}{\rho_0 j\omega}\frac{k_l}{\sin k_l L_t}\left[\cos k_l(x_2 - x)p_1 - \cos k_l(x - x_1)p_2\right], \tag{3.67}$$

where S_{cs} is the surface of the tube cross-section. We modify equation 3.67 with use of the identity $\rho_0\omega = k_0 Z_0$ and we denote the flow outgoing the tube on the input (q_1) and on the output (q_2):

$$q_1 = \frac{S_{cs}\mathcal{Y}_v}{jk_0 Z_0}\frac{k_l}{\sin k_l L_t}\left[\cos k_l L_t p_1 - p_2,\right], \tag{3.68}$$

$$q_2 = -\frac{S_{cs}\mathcal{Y}_v}{jk_0 Z_0}\frac{k_l}{\sin k_l L_t}\left[p_1 - \cos k_l L_t p_2\right]. \tag{3.69}$$

We may represent equation 3.68 and 3.69 as a system of equations:

$$\begin{bmatrix} q_1 \\ q_2 \end{bmatrix} = \frac{S_{cs}\mathcal{Y}_v}{jk_0 Z_0}\frac{k_l}{\sin k_l L_t}\begin{bmatrix} \cos k_l L_t & -1 \\ -1 & \cos k_l L_t \end{bmatrix}\begin{bmatrix} p_1 \\ p_2 \end{bmatrix} \tag{3.70}$$

and the input admittance of the system is:

$$\frac{q_1}{p_1} = \frac{S_{cs}\mathcal{Y}_v}{jk_0 Z_0}\frac{k_l}{\tan k_l L_t}. \tag{3.71}$$

Following the example of A.D. Pierce [55] we represent the circular tube as a two-port element with acoustic impedance Z_d and acoustic compliance Y_c (see figure 3.9). To

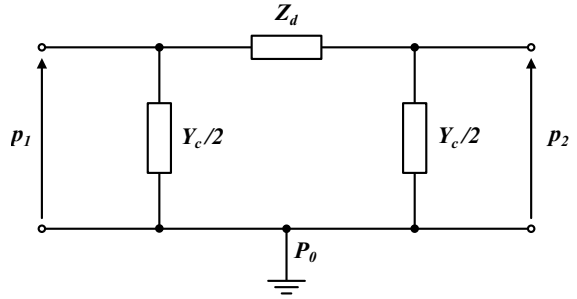

Figure 3.9: Simplified representation of circular tube as a two-port element.

identify acoustic impedance and acoustic compliance that appear under two different circumstances A.D. Pierce [55] investigates two cases:

First case: $Y_c \to \infty$

The length of the tube is much smaller than the acoustic wavelength, the flow inside the tube is nearly incompressible. In this case we demonstrate the impedance behavior of the tube and since the flow is nearly incompressible the acoustic compliance goes to infinity and it is replaced by open circuit (fig. 3.10(a)).

Second case: $Z_d \to 0$

In the second case the air is compressed inside the tube and the value of air flowing outside the tube is null. The acoustic impedance in this case approaches zero, therefore it is treated as short-circuit and Y_c is the only element describing the acoustic behavior of the tube (fig. 3.10(b)).

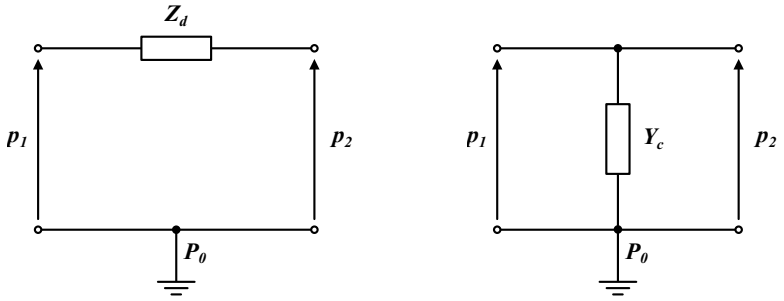

(a) First case: $Y_c \to \infty$ (b) Second case: $Z_d \to 0$

Figure 3.10: Two different representation of circular tube regarding its acoustic behavior.

In practice, to demonstrate the first case with use of equation 3.70 we need to establish the flow passing through the tube - excite the enclosed air in differential mode ($p_1 = -p_2$). On the other hand to demonstrate the second case we need to compress the air inside the tube - thus the air must be excited in common mode ($p_1 = 1$, $p_2 = 0$). If we separate the differential and the common mode excitation, the equation 3.70 becomes:

$$\begin{bmatrix} q_1 \\ q_2 \end{bmatrix} = \frac{S_{cs}\mathcal{Y}_v k_l}{jk_0 Z_0} \frac{1}{\sin k_l L_t} \begin{bmatrix} 1 & -1 \\ -1 & 1 \end{bmatrix} \begin{bmatrix} p_1 \\ p_2 \end{bmatrix} + \left(-\frac{S_{cs}\mathcal{Y}_v k_l}{jk_0 Z_0} \frac{1-\cos k_l L_t}{\sin k_l L_t} \right) \begin{bmatrix} 1 & 0 \\ 0 & 1 \end{bmatrix} \begin{bmatrix} p_1 \\ p_2 \end{bmatrix}, \tag{3.72}$$

where the expressions that precede the matrices corresponds to the acoustic admittance $1/Z_d$ and the acoustic compliance Y_c:

$$Z_d = \frac{jk_0 Z_0}{S_{cs}\mathcal{Y}_v k_l} \sin k_l L_t, \tag{3.73}$$

$$Y_c = -\frac{S_{cs}\mathcal{Y}_v k_l}{jk_0 Z_0} \frac{1-\cos k_l L_t}{\sin k_l L_t}. \tag{3.74}$$

3.5.3 Results discussion

Table 3.3 summarizes the cost of the compared models. Under this terms the LRF model is clearly the best choice for the users with limited resources that at the same time would like to keep the high resolution (number of frequencies). The FEM solutions are significantly more expensive. Finite element analysis were made with use of machine with 10 CPUs and they require 9 - 13 gigabytes of RAM. The number of frequencies was limited to the minimal value that enabled us to compare the models based on FEA with LRF. Nonetheless the simulations have taken from 30 minutes in case of the ALNS

model (omit of temperature terms reduces the number of DOF) to 60 minutes in case of FLNS and commercial COMSOL Thermoacustic models which use full set of linearized Navier-Stokes equations.

Table 3.3: Comparison of model computation cost.

		Model			
Feature	Unit	LRF	ALNS	FLNS	COMSOL Thermoacoustic
DOF	[1]	-	229588	302728	302728
Number of frequencies	[1]	1200	61	61	61
Physical memory	[GB]	0.01	9.44	13.26	13.14
Virtual memory	[GB]	-	14.76	18.26	18.76
Solution time	[min]	0.05	33	58	60

Bode plot of the input admittance (fig. 3.11) gathers the transfer functions for the frequencies from 10 Hz to 1 MHz calculated with subsequent models. The shapes of magnitude plots are similar in all the cases and only the COMSOL Thermoacoustic model shows minor nonconformity on the phase plot. However the magnitude of LRF model is slightly higher (10 dB) for all the frequencies. To understand this shift of LRF magnitude one need to remember that in case of LRF model we neglect the fluid velocity in cross-sectional directions. This simplification reduces the energy dissipation through viscous effects and results in overestimation of the tube admittance. On the contrary

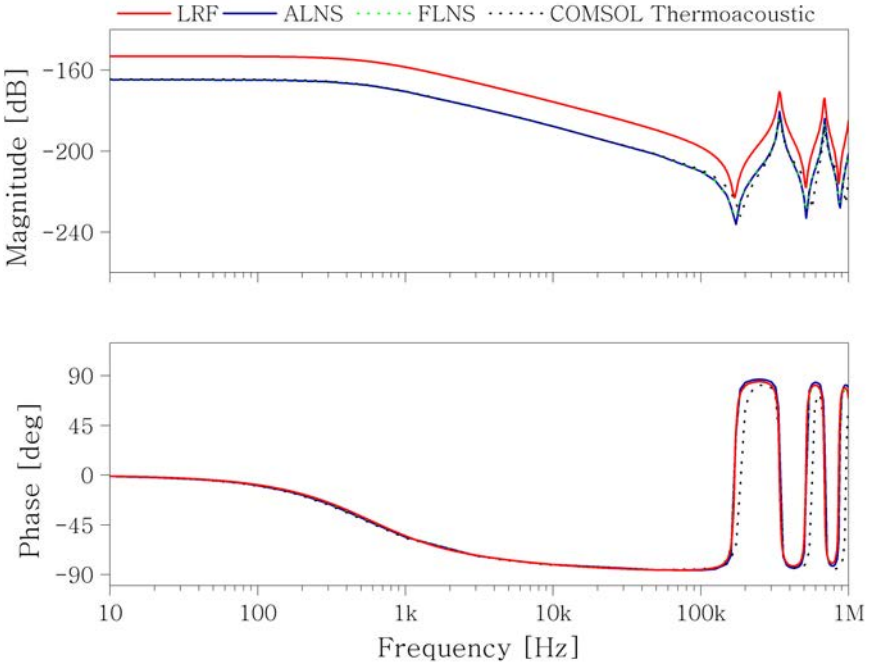

Figure 3.11: Bode plot of the input admittance (q_1/p_1).

the 3D FEM models evaluate the velocity in every dimension and the admittance given by those models is more precise. Figure 3.12 presents the velocity field distribution in the tube. The module of velocity in propagation direction (longitudinal velocity) is constant throughout the tube length (fig. 3.12(a)) while the velocities in cross-sectional plane (radial velocity) have their maximum in the vicinity of the inlet and outlet of the tube (fig. 3.12(b)).

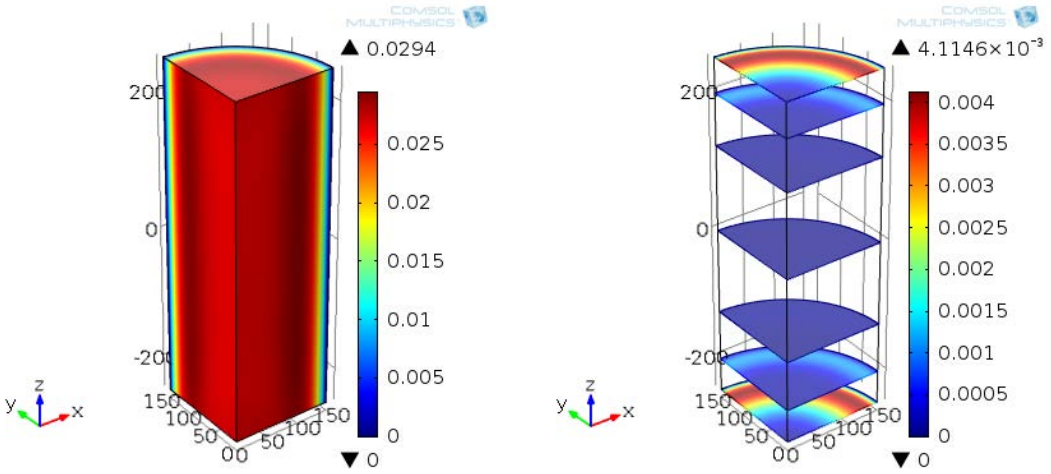

(a) Module of longitudinal fluid velocity.

(b) Module of radial fluid velocity.

Figure 3.12: Velocity field distribution in the tube, f = 10 kHz.

Figure 3.13 presents the same results as figure 3.11, however it focuses on the acoustic resonances. Difference in magnitude between ALNS, FLNS and COMSOL Thermoacoustic models is displayed. ALNS presents slightly higher magnitude in the vicinity of acoustic resonances since the energy is not dissipated by thermal effects.

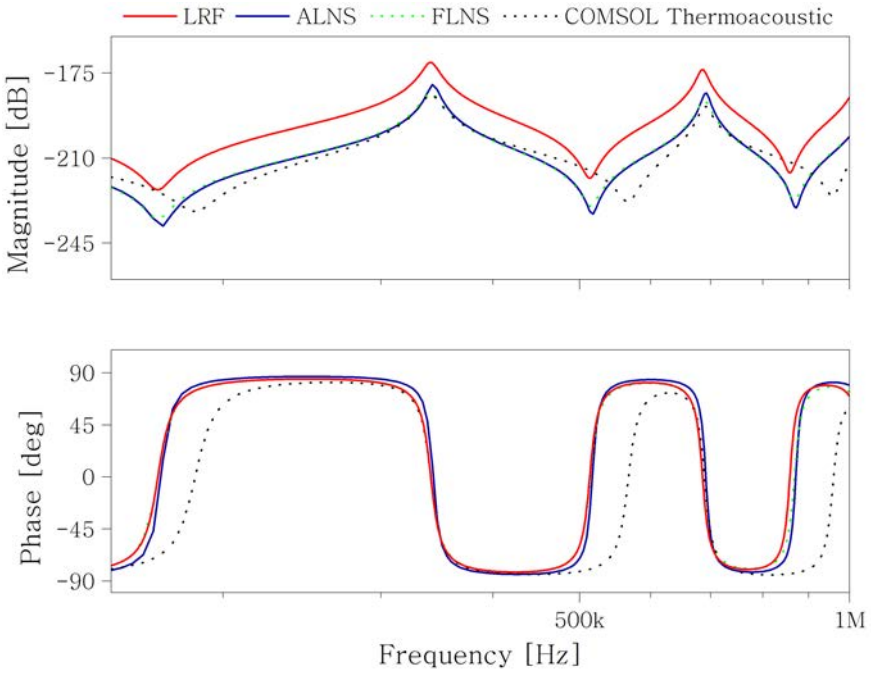

Figure 3.13: Bode plot of the input admittance (q_1/p_1) focused on acoustic resonances.

It has been proven that Low Reduced Frequency model is reliable replacement of Finite Element Analysis for fast analysis of acoustic phenomena. It is true that this approach becomes problematic for the geometries with complicated cross-sections where the analytical resolutions of shape functions are not available. However for those geometries the shape functions Ψ_v and Ψ_τ might be calculated numerically.

It is then possible to evaluate the acoustic system with use of LRF model to adjust the critical parameters of the system. At the end of design process the LRF-based simulations can be enriched with use of finite element analysis to obtain the precise values of the admittance.

3.6 Towards Lumped Element model

Lumped element modeling is a common technique used in modelisation of variety of physical properties with use of analogy to simple mechanical system or discrete electronic elements (if we use electronic elements the model is commonly called the Equivalent Circuit model). The theoretical background of Lumped Element model in acoustic field can be found in books of A.D. Pierce and M. Bruneau [54, 55]. Analogies of general physical properties to their equivalents in fluidics, mechanics and discrete electronics are gathered in table 3.4. We have decided to represent the acoustic elements with discrete elements of electrical system. With this approach we may simulate the system analytically or - in case of complex systems - with use of MATLAB or SPICE software.

Table 3.4: Lumped analogies of the physical properties [68]

General	Fluidic	Mechanical	Electrical
Effort	Pressure	Force	Voltage
Flow	Vol. flow rate	Velocity	Current
Displacement	Volume	Displacement	Charge
Momentum	Pressure Momentum	Momentum	-
Resistance	Fluid resistance	Damper	Resistor
Capacitance	Fluid compliance	Spring	Capacitor
Inertance	Inertance	Mass	Inductor

3.6.1 Validation of Lumped Element model

At the end of subsection 3.5.2 we have introduced the acoustic impedance and compliance of circular tube. Basing on this two elements we may identify the electrical representation of two-port element (fig. 3.14) analogous to fig. 3.9. To obtain the ex-

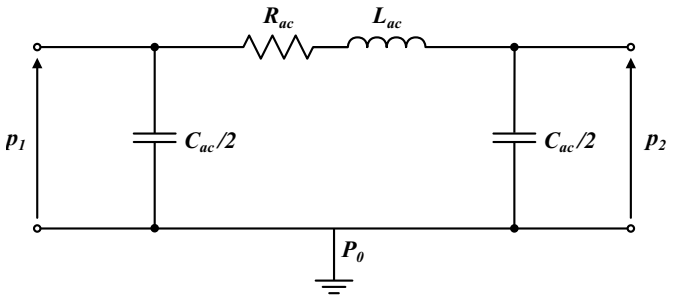

Figure 3.14: Electrical representation of two-port acoustic element.

pressions of lumped resistance R_{ac}, inductance L_{ac} and capacitance C_{ac} we search for

approximation of impedance (eq. 3.73) and compliance (eq. 3.74) about $\omega = 0$. The simplified expressions of lumped parameters for circular tube becomes:

$$R_{ac} = \frac{8\mu L_t}{\pi R_t^4}, \qquad L_{ac} = \frac{4\rho_0 L_t}{3\pi R_t^2}, \qquad C_{ac} = \frac{L_t \pi R_t^2}{2P_0\gamma} \tag{3.75}$$

and with use of lumped parameters the input admittance of the tube is expressed with the following formula:

$$\frac{q_1}{p_1} = \frac{1}{R_{ac} + j\omega L_{ac}} + j\omega C_{ac}. \tag{3.76}$$

To validate the identified lumped elements we trace again the input admittance of the circular tube (fig. 3.15). We use the similar geometry to the one from the benchmark. The admittance of both - LRF and Lumped Element model is coherent nearly till the frequency of 100 kHz. Keeping in mind that the microphone bandwidth is 20 - 20 kHz, the Lumped Element model is applicable to the simulations of this kind of sensors.

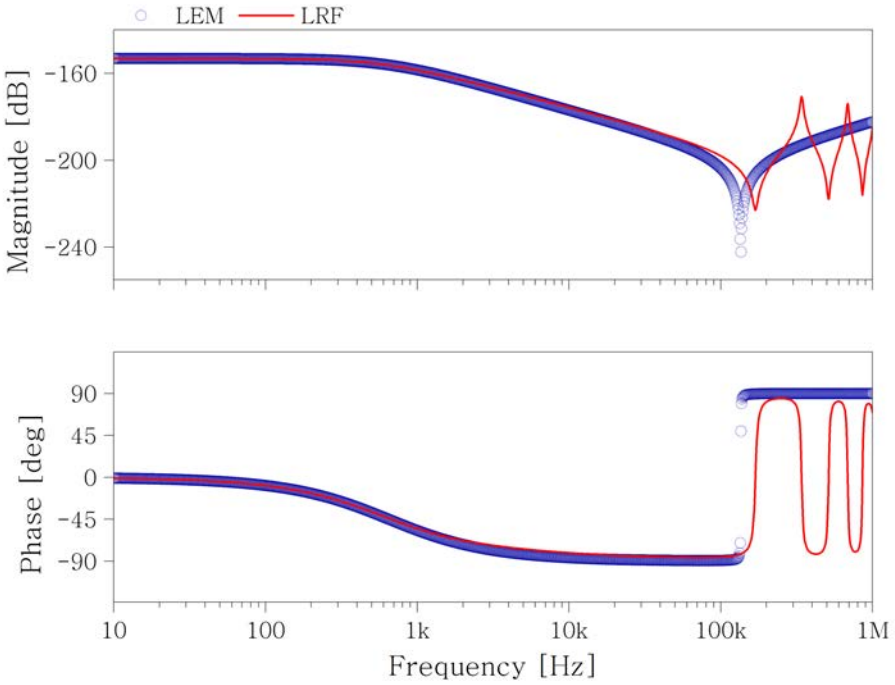

Figure 3.15: Comparison of the admittance obtained with the LRF and with Lumped Element model.

3.6.2 Acoustic resistance of rectangular guide

As far we have shown how to identify the lumped elements for the circular tube, however the new architecture of the MEMS microphone investigated in this thesis consists of the acoustic elements that have a rectangular cross-section. If one of the rectangle sides is much larger than the other one (A $\ll$ B - for illustration of A and B please see fig. 3.16) the geometry can be approximated as a slit (layer). In this case we can analytically describe the shape functions and their means values, then the acoustic resistance can be calculated in the similar way as in case of the circular tube and it equals [54]:

$$R_{ac} = \frac{12\mu L_r}{BA^3}, \tag{3.77}$$

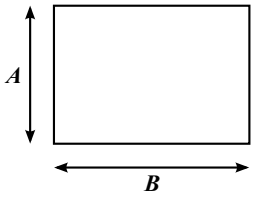

Figure 3.16: Cross-section of the rectangular acoustic elelemnt.

where L_r denotes the length of the guide in the sound propagation direction. However what can we do to identify the lumped elements when A and B are of comparable dimensions? This problem can be resolved with use of LRF model, for example the viscous resistance R_{ac} may be identified with equation 3.73 for the Ψ_v and Ψ_τ solved in FEA solver at low frequency.
To begin we have verified this approach by comparison of equation 3.73 and 3.75 on the example of the circular tube. The results on figure 3.17 shows that the viscous resistance identified with FEA solution is correct and we can apply it to other types of sections.

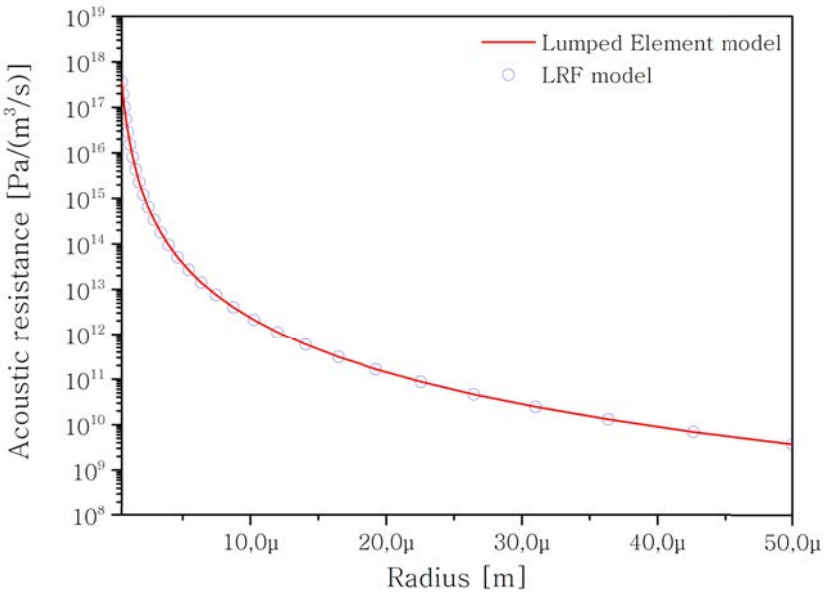

Figure 3.17: Acoustic resistance of the cylindrical tube as a function of radius R. The length L_t of the tube is 500 µm.

We have prepared the same type of simulations for the rectangular guide where the side lengths A and B were in rage of 0.5 - 50 µm. As a result we have obtained the color map of the acoustic resistance (fig. 3.18). The figure highlights the importance of the thermal and viscous boundary layers especially for the geometries smaller than 10x10 µm where the viscous resistance rises drastically.

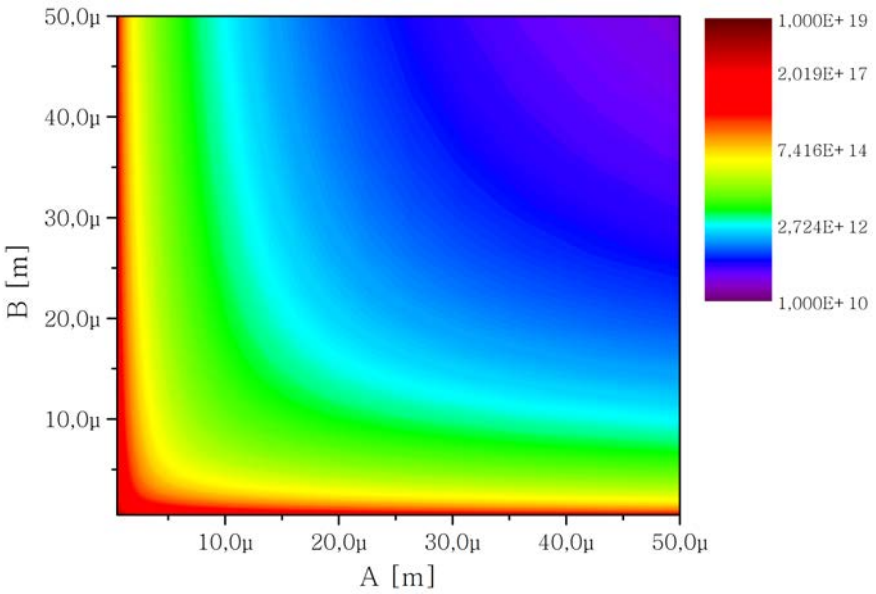

Figure 3.18: Acoustic resistance of the rectangular guide as a function its side length A and B. Color legend indicates the acoustic resistance with the units [Pa/(m^3/s)]. The length L_r is set to 500 µm.

Summary

We have gone through the set of models that may be used to investigate the acoustic behavior of the MEMS microphone. Despite the high computational costs of the models based on Finite Elements Method, these models seems to be the wisest and quickest way to understand the acoustic phenomena at the microscale. At the end of this chapter we have reached the representation of the acoustic phenomena in form of the equivalent electrical circuit. In the next chapter we apply these two models to the design considerations of the new MEMS microphone architecture. We start with the simulations of the microphone with use of the FLNS model, then - with the knowledge acquired thanks to FEA, we construct the model of investigated microphone in form of the electronic circuit.

Chapter 4

Sensor design considerations

In the following chapter we focus on the design of the new MEMS microphone. We now use FLNS model with fluid-structure interaction to predict the microphone frequency response and to detect the crucial factors that have an influence on it. Afterward we discuss the mechanical structure and demonstrate how to represent complicated truss beam in 2D. Coupling between the microphone subsystems (acoustical, mechanical and electrical systems) enabled us to present the microphone sensitivity with three different models: 2D, 3D FLNS models and with Lumped Element model. The last model is subsequently used to analyze the noise sources that restrict the lower limit of signal detection. Finally we shortly discuss the influence of technological dispersion (overetch) and the mechanical shocks on the microphone functioning.

4.1 Architecture properties of considered MEMS

Overall view

Considered MEMS (fig. 4.1(a)) has overall dimensions of 1.5x1.5x0.6 mm^3, it consists of 4 micro-beams placed between the inlet vents and the outlet vents (fig. 4.1(b)). These beams move rotationally in plane of a Silicon wafer - the axis of rotation coincides with the vector normal to the surface of a wafer.

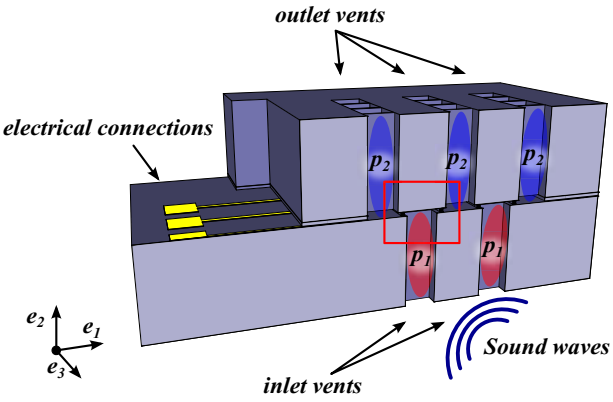

(a) Overall view

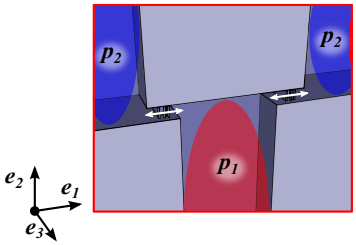

(b) Location of two out of four microbeams

Figure 4.1: Cross-sectional view of MEMS dice.

MEMS dice is then packaged; typical chip-scale package showed on fig. 4.2 includes two separated chips which are MEMS and ASIC (Application-Specific Integrated Circuit).

Integrated circuit amplifies sensor signal and furnishes it in analog or digital output form.

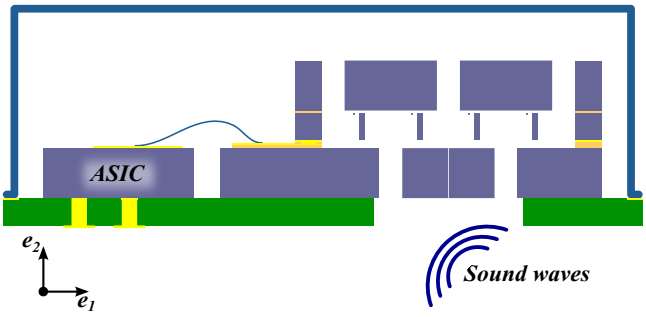

Figure 4.2: Bottom port configuration of MEMS microphone package (not to scale).

Standard PCB (Printed Circuit Board) is used as a support and metal, cup-shaped lid is used for package sealing. Depending on a sound port position we distinguish two package configurations called the top port and the bottom port. For the M&NEMS microphone considerations the bottom port configuration has been chosen. The package introduces the acoustic cavity into the microphone. The volume of this cavity called the backvolume is obtained by deducting the volumes of the MEMS and the ASIC chips from the internal volume of the package. The influence of the backvolume is considered in the microphone design.

Acoustic system

The cross-section of the MEMS dice acoustic system along with the symbols of each dimension are presented on fig. 4.3. Microbeams are placed between two silicon wafers

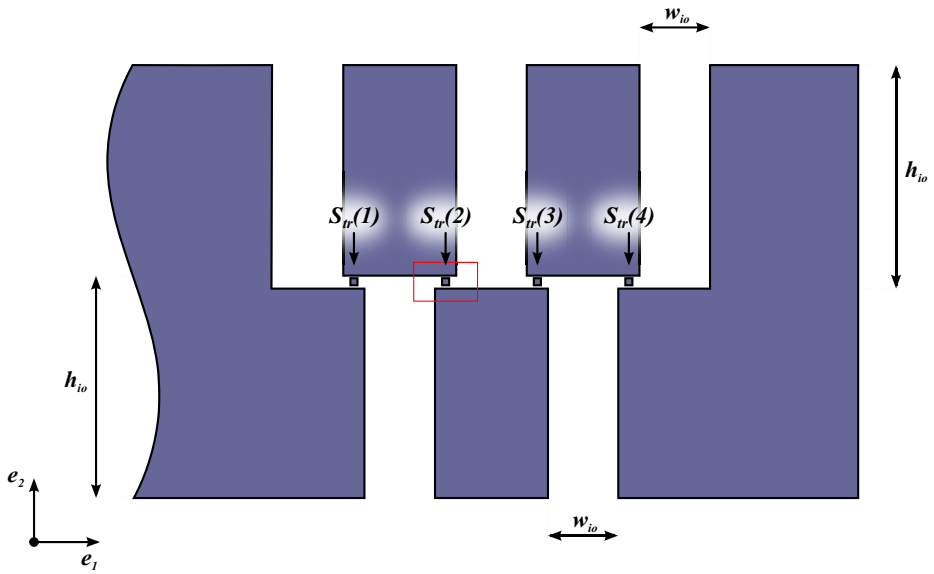

Figure 4.3: The cross-section of the MEMS dice with view on the acoustic system. One can see two inlets and three outlets. All of the inlets and outlets have the same dimensions.

(fig. 4.4). This architecture introduces the viscous damping that is related to the gaps a and b localized above and below the beam. The dimensions of the elements of acoustic system are listed in the table 4.1.

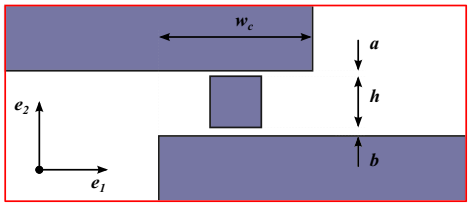

Figure 4.4: Cross-section of the beam and the surrounding wafers (so-called "coupler").

Table 4.1: Dimensions of the acoustic system

Symbol	Value	Unit	Description
l_{io}	740	$[\mu m]$	Length of the inlet and outlet vents along the e_3 axis (out of plane dimension of fig. 4.3)
h_{io}	313	$[\mu m]$	Height of the inlet and outlet vents
w_{io}	100	$[\mu m]$	Width of the inlet and outlet vents
a	1	$[\mu m]$	Height of the gap between the beam and SOI wafer
b	2	$[\mu m]$	Height of the gap between the beam and sealing wafer
h	10	$[\mu m]$	Height of the beam (defined by epitaxial layer)
w_c	30	$[\mu m]$	Width of the couplers
V_{ar}	7.65	$[mm^3]$	Backvolume

Mechanical system

Our investigations concern two types of the diaphragms: the first type is the simple beam (fig. 4.5) while the second one (fig. 4.6) it is a beam constructed with use of truss elements. Both beams are suspended in the same manner, moreover the truss beam architecture maintains the same mass that the one of the simple beam. Piezoresistive gauge is attached to the movable element at one extremity while the other side is anchored. Nanogauge is situated along the line between the center of rotation and center of inertia of the beam. The dimensions of the beams used in the project are summarized in table 4.2.

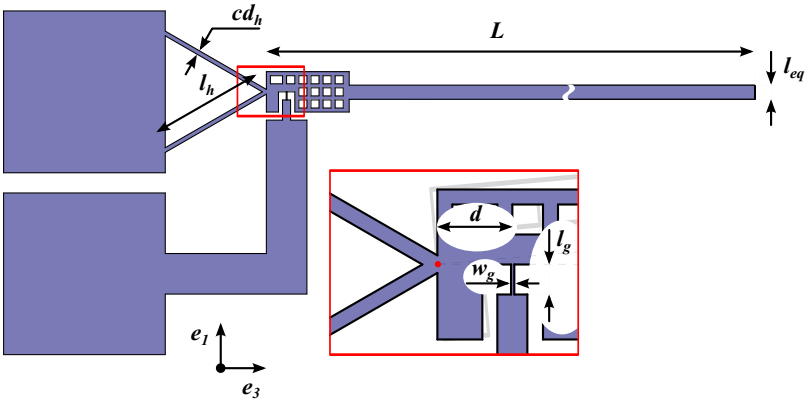

Figure 4.5: Top view of the simple beam.

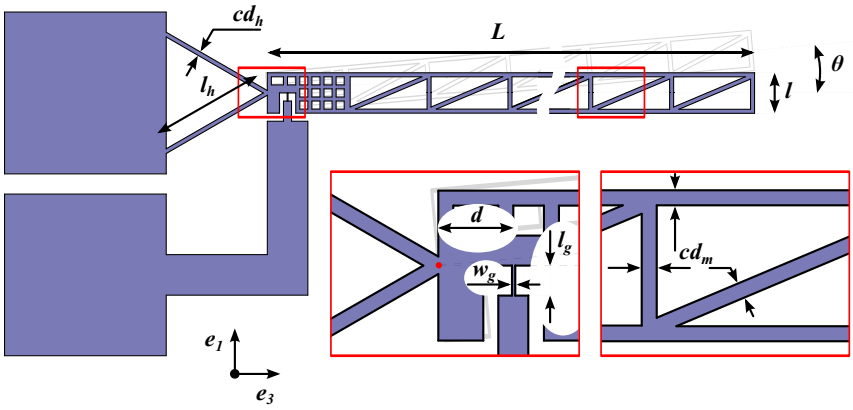

Figure 4.6: Top view of the truss beam.

Table 4.2: Dimensions of the beams

Symbol	Value	Unit	Description
L	740	$[\mu m]$	Length of the beam
l_{eq}	3.52	$[\mu m]$	Width of the simple beam
l	10	$[\mu m]$	Overall width of the truss beam
h	10	$[\mu m]$	Height of the beam (defined by epitaxial layer)
d	4	$[\mu m]$	Distance between the center of rotation and the center of the nanogauge
l_g	2	$[\mu m]$	Length of the nanogauge
w_g	250	$[nm]$	Width of the nanogauge
h_g	250	$[nm]$	Height of the nanogauge
l_h	30	$[\mu m]$	Length of the hinge member
cd_h=cd_m	1	$[\mu m]$	Width of the hinge and beam member respectively

Electrical system

Electrical system of the discussed sensor consists of four piezoresistive nanogauges. They are arranged into the Wheatstone bridge architecture that was discussed in subsection 2.2.2. The bridge may be biased with constant current or constant voltage (see fig. 4.7).

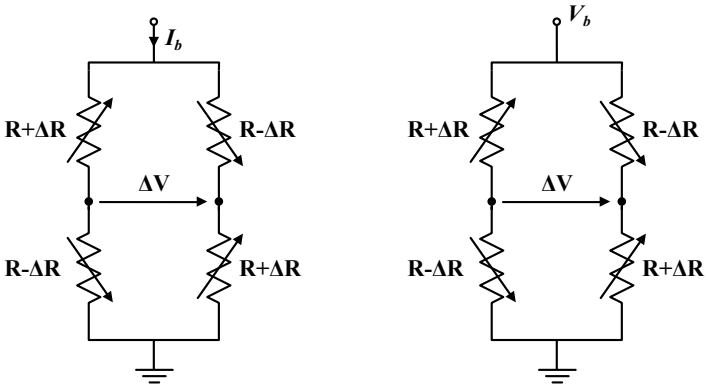

Figure 4.7: Wheatstone bridge architecture used in MADNEMS sensor.

The electrical specifications of the considered electrical system are gathered in table 4.3.

Table 4.3: Electrical specifications of designed sensor.

Symbol	Value	Unit	Description
R	4.46	$[k\Omega]$	Nominal resistance of the nanogauges
I_b	100	$[\mu A]$	Bias current of the Wheatstone bridge
V_b	0.446	$[V]$	Bias voltage of the Wheatstone bridge
Material properties			
N	$5 \cdot 10^{18}$	$[cm^{-3}]$	Impurity concentration (p-Si)
π_{pzr}	0.4	$[1/GPa]$	Piezoresistive coefficient of Silicon

4.2 Transduction chain - assemble of the microphone subsystems

The previous section introduced the elements of the considered microphone - the acoustic system of the MEMS dice, the chip-scale package, the mechanical structure and the electrical system. This elements have to be assembled in order to estimate the microphone transfer function. Transduction chain presented on figure 4.8 includes the relations between the systems:

- acoustic system of the MEMS dice have three inputs (p_1, p_2 and q_m) and three outputs (q_1, q_2 and Δp).
- The influence of the backvolume is coupled to the acoustic system by the feedback, the pressure p_2 is estimated with use of the flow rate q_2 that enters the backvolume.
- The mechanical system is coupled to the acoustic system with use of the pressure gradient Δp generated across the microbeams. Mechanical system introduces to

the acoustic system the flow rate q_m generated by the movement of the beams. Mechanical system is coupled to the electrical system by the longitudinal stress σ_g generated inside the nanogauges.

- Internal stress of a nanogauge results in the variation of the nanogauge resistance that is specified by the piezoresistive effect. Finally, the resistance variations may be interpret by Wheatstone bridge that is biased with current I_b and provides an output voltage ΔV.

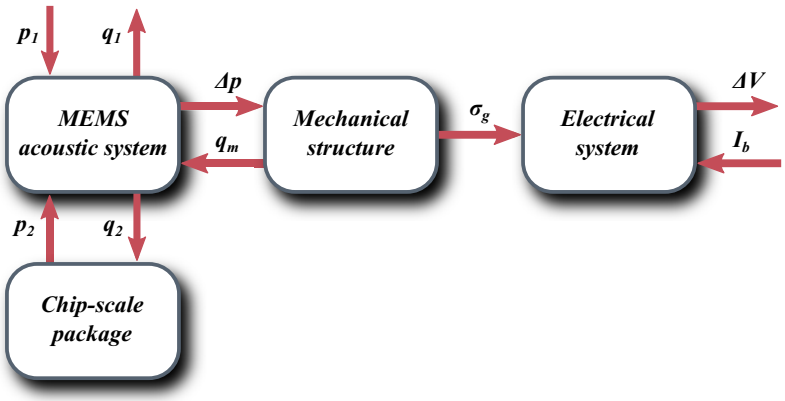

Figure 4.8: Transduction chain of the M&NEMS microphone.

4.3 2D finite element analysis of MEMS with fluid-structure interaction

Dimensions of designed microphone ranges from 1 mm down to 1 µm. The smallest acoustic elements are the slits situated above and below the beam (fig. 4.4). Their dimensions $a = 1$ µm and $b = 2$ µm are much smaller than the thicknesses of thermal and viscous boundary layers (illustrated on fig. 3.3) for the targeted sensor bandwidth (20Hz to 20kHz). Detailed analytical and FEM models that investigate thermoviscous effects have been prepared within the MADNEMS microphone project and presented by C. Guianvarc'h and T. Verdot [61, 62]. Using a simplified model for moving beams, these models handle fluid-structure interactions.

4.3.1 Structure of the model

Acoustic and thermal boundary conditions

We present the cross-section of the MEMS chip on fig. 4.9 with the boundary conditions that are required to meet the acoustic and mechanical behavior of the device. Therefore most of the surfaces of the acoustic system are simulated as the isothermal wall (non-slip conditions and no temperature variations); we impose the pressure p_1 at the MEMS inlet and p_2 at the MEMS outlet.

Fluid-Structure Interaction (FSI)

Closer look on the couplers, where the fluid-structure interaction is realized is presented on the figure 4.10. The velocity of the fluid and the beams on the fluid-structure interface

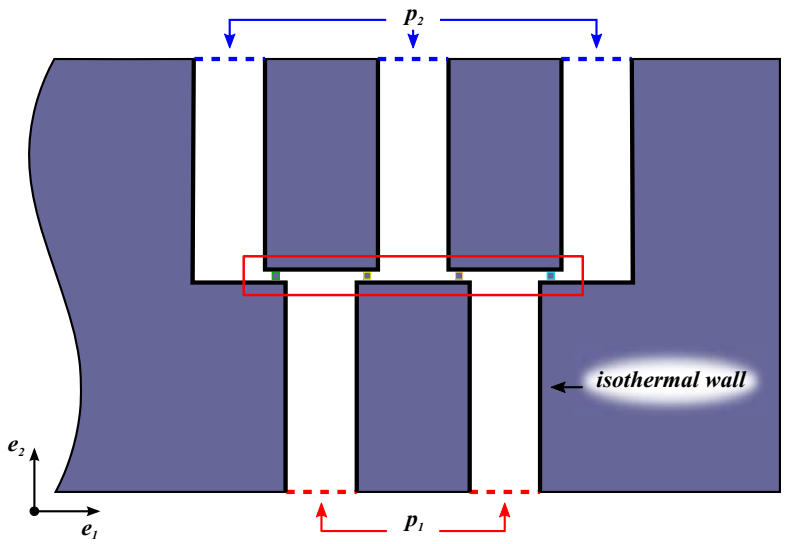

Figure 4.9: Cross-sectional view of MEMS with boundary conditions indicated.

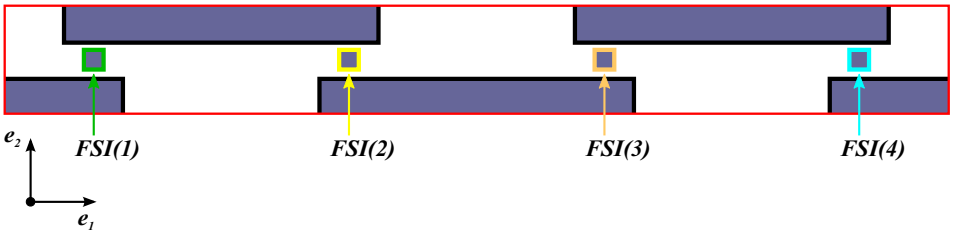

Figure 4.10: Closer view on the "couplers".

(the countour of the beam) is set to be equal:

$$\frac{L}{2}\dot{\theta} - \mathbf{v} = 0 \tag{4.1}$$

and it is a resultant of the beam movement driven by the acoustic pressure fluctuations where both mechanical and acoustical problems are solved independently. The mechanical behavior of the beams is governed by the analytical model (presented in subsection 4.4.1) and introduced into the FEM with use of ordinary differential equations. The displacement of the beams in 2D model is approximated by the average displacement of the rotating beam (fig 4.11).

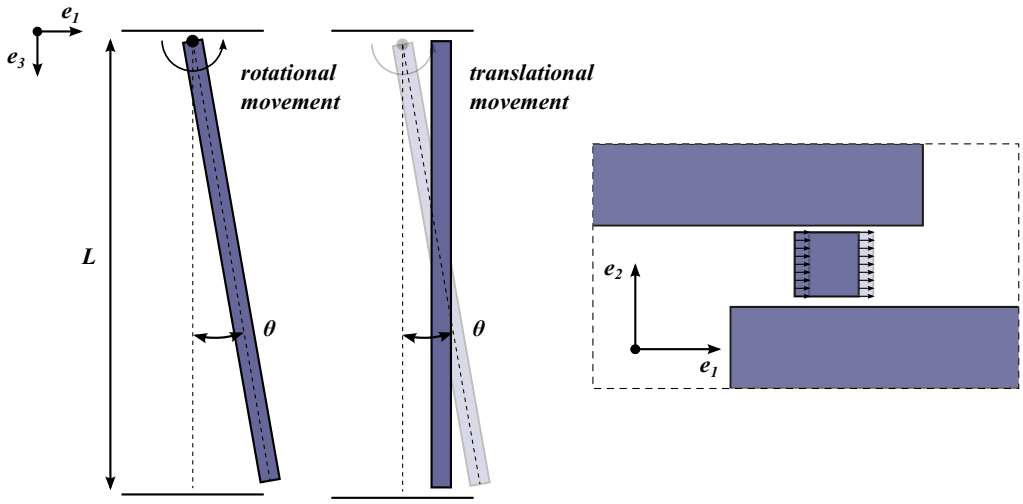

Figure 4.11: Representation of rotationall movement of the beam in 2D.

Meshing

The mechanical behavior of the beams is model analytically, thus the meshing is limited to the acoustic domains and the beams remain not meshed. We employ anisotropic mesh, which is adjusted on the boundaries to simulate reliably the boundary effects. The smallest thickness of boundary layers over the audible bandwidth equals 15 µm for 20 kHz. Therefore the maximal size of the mesh elements on the boundaries is restrained to 5 µm so that the boundary layers are covered by three elements in the worst case (fig. 4.12). The smallest elements of acoustic system are located above and below the beams. This part of the acoustic domain is meshed much more finely, the maximum dimension of elements is restrained to 0.5 µm (fig. 4.13). Comprehensive studies on the strategy of meshing for the viscothermal models were presented by N. Joly [58].

4.3.2 Discussion on the MEMS chip acoustic properties

Initial verification of the fluid-structure interaction is possible by investigation of the input admittance $Y_{11}(\omega) = q_1(\omega)/p_1(\omega)$ of the MEMS chip (fig. 4.14). We have investigated two cases:

first case: the beams are fixed and their boundaries are simulated as a wall;

second case: the beams are moving and the fluid-structure interation is introduced.

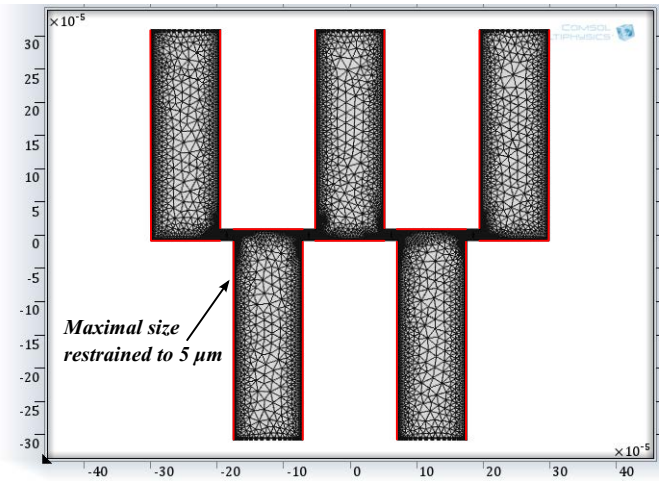

Figure 4.12: Overall view on the mesh.

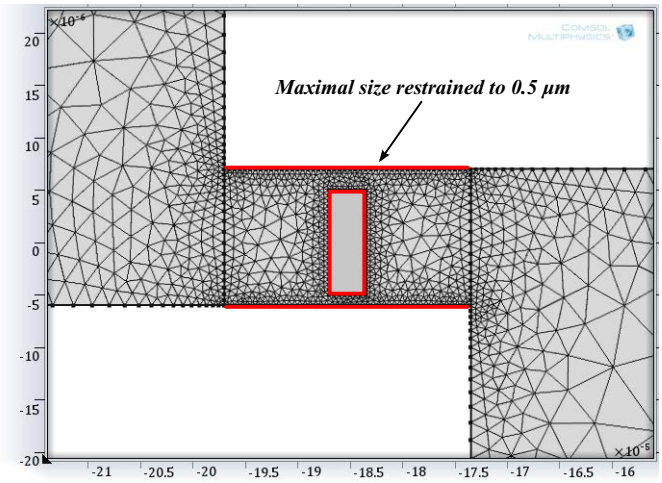

Figure 4.13: Mesh in vicinity of the beams.

The comparison of the admittances shows that the characteristics of the systems are the same at low frequency (f <2 kHz), where the viscous resistance prevails and at the high frequency (f >100 kHz) where we observe the fluid compression inside the MEMS followed by the acoustic resonances. What distinguish the admittance of the model with moving beams is the increase of acoustic admittance between 10 and 20 kHz. Over this section the admittance is dominated by the flow generated by the mechanical structures that resonate at 16 kHz.

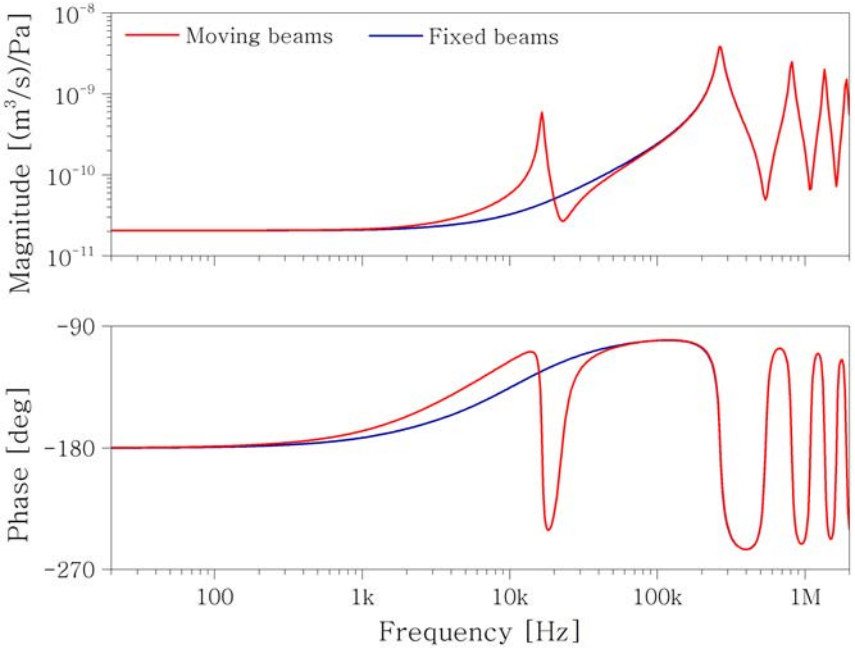

Figure 4.14: Comparison of input admittance with moving and fixed beams.

Graphic representation of the pressure and velocity fields gives another information on the system. Figure 4.15 focuses on harmonic solutions (pressure fluctuations and velocity field) computed at 1 kHz and 16 kHz. These solutions highlight two types of behavior:

- at low frequency when velocity of a beam remains weak air velocity in the slits is mainly governed by the prescribed difference of pressure (velocity profile is similar to the Poiseuille parabolic flow).
- In the vicinity of mechanical resonance of a structure (16 kHz), beam velocity affects air velocity in the slits and the velocity field become similar to the Couette flow (whose velocity profile is linear through the thickness of the slit).

These studies presented in papers by C. Guianvarc'h and T. Verdot [61, 62] prove that viscous effects occurring in the small slits generate and maintain a pressure drop across the beams.

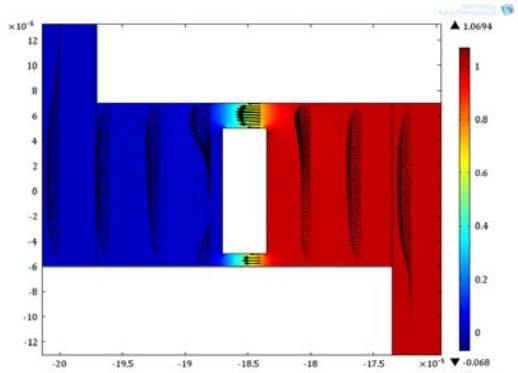

(a) Surface graph of pressure field with the arrows indicating velocity field at 1 kHz.

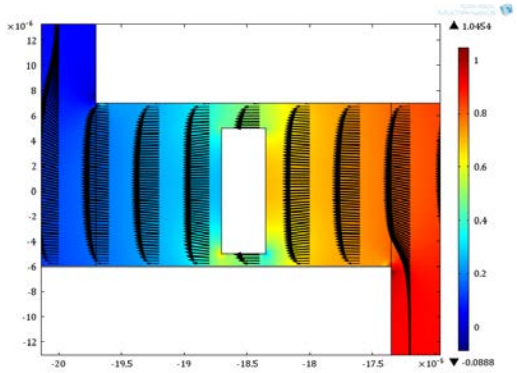

(b) Surface graph of pressure field with the arrows indicating velocity field at 16 kHz.

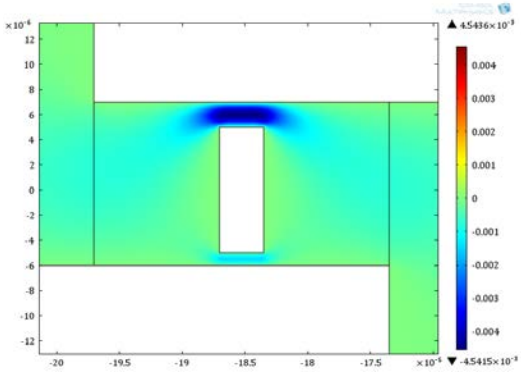

(c) Surface graph of velocity field at 1 kHz.

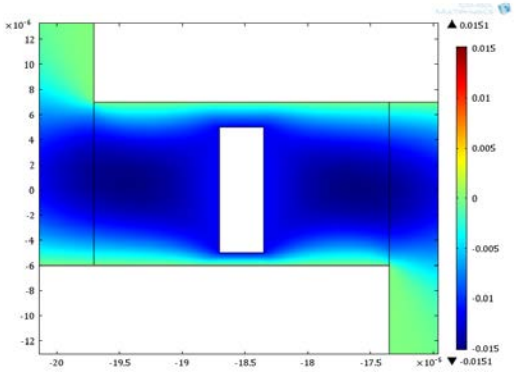

(d) Surface graph of velocity field at 16 kHz.

Figure 4.15: Manifest of fluid-structure interaction: for low frequency (1 kHz) the air flow is governed by the pressure gradient while at the mechanical resonance (16 kHz) the beam generates the air flow.

Mismatch between the input and output admittance

On figure 4.16 we present the input (Y_{11}) and output (Y_{22}) admittance of the system. The traces are initially even, however the output admittance tends to be higher than the input admittance starting from 1 kHz. Such behavior is motivated by the asymmetry of the acoustical system (two inlets/three outlets). The dimensions of the inlets and outlets are the same however the overall volume of the inlets is lower than the overall volume of the outlets.

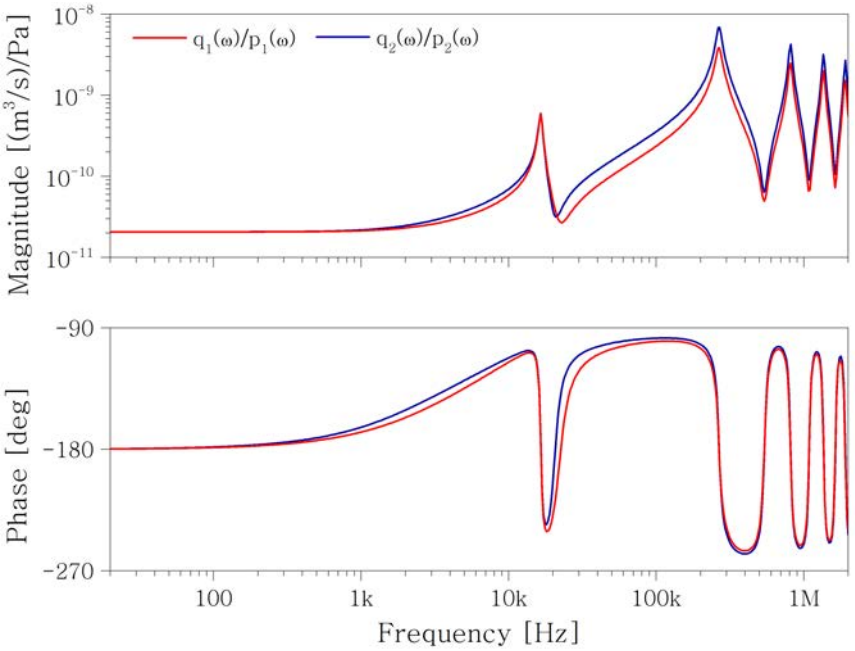

Figure 4.16: Comparison of input and output admittance of MEMS chip.

If we inquire further the asymmetry of the acoustic system we may recognize that the beams located in the center of the MEMS ($S_{tr}(2)$, $S_{tr}(3)$ on fig. 4.3) are subject to the lower acoustic compliance than the beams at the periphery of the MEMS ($S_{tr}(1)$, $S_{tr}(4)$). This problem was not investigated more precisely throughout this thesis however one can expect that the phase of the center beams will be shifted regarding the external beams.

4.3.3 Influence of MEMS chip-scale packaging on the microphone response

To calculate the frequency response of the microphone, we must obviously take into account the volume called the backvolume (obtained by deducting the volumes of the MEMS and the ASIC chips from the internal volume of a package). The backvolume (V_{ar}) introduces acoustic compliance C_{ar}:

$$C_{ar} = \frac{V_{ar}}{\gamma P_0}, \tag{4.2}$$

where γ denotes ratio of specific heats for air and P_0 is the static pressure. Regarding the closed cavity of a package with dimensions larger than thermal and viscous boundary

layers we can use the law of mass conservation:

$$\int_{V_{ar}} \frac{\mathrm{d}V}{\gamma P_0} \frac{\partial p_{ar}}{\partial t} = \int_{V_{ar}} -\nabla \cdot \mathbf{v}\, \mathrm{d}V, \tag{4.3}$$

where p_{ar} is a pressure in backvolume and it equals p_2. By solving the integrals from equation 4.3 we obtain the time derivative of pressure inside the backvolume that can be implemented in FEM as an ordinary differential equation:

$$\frac{\partial p_{ar}}{\partial t} = \frac{q_{ar}}{C_{ar}}, \tag{4.4}$$

where q_{ar} is a total volumetric flow entering the backvolume and it equals q_2.

Comparison of input admittance of the MEMS with and without the package (fig. 4.17) reveals the dissimilarities for the low frequencies. At first sight it is diffi-

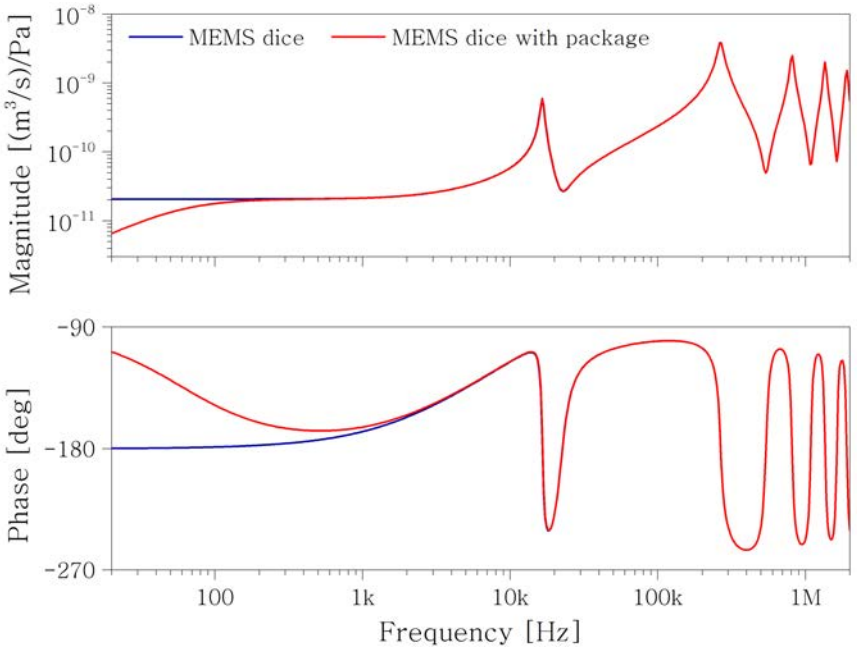

Figure 4.17: Comparison of input admittance of MEMS chip (infinite backvolume) and packaged MEMS (backvolume limited by the package).

cult to explain intuitively the elevated input flow for low frequencies in case of packaged MEMS. To understand this phenomenon we investigated the response of the system in time - more precisely the time that is required for equilibration of the pressure p_1 and the pressure inside the package p_{ar}. Figure 4.18 shows that if we impose the pressure of 1 Pa at the input of the microphone, it takes around 20 ms for the pressure inside the backvolume to equalize. This characteristic time - τ_{RC} - is set by the viscous resistance of the MEMS and the acoustic compliance of the backvolume.

Let us now examine the response to the harmonic input signal p_1 applied at three different frequencies: at the frequency of 60.42 Hz that corresponds to the characteristic time and at the frequencies that are in range of one decade (fig. 4.19). The signal at the frequency 6 Hz corresponds to the period of 167 ms. It is longer period than the characteristic time τ_{RC} of MEMS, therefore the pressure inside the backvolume manages to equilibrate to the input pressure and the pressure gradient across the microbeam

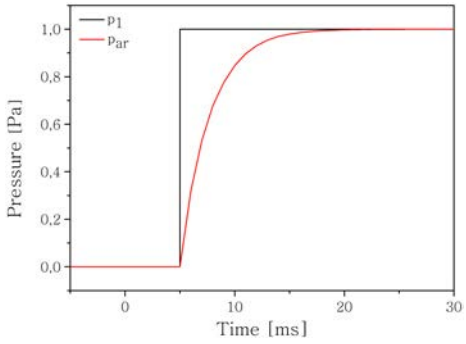

Figure 4.18: Temporal response to the static pressure of 1 Pa imposed at the input.

$(p_1 - p_{ar})$ is negligible. For the frequency of 60.42 Hz we see that the signal p_{ar} decreased, and at the frequency of 600 Hz the gradient of pressure across the microbeam equals p_1. This considerations underline the role of the backvolume and the viscous resistance. At the frequencies with period lower than the characteristic time τ_{RC} the gradient across the beams is to low to obtain the reliable response of the microphone.

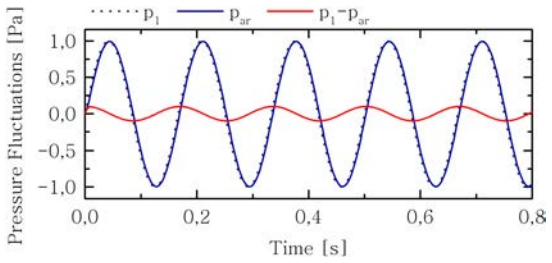

(a) f = 6 Hz.

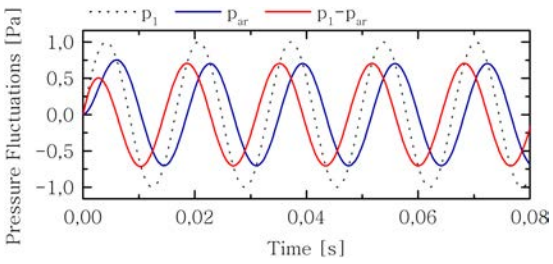

(b) f = 60.42 Hz.

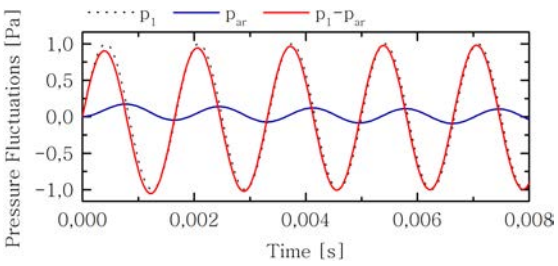

(c) f = 600 Hz.

Figure 4.19: Temporal response to the harmonic pressure imposed at the input.

4.4 Detailed discussion on the mechanical system

4.4.1 Analytical model

Mechanical properties

Mechanical governing equation of the system with inertia J, damping D_V, stiffness C and the torque generated by the acoustic pressure Γ_A is presented in the following manner:

$$J\ddot{\theta} + D_V\dot{\theta} + C\theta = \Gamma_A. \tag{4.5}$$

The damping D_V of the system and the torque Γ_A are the consequence of fluid-structure interaction and are governed by the viscous effects (section 4.3). Inertia of the beam is denoted by its mass and its length:

$$J = m_b\frac{L^2}{3}. \tag{4.6}$$

For the analytical considerations we assume that the beam is rigid and that the total stiffness of the system assembles the rotational stiffness of the hinge C_h and the longitudinal stiffness of the nanogauge K_g:

$$C = C_h + dK_g d. \tag{4.7}$$

The rotational stiffness of the hinge has been calculated by parallel connection of two hinge members. The Young modulus (E_h) of the hinge members that are rotated by 30 degrees relative to <110> crystallographic direction is approximately 140 GPa.

$$C_h = 2\left(E_h\frac{h\cdot cd_h^3}{3l_h}\right). \tag{4.8}$$

Formula for longitudinal stiffness of the gauge uses the Silicon Young modulus in <110> direction ($E_{<110>} = 169$ GPa) and the dimensions of the gauge:

$$K_g = E_{<110>}\frac{s_g}{l_g}, \tag{4.9}$$

where s_g is the cross sectional surface of the gauge ($s_g = w_g h_g$).
Knowing the inertia of the beam and the total stiffness of the system we may evaluate the in-plane resonance:

$$f_0 = \frac{1}{2\pi}\sqrt{\frac{C_h + dK_g d}{J}}. \tag{4.10}$$

For the dimensions given in table 4.2 the resonant frequency calculated from the analytical formula is 16 kHz bor both - the simple and the truss-structured beam.

Discussion on mechanical resonance

The above analysis assumed that the beam is totally rigid. In fact the beam will be subjected to small scale deformations proportional to its overall stiffness.
Analytical designation of mechanical resonance frequency becomes in this case problematic. We may presume that the exact value of the resonance frequency is a combination of two extreme behaviors:

- the beam is rigid, it is free to move at one extremity and suspended by the microhinge and the nanogauge at the second extremity,
- the beam is non-rigid, it is deprived of microhinge and nanogauge - its behavior resembles the case of clamped-free beam.

For now we accept the introduced error, however to provide the final specification we endorse the resonance frequency designated by FEA (subsection 4.4.2), since it is a much more reliable method in this circumstances.

Mechanical transfer function

Mechanical transmissibility of M&NEMS microphone is expressed by the value of longitudinal stress in a nanogauge σ_g generated by pressure difference Δp. We propose to start by calculating the quasi-static value of longitudinal stress as a function of rotation of a beam expressed by θ:

$$\theta = \frac{L}{2}\frac{S_d^* \Delta p}{C_h + dK_g d}, \tag{4.11}$$

where S_d^* denotes the lateral surface of the beam S_d that is modified due to the viscous effects governed by the 2D finite element model. Later we express the quasi-static value of longitudinal stress:

$$\sigma_g = \left[\frac{K_g d}{s_g}\right]\theta. \tag{4.12}$$

In order to introduce the inertial effects we consider fluctuation of pressure at angular frequency ω and mechanical resonance of a beam at ω_0. Knowing that the beam is an oscillator with quality factor Q_V given by viscous shear damping D_V, the mechanical transfer function becomes:

$$T_M(\omega) = \frac{\sigma_g}{\Delta p} = \left[\frac{S_d^*}{S_g}\right]\left[\frac{L/2}{d}\right]\frac{dK_g d}{C_h + dK_g d}\left[\frac{1}{1 - \left(\frac{\omega}{\omega_0}\right)^2 + \frac{1}{Q_V}\left(j\frac{\omega}{\omega_0}\right)}\right]. \tag{4.13}$$

Mechanical system optimization

Thanks to the mechanical transfer function expression (equation 4.13), we may reveal the procedure to enhance the "mechanical sensitivity". Microphone based on M&NEMS technology profits of two mechanical amplification mechanisms. First amplification mechanism comes from the ratio between the modified lateral surface of a beam S_d^* and section of a nanowire S_g while the second comes from the ratio of the lever arm $(L/2d)$.
Enhancement of mechanical sensitivity with use of these factors seems to be straightforward, however the design has to follow the microfabrication restrictions (resolution of lithography, aspect ratio of DRIE, internal stress).

If we continue the study of mechanical transfer, we may see that the stress exerted on the section of the nanogauge is related to the distance between the center of rotation and the center of the nanogauge d. We may simply trace the stress as a function of d with use of analytical expression and numerical model (illustrated on fig. 4.20).
Optimal value of d may be also obtained by analysis of equation 4.13. We first isolate the part of mechanical transfer function that depends on d:

$$f^*(d) = \left[\frac{L/2}{d}\right]\frac{dK_g d}{C_h + dK_g d}. \tag{4.14}$$

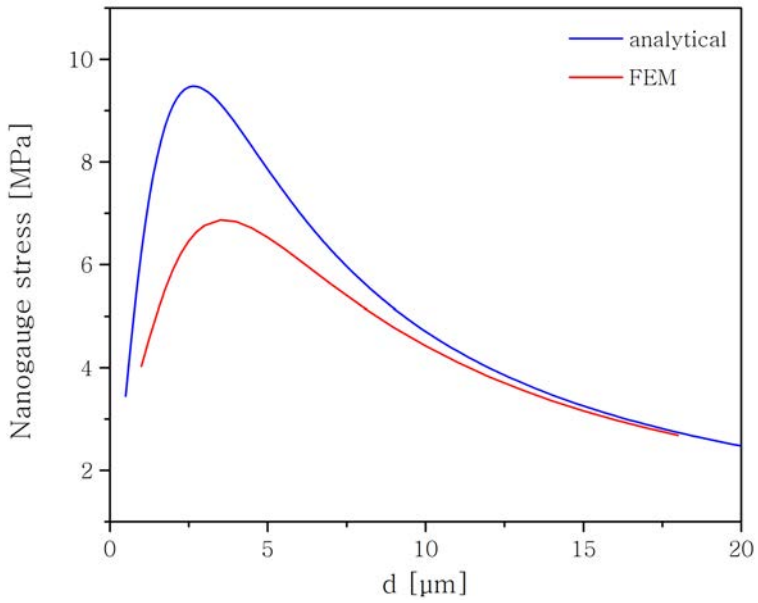

Figure 4.20: Optimal value of d parameter.

We know that the maximum of f^* may be found when $\partial f^*/\partial d = 0$. It give us optimal distance of d defined as:

$$d^* = \sqrt{C_h/K_g}. \tag{4.15}$$

To illustrate how the error in position of the gauge d influence the overall mechanical transfer function we introduce d^* into the equation 4.13:

$$T_M^*(\omega) = \frac{\sigma_g}{\Delta p} = \frac{1}{2}\left[\frac{S_d^*}{S_g}\right]\left[\frac{L/2}{d^*}\right]\left[\frac{1}{1-\left(\frac{\omega}{\omega_0}\right)^2 + \frac{1}{Q_V}\left(j\frac{\omega}{\omega_0}\right)}\right], \tag{4.16}$$

knowing that $C_h/K_g = (d^*)^2$, the ratio T_M/T_M^* can be presented in the following form:

$$\frac{T_M}{T_M^*} = \frac{2\,(d/d^*)}{1+(d/d^*)^2}. \tag{4.17}$$

Relation of T_M and T_M^* from equation 4.17 can be traced as a function of d/d^*. The resulting graph (fig. 4.21) reveals that the misalignment of d introduced either in design process or during the fabrication may reduce the mechanical sensitivity of MEMS. It is important to notice that the horizontal axis is presented in logarithmic scale, therefore the performance drops more drastically if d is lower than its optimal value d^* ($d < d^*$) rather than in the opposite direction ($d > d^*$).

4.4.2 FEM model

3D Comsol model has been prepared in order to analyze the dynamic properties of the microbeams. The model use single-crystal Silicon. The Young modulus for the used material is gathered in elasticity matrix. Microbeam is aligned according to the crystallographic direction of the wafers used in microfabrication of MEMS.
Microbeam is damped resonator with the viscous damping that is introduced by shear

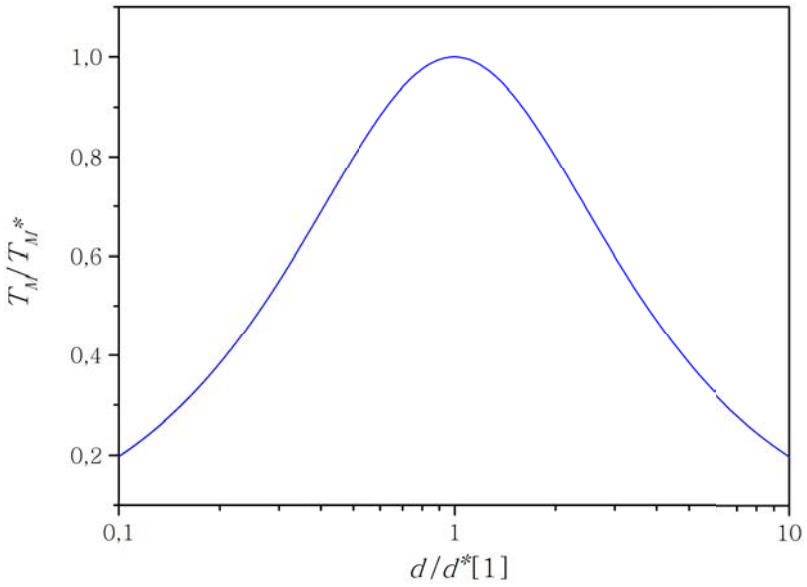

Figure 4.21: Influence of nanogauge misalignment on the resultant mechanical transfer.

stress generated inside the gaps below and above the beam. This damping has been brought into the model by use of Rayleigh damping hypothesis[1]:

$$[D_{V_{FEM}}] = \alpha\,[M] + \beta\,[K]\,, \tag{4.18}$$

We have considered that the damping is proportional to mass matrix, thus $\beta = 0$ while α equals:

$$\alpha = \frac{\mu}{\rho_{Si}} \left[\frac{1}{h}\right] \left[\frac{1}{a} + \frac{1}{b}\right], \tag{4.19}$$

where μ and ρ_{Si} are the air shear viscosity and the Silicon volumetric mass density respectively.

Geometry and mesh

Geometry of the hinge and the beam is build with use of the work plane that is subsequently extruded to the desirable thickness. The hinge and the nanogauge handle elements are created as a polygons while the beam is a rectangle. Finally the union of the foregoing elements with no internal boundaries is generated and the work plane is extruded. The nanogauge is attached to the resulting beam geometry as a 3D block. Specific construction of the long beam together with the nanogauge and the microhinge results in the high scale factors. Regarding the scale factors:

- $h/l_{\text{eq}} \approx 3$,
- $h/h_{\text{g}} = 40$,

different sizes of the mesh elements have to be employed. Therefore we identify four geometry elements which needs different meshing strategies:

[1]Rayleigh damping use an assumption that the damping matrix is proportional to the mass and the stiffness matrices. Therefore it introduces the damping to the system with use of mass and stiffness matrices multiplied by coefficients α and β. [69, 70]

- microhinge where the maximal element size is $cd_h/2$,
- nanogauge handle where the maximal element size is $2cd_m$ and the mesh is refined along the edges to the size $cd_h/6$,
- nanogauge where the maximal element size is $w_g/2$,
- the beam where the maximal element size is $l_{eq}/3$.

The resulting mesh is illustrated on figures 4.22 and 4.23.

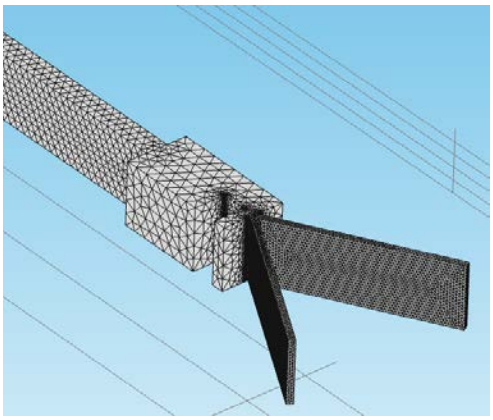

Figure 4.22: Tetrahedral mesh used in simple beam for mechanical studies.

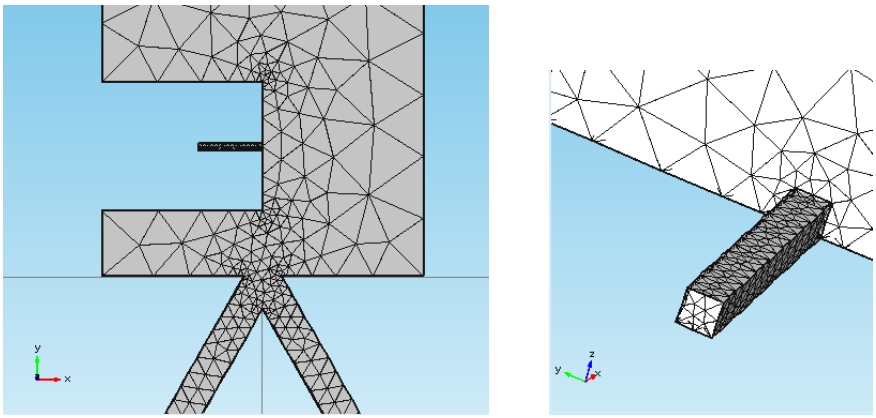

Figure 4.23: Tetrahedral mesh used for discretization of the hinge and the nanogauge.

Eigenvalue analysis

Eigenvalue analysis were used to determine in-plane mechanical resonance of the beam, furthermore this analysis may be used to extract the modal damping of the beam used to estimation of the Brownian noise (see subsection 4.8.1). Unfortunately the in-plane resonance occurs at the frequency much lower than the 16 kHz approximated with analytical formula in subsection 4.4.1. The shape of this resonant mode which occurs at 7.7 kHz is shown on fig. 4.24.

Under such circumstances we have decided to build the beam with use of truss structure (see fig. 4.6) which is commonly used in structural mechanics. The truss-structured

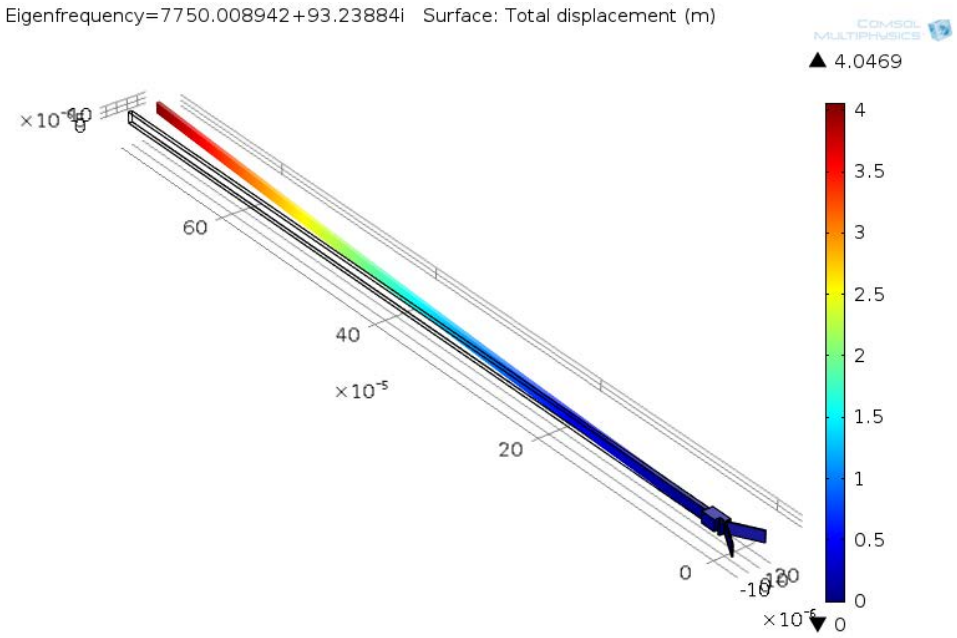

Figure 4.24: First mechanical resonance.

beam is build in such manner that it preserves the same mass as the simple beam. However its stiffness is higher since the truss members are subjected to tensile and compressive forces rather than bending. The 3D model of the beam is prepared with the same procedure as the simple beam and the truss is build as an array of the truss members. The mesh of the truss (fig. 4.25) is prepared individually considering the aspect ratio between the width of the members and the height of the beam ($h/cd_{\mathrm{m}} = h/cd_{\mathrm{h}} = 10$).

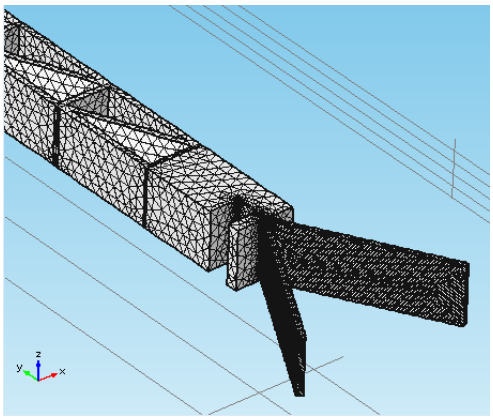

Figure 4.25: Tetrahedral mesh used in truss-structured beam for mechanical studies.

The results of the simulations (fig. 4.26) confirm that the beam based on truss structure represents higher stiffness than the simple beam (in-plane resonance occurs at 12.8 kHz which is much higher than 7.7 kHz given by simple beam). Therefore for the further design considerations we will use the truss beam.

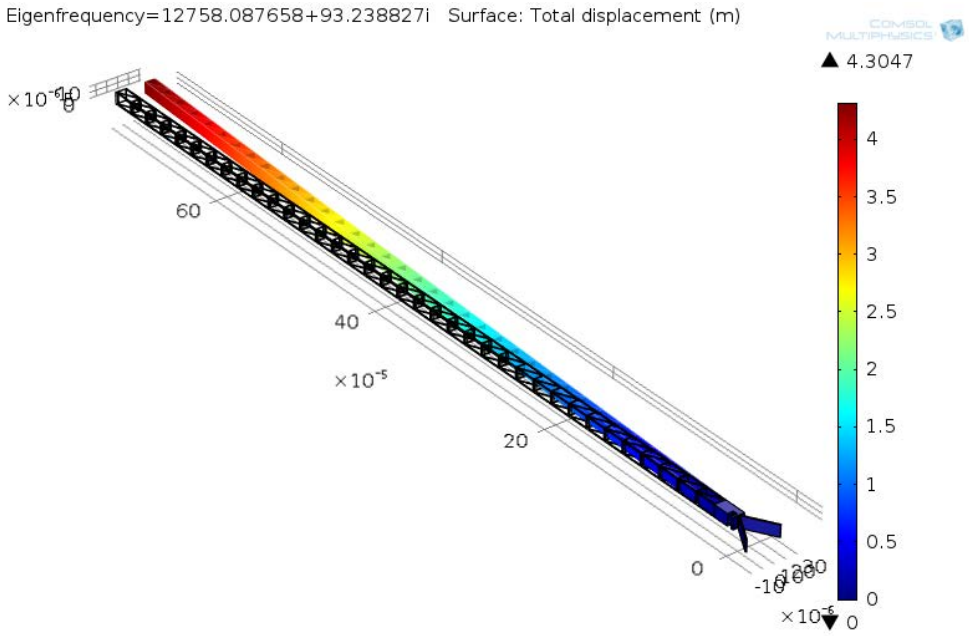

Figure 4.26: First mechanical resonance.

Frequency domain analysis

Frequency domain analysis were used for sensitivity value extraction. Sensitivity for FEM model has been evaluated basing on the average longitudinal stress generated inside the nanogauge by the reference pressure of 1 Pa. The average longitudinal stress was then introduced to the equation 2.16 to obtain the resulting resistance variation. The final sensitivity value was obtained from the electrical transfer function for the full Wheatstone bridge architecture (eq. 2.19). The simulations results are shown and compared to analytical sensitivity in section 4.7.

4.5 Truss structured beam - from 3D to 2D simulations

On the contrary to the simple beam (fig. 4.5) where the cross-section is constant across the beam length, the truss beam is much more sophisticated and there is no straightforward 2D representation of its geometry. Since we have preserved the mass of the beam, the adjustment of resonant frequency coming from equation 4.10 is not required, however we face the acoustic problem which is the adjustment of viscous resistance introduced by the gaps above and below the beam. To investigate this problem we have prepared three models with different geometries of beam cross-sections:

first: truss is represented with rectangle where the width corresponds to the equivalent width of truss members which in fact equals l_{eq} (fig. 4.27),

second: truss is represented with rectangle where the width equals the overall with of truss beam l (fig. 4.28),

third: we represent the beam with three rectangles: two external where width equals the width of truss members (cd_m) and the central one which is slightly wider (1.2 µm) to take into account the angle of the central member of the truss (fig. 4.29).

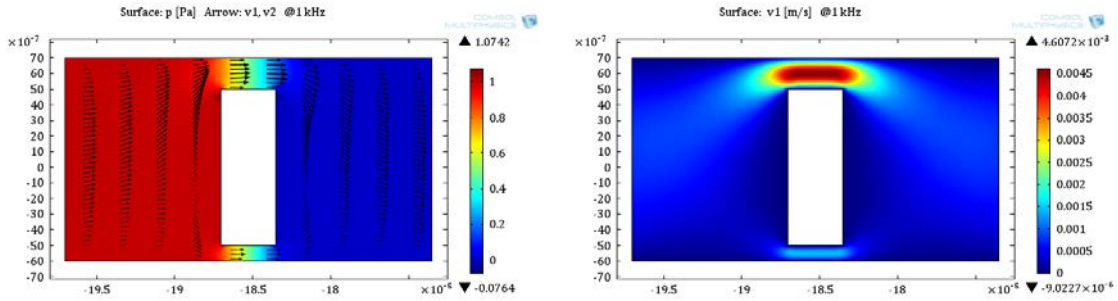

Figure 4.27: Truss beam represented with use the equivalent width.

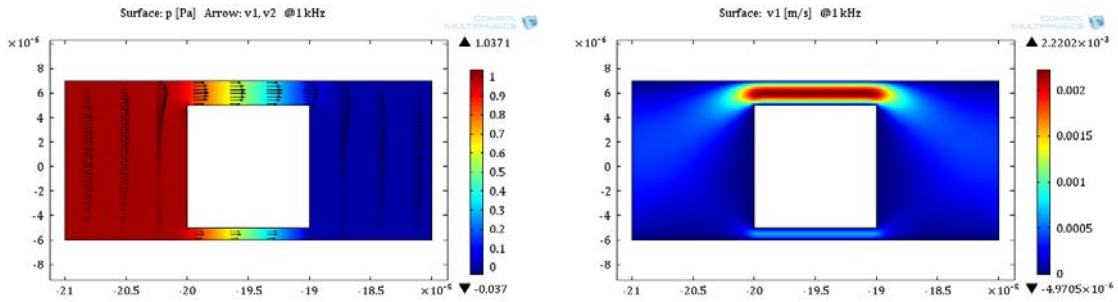

Figure 4.28: Truss beam represented with use the overall width.

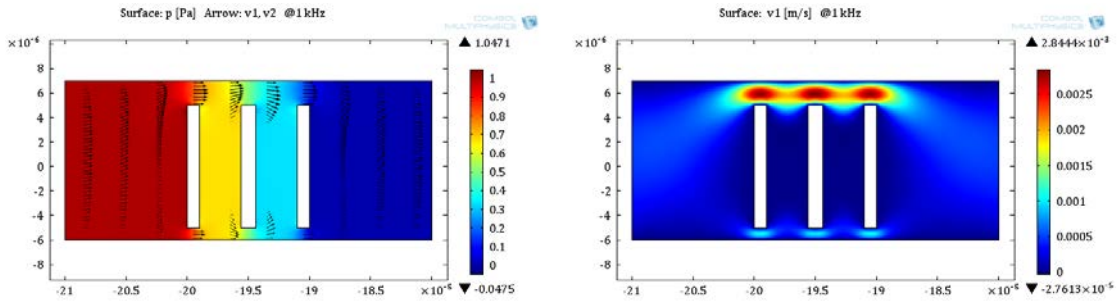

Figure 4.29: Truss beam represented with use of 2D "truss".

The aim of these models is to investigate only the acoustic properties, therefore to simplify the model: we omit fluid-structure interaction and the beams outlines are simulated as the isothermal walls. Moreover in order to save the computation cost we model just one coupler, where the pressure at the inlet and outlet is set to 1 and 0 Pa. The resulting pressure and velocity fields for 1 kHz presented of figures 4.27 - 4.29 are insufficient to compare the 2D modeling approaches and appoint the most precise representation of 3D structure. Therefore to validate our choice we have prepared 3D model where the 3D beam geometry was subtracted from the coupler geometry (no fluid-structure interaction). Even the 3D model of the coupler (without the fluid-structure interaction) that was used to extract the results showed on figure 4.30 is extremely expensive in terms of computation. To visualize the problematic of 3D simulations: properly meshed model that use COMSOL Thermoacoustic module takes 6 minutes to solve one frequency using 10 CPU's. During that time it solves the problem for over 5 millions DOF while using 100 GB of RAM. This extreme computation cost makes 3D model inefficient for engineering problem which is the design of MEMS microphone where the numerous geometry parameters have to be revised.

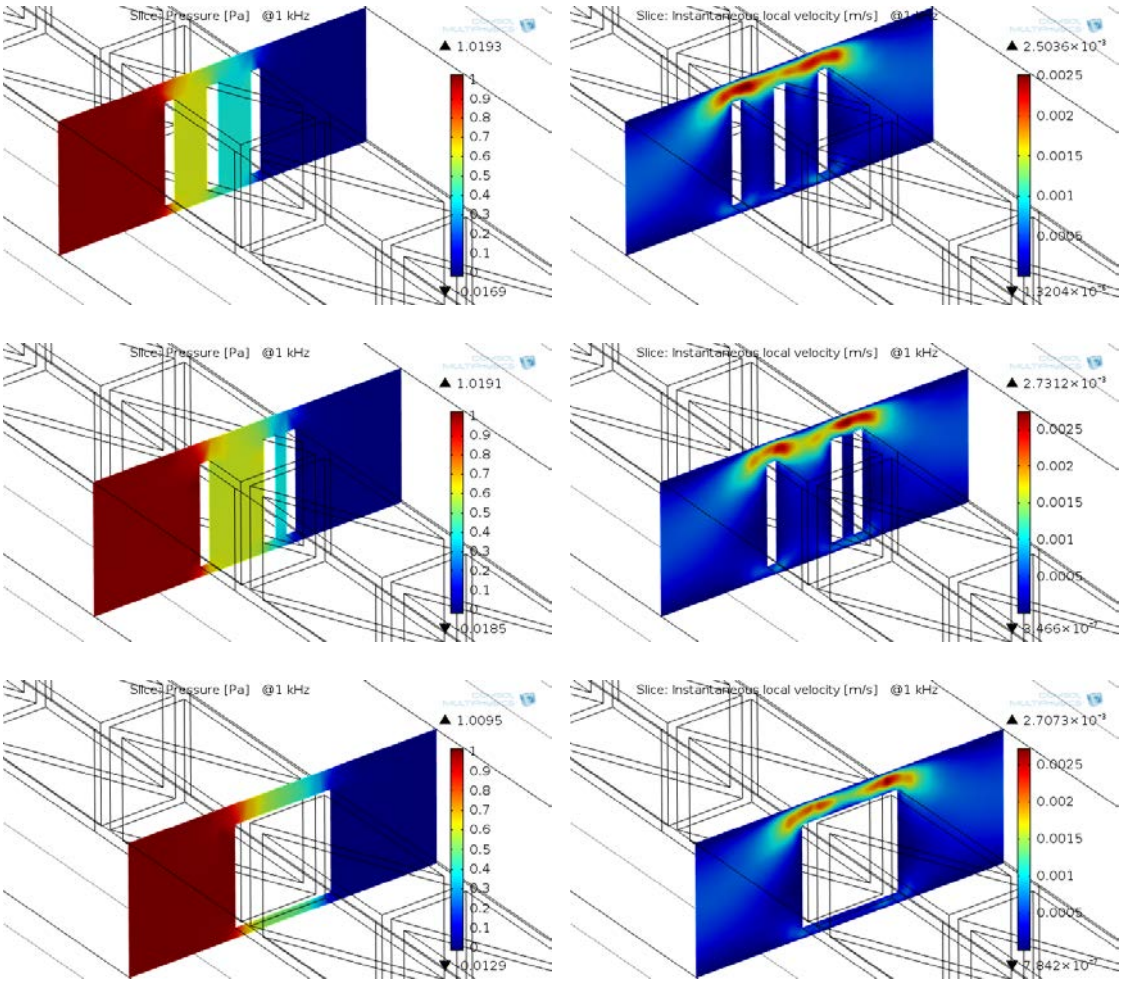

Figure 4.30: Pressure and velocity field distribution in 3D truss beam.

The quantitative comparison of beam representation was made basing on the input admittance for the audible bandwidth (fig. 4.31). We may determine two extreme cases:

geometry with equivalent width that has the lowest viscous resistance and the geometry with overall width that has the highest viscous resistance. We lean towards the interme-

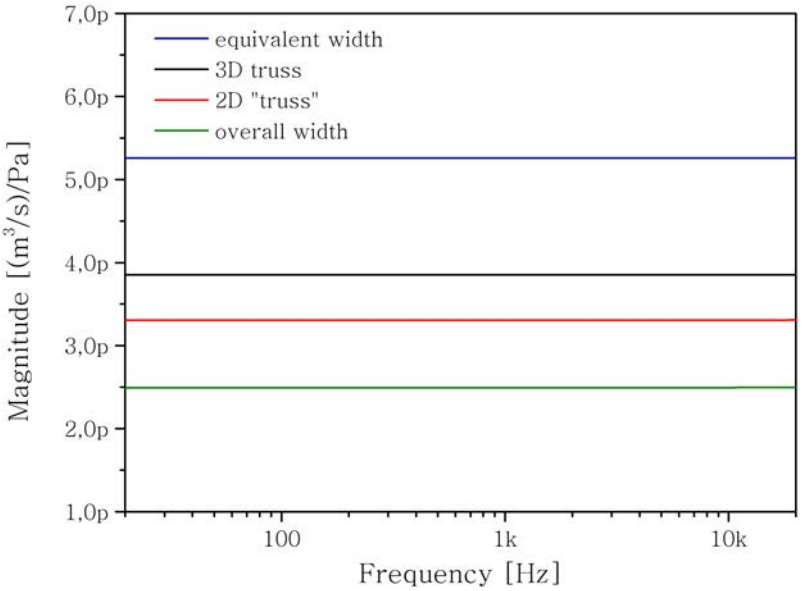

Figure 4.31: Comparison of input admittance for different 2D representations of truss beam.

diary solution which is the 2D "truss". This 2D representation slightly underestimates the input admittance of coupler with truss beam. This underestimation of the input admittance will generate a proportional error in estimation of the frequency response of the microphone (sensitivity - section 4.7). We accept this error and in the further design procedure we use the 2D model with the beam represented as the 2D "truss". However to estimate the error introduced by the 2D representation we have prepared the fully-coupled 3D model in which we have limited the microphone geometry to one coupler and the beam. We have set the gradient of pressure across the coupler to 1 Pa at the frequency of 1 kHz (fig. 4.32(a)). The estimation of the average stress generated inside the nanogauge (fig. 4.32(b)) lead us to the value of the sensitivity which is compared to the one obtained with 2D model in section 4.7.

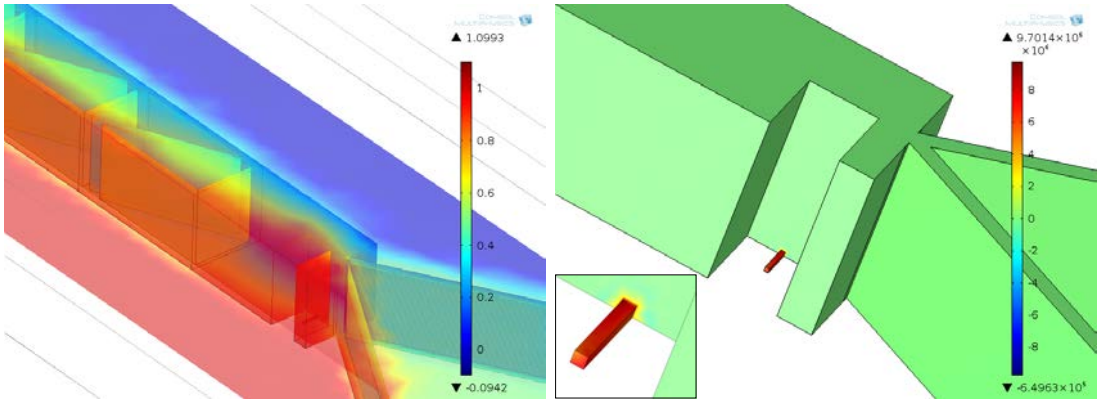

(a) Pressure field distribution. (b) Stress accumulation inside the nanogauge.

Figure 4.32: 3D model of one coupler and the beam with fluid-structure interaction.

4.6 Electrical system transfer function

MADNEMS microphone consists of 4 active gauges, thus the resulting ΔV is proportional to the longitudinal stress in the nanogauge in the following manner (as presented in subsection 2.2.2):

$$\Delta V = V_b \left(\frac{\Delta R}{R} \right) = V_b \pi_{pzr} \sigma_g \tag{4.20}$$

and the electrical transfer function becomes:

$$T_E = \frac{\Delta V}{\sigma_g} = V_b \pi_{pzr}. \tag{4.21}$$

4.7 Sensitivity

Total sensitivity of a microphone is the assembly of its acoustical, mechanical and electrical transfer functions. The sensitivity response (fig. 4.33) given in this section is designated with use of three different models:

- 2D FEM model,
- simplified 3D FEM model,
- Lumped Element Model.

FEM models were already presented while the Lumped Element Model is introduced later in section 4.8. 3D model is not an efficient tool for the design of M&NEMS microphone and the value of the sensitivity has been calculated only for 1 kHz. Two remaining models give nearly similar response for the whole bandwidth. In these models the mechanical behavior of the beam is governed with the same analytical approach, however the acoustic phenomena model differs and it is more precise in the case of the FEM. This difference is visible at low frequency and at the resonant frequency. It is mainly caused by different way of viscous resistance estimation.

For the purpose of sensitivity analysis we have prepared the general equation that describes the sensitivity, however we need to remember that such elements as: S_d^*, Q_V and τ_{RC} are designated in different manner for each model. The components that do not depend on the frequency are gathered and expressed as S_0, the nominal sensitivity of a microphone:

$$S_0 = [\pi_{pzr} V_b] \left[\frac{S_d^*}{S_g} \right] \left[\frac{L/2}{d} \right] \frac{dK_g d}{C_h + dK_g d}. \tag{4.22}$$

Then, to obtain the total sensitivity we add the terms that depends on the frequency:

$$S(\omega) = \frac{\Delta V}{p_1} = S_0 \left[\frac{1}{1 - \left(\frac{\omega}{\omega_0} \right)^2 + \frac{1}{Q_V} \left(j \frac{\omega}{\omega_0} \right)} \right] \left[\frac{\tau_{RC} j\omega}{1 + \tau_{RC} j\omega} \right]. \tag{4.23}$$

Lower limit of a microphone bandwidth is fixed by the inverse of time constant $1/\tau_{RC}$ coming from viscous resistance of the slits and the acoustic compliance of the back volume. High frequency limit is set by the first mechanical resonance frequency of M&NEMS structure.
Nominal sensitivity at $f = 1$ kHz and bias voltage of Wheatstone bridge $V_b = 0.46$ V is estimated with 2D FEM simulations to -56.4 dBV (1.5 mV/Pa). This value is an output voltage of Wheatstone bridge, the final sensitivity of the microphone will be enlarged by amplification of readout electronics (ASIC).

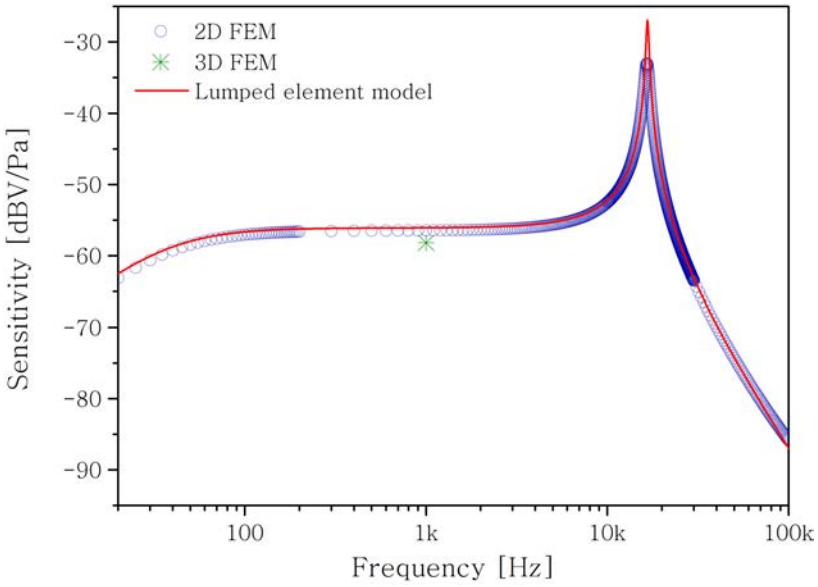

Figure 4.33: Frequency response of the MADNEMS microphone.

Influence of chip-scale packaging

In subsection 4.3.3 the influence of chip-scale packaging on the MEMS microphone response was introduced. We have identified that the major factors are the viscous resistance of the gaps (proportional to the gaps height b) and the acoustic compliance of the backvolume (V_{ar}). Indeed the figures 4.34 and 4.35 shows how easy is to affect the low frequency response of the microphone by varying this two parameters.

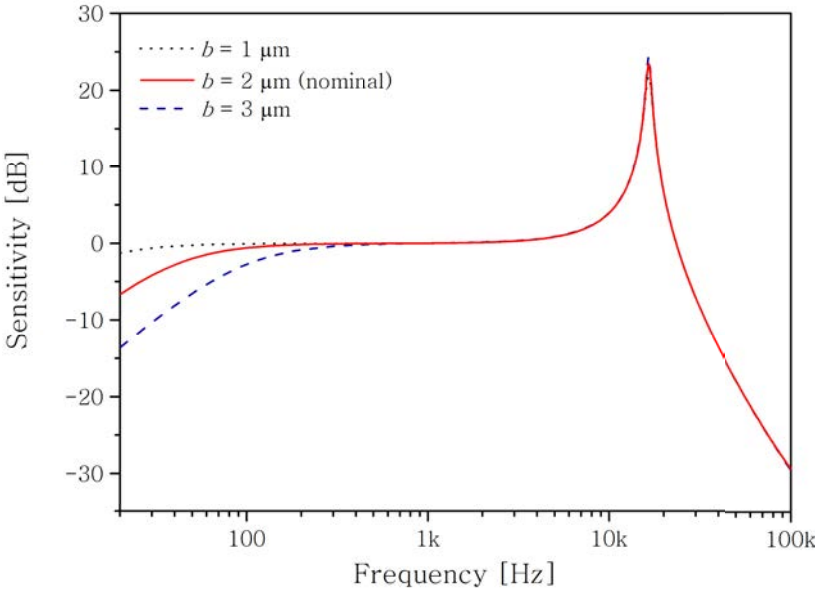

Figure 4.34: Comparison of normalized frequency response $S(\omega)/S_0$ of the microphone for different b parameters.

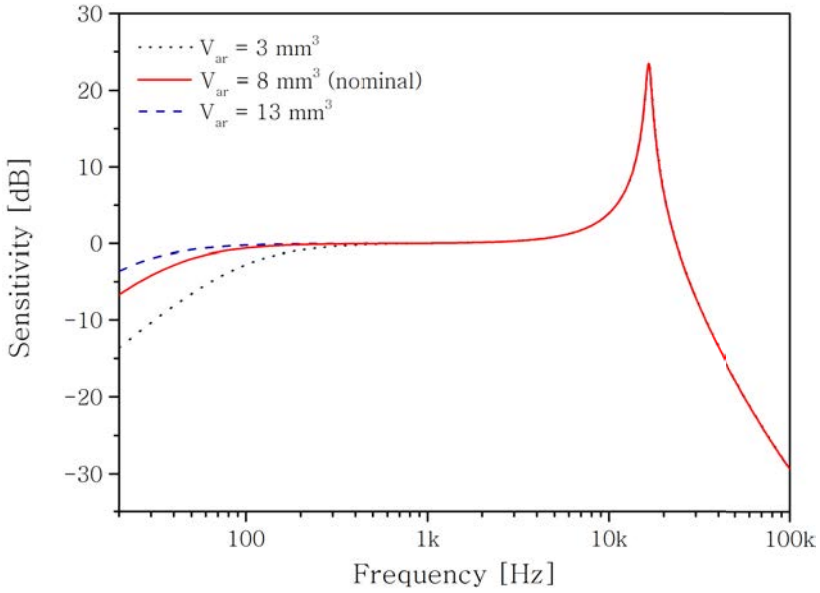

Figure 4.35: Comparison of normalized frequency response $S(\omega)/S_0$ of the microphone for different backvolumes.

4.8 Noise budget

Detection threshold of the sensor is limited by the noises included in the transduction chain. We will now discuss the origins of this noises and their contribution to the noise budget of the microphone. The considerations are based on the comprehensive report of T. Gabrielson [71] which is recommended as an introduction to this section.

4.8.1 Origins of the noises

Depending on the origin, the noises are introduced into the transduction chain in the different manner, they are then subjected to the same conversion mechanisms (for example amplification and filtering) as the functional signal. Therefore the noise budget considerations that are of high importance, are presented in order of the appearance of the noise in the transduction chain (fig. 4.36).
Four main noise sources were identified in the designed microphone:

- thermoacoustic noise which generates the pressure fluctuations as a result of energy dissipation by the viscous resistance of the acoustic system,
- the Brownian noise which induces the force on the MEMS surface similarly to the force generated by the gradient of pressure.
- Johnson noise introduced by the thermal noise of the strain gauge,
- Flicker noise introduced into the strain gauge.

Some of the mentioned noises have mutual origins. These are the thermoacoustic noise, the Brownian noise and the Johnson noise, which are the thermal noises that accompany every dissipative effect (every dissipative mechanism cause the fluctuations). Thermal noises are constant across the spectrum (white noise), we can express them in the following way:

$$F_n = \sqrt{4k_bTR^*}, \tag{4.24}$$

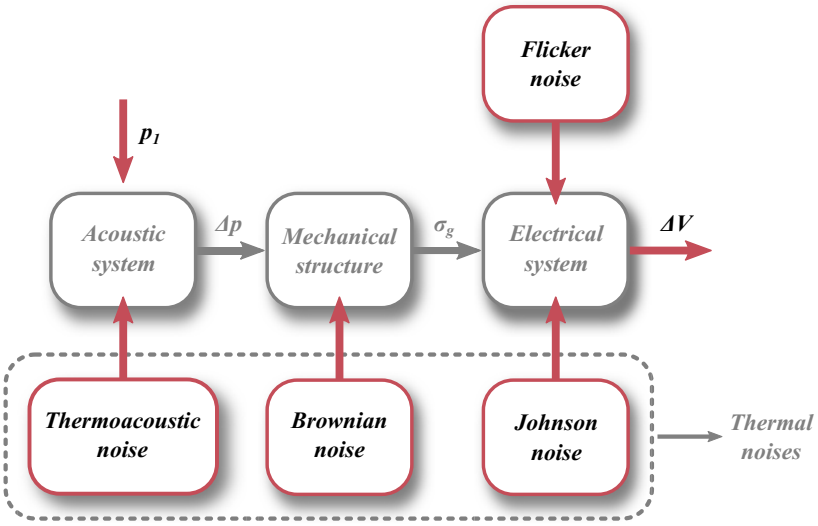

Figure 4.36: Noise model of the microphone.

where k_B denotes the Boltzmann constant, T is temperature in Kelvins and R^* denotes the dissipation mechanism (in case of the microphone it is the viscous resistance of the acoustic system, damping of the mechanical structure and the electric resistance of the nanogauges).

Thermoacoustic noise

This noise is related to the viscous resistance of the acoustic system. Dissipation of acoustic energy inside the MEMS will then generate the pressure fluctuations according to the thermal noise formula:

$$F_{V_n} = \sqrt{4k_bTR_{viscous}}. \tag{4.25}$$

Brownian noise

Mechanical-thermal noise (Brownian noise) is a white noise caused by the Brownian motion of the fluid particles. Those particles randomly interact with the surface of the microsystem causing the beam displacement in the same manner as in the case of sound pressure load. The resulting beam displacement is then transduced into variations of output voltage.
Problematic of the Brownian noise might be omitted at large scale, however not in case of the microsensors. The most comprehensive studies on Mechanical-thermal noise were prepared by T.B. Gabrieson [71, 72]. He have presented the method of Mechanical-thermal noise evaluation basing on the Equipartition Theorem and Nyquist Relation. Spectral density of force generated by mechanical-thermal noise is then:

$$F_{B_n} = \sqrt{4k_bTR_{mech}}, \tag{4.26}$$

k_B denotes the Boltzmann constant, T is temperature in Kelvins and R_{mech} denotes the mechanical resistance (damping).

Analytical model examination. Knowing the viscous shear damping D_V we may estimate the torque Γ_{Bn} exerted on the beam by the Brownian noise. To do so, we

replace mechanical resistance R_{mech} in equation 4.26 by the viscous shear damping:

$$\Gamma_{B_n} = \sqrt{4k_bTD_V}. \tag{4.27}$$

Knowing the torque generated by Mechanical-Thermal noise we may modify and combine equations 4.11 and 4.12 to obtain:

$$\sigma_{g_{B_n}} = \left[\frac{K_g d}{s_g}\right]\left[\frac{\Gamma_{B_n}}{C_h + dK_g d}\right]\left[\frac{1}{1-\left(\frac{\omega}{\omega_0}\right)^2 + \frac{1}{Q_V}\left(j\frac{\omega}{\omega_0}\right)}\right]. \tag{4.28}$$

Finally, the contribution of this noise expressed in $\left[V/\sqrt{Hz}\right]$ over the sensor bandwidth is:

$$V_{B_n} = V_b \pi_{pzr} \sigma_{g_B}. \tag{4.29}$$

FEM examination. Finite element model allow us to estimate the value of damping by use of modal analysis presented in section 4.4.2. It may be extracted from the modal mass μ_j in the following manner:

$$[D_{V_{FEM}}] = \alpha\, {}^t\phi_j\, [M]\, \phi_j = \alpha\, [\mu_j]\,, \tag{4.30}$$

where ϕ_j is a mode shape matrix and μ_j is a modal mass. Knowing the modal damping, we give the Mechanical-Thermal noise as an input noise expressed in $\left[Pa/\sqrt{Hz}\right]$ with the modified formula given by T.B. Gabrielson [72]:

$$B_n = \sqrt{4k_bT\frac{R_{mech}}{(Lh)^2}} = \sqrt{4k_bT\frac{D_{V_{FEM}}}{(Lh)^2}}. \tag{4.31}$$

Flicker noise

Flicker noise is also called Hooge noise or 1/f noise because its spectrum is inversely proportional to the frequency. It is an intrinsic noise of each conductor, it is introduced into the sensor transduction chain at the level of silicon nanogauges.
The origins of this noise are still under study, however they are linked to the fluctuations of conductivity that can be the results of fluctuation of carriers density and fluctuation of their mobility. The behavior of the noise has been empirically described in 1969 by F.N. Hooge [73] and the comprehensive discussion on 1/f noise origins may be found in his more recent work [74]:

$$V_{F_n} = V_b\sqrt{\frac{\alpha_H}{c_n f}}, \tag{4.32}$$

where α_H is called the Hooge parameter and it is a material constant while the c_n denotes the number of carriers inside the resistor. The Hooge parameter depends on the material (quality of the crystal). It can be optimized by following the doping of the Silicon by annealing process.
The number of carriers c_n inside the gauge is calculated with:

$$c_n = l_g s_g N \cdot 10^6, \tag{4.33}$$

where N is an impurity concentration (see table 4.3).

Johnson noise

Johnson noise (Johnson-Nyquist noise) is another intrinsic noise that is related to the nanogauge resistance and contributes to the total noise of the nanogauge. It has a white frequency spectrum and it is represented by the following formulation:

$$V_{J_n} = \sqrt{4k_bTR}. \tag{4.34}$$

4.8.2 Equivalent circuit representation of the microphone for the noise budgeting

Circuit representation and designation of lumped elements

Equivalent circuit representation is a popular technique of MEMS microphones simulations. It has been applied by several authors [19, 26, 29, 32, 33] to model MEMS microphones response and the noise budget. Moreover it seems to be the most convenient method to estimate the output noise generated by the system. For sake of simplicity, we present the lumped elements of the designed microphone on the example of one beam (fig. 4.37).

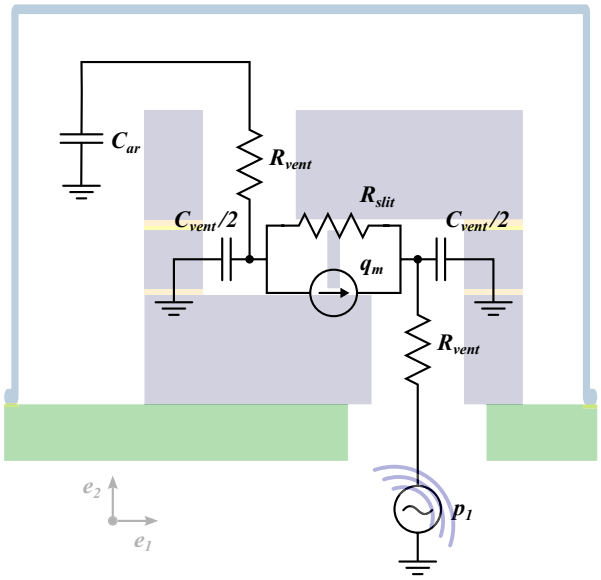

Figure 4.37: Lumped elements of the microphone presented on single coupler.

We may then identify the following elements:

- p_1 is the acoustic pressure at the input of the microphone,
- R_{vent} is the viscous resistance of the inlet and outlet vents,
- C_{vent} is the acoustic compliance of the inlet and outlet vents,
- R_{slit} is the combined viscous resistance of the gaps above and below the beam,
- q_m is the air flow generated by the mechanical structure,
- C_{ar} is the acoustic compliance of the backvolume.

If we want to represent the full architecture of designed microphone, we need to take four beams, two inlet vents and three outlet vents. The equivalent circuit is then presented

on fig. 4.38. The microphone simulations based on such circuit may be done in Spice software or by use of Linear Time-Invariant (LTI) models in MATLAB.

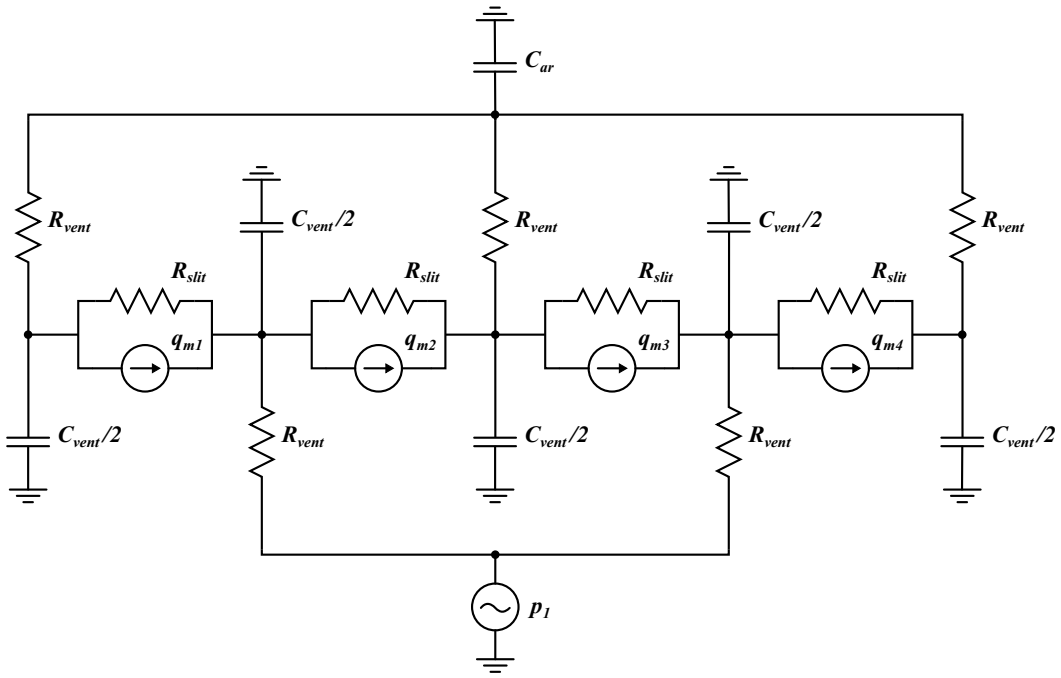

Figure 4.38: Lumped model of the microphone.

Our considerations assume that the air is non compressible in the slits above and below the beams. Moreover for audible bandwidth inertial effects can be neglected. Including viscous shear stress in the air, Navier-Stokes momentum balance equation provides relationship between the pressure p and velocity $\mathbf{v}$ fields [75]:

$$\frac{\partial p}{\partial x} = \mu \frac{\partial^2 \mathbf{v}}{\partial y^2}, \tag{4.35}$$

Equation 4.35 is integrated considering difference of pressure across the coupler Δp and no-slip conditions at fluid-structure interfaces. As a result we obtain formula for volumetric air flow inside the coupler q_c:

$$q_c = \frac{1}{R_{slit}} \Delta p + \frac{L}{2} S_d^* \dot{\theta}, \tag{4.36}$$

where $\dot{\theta}$ is the angular velocity of the beam (see fig. 4.6), R_{slit} denotes the total viscous resistance of gaps that is calculated with LRF model and given later and S_d^* is modified lateral surface of a beam driven by viscous effects:

$$S_d^* = (Lh) \left(1 + \frac{a+b}{2h} \right). \tag{4.37}$$

The second part of equation 4.36 is the air flow generated by the mechanical structure:

$$q_m = \frac{L}{2} S_d^* \dot{\theta}. \tag{4.38}$$

Torque applied to rotating beam is defined by acoustic force reduced by viscous shear damping:

$$\Gamma_A = \frac{L}{2} S_d^* \Delta p - D_V \dot{\theta}, \tag{4.39}$$

where viscous shear damping lumped coefficient D_V is:

$$D_V = \frac{\mu L^2}{3}(lL)\left(\frac{1}{a}+\frac{1}{b}\right). \tag{4.40}$$

The acoustic compliance of the backvolume is calculated with use of the following formula:

$$C_{ar} = \frac{V_{ar}}{\gamma P_0}. \tag{4.41}$$

In this model the values of some elements are designated with use of the LRF model approach described in section 3.6.2. With this approach we have determined the value of R_{slit}, R_{vent} and C_{vent}:

Table 4.4: Lumped elements determined with use of LRF model.

Symbol	Value	Unit
R_{slit}	3.2444e11	$[Pa/(m^3 s)]$
R_{vent}	9.987e7	$[Pa/(m^3 s)]$
C_{vent}	3.59e-19	$[m^3/Pa]$

Introduction of noise sources

Resistors presented on figures 4.38 and 4.37 are the noiseless resistors, in fact both schematic have to be modified to introduce the noises coming from the viscous resistances. For the noise analysis each noiseless resistor is complemented by the voltage noise source as shown on fig. 4.39.

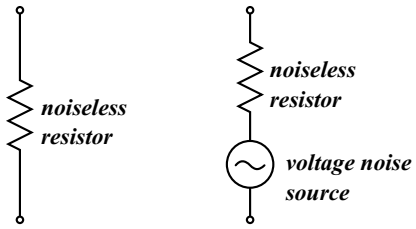

Figure 4.39: Introduction of noise sources.

4.8.3 Total transduction chain noise

Total noise of the microphone corresponds to signal (voltage) level measured at the output of microphone located in a perfectly quiet environment (no pressure fluctuations). Knowing the sensor sensitivity, noise can also be represented as an equivalent pressure noise at the entrance of the microphone. This second form gives an order of magnitude of the signal level detectable by the sensor.

Contributions of noise sources

We present the global view of noise spectral density on the figure 4.40 it reveals the three noises that dominates: the Flicker noise, the Johnson noise and the Brownian noise. Flicker noise (which decreases along with frequency) predominates the total noise of the sensor at low frequencies and it is negligible in the vicinity of the mechanical

resonance of the sensor. Johnson noise dominate the noise budget between 1.3 and 6.5 kHz, then in the vicinity of the mechanical resonance the performance is limited by the mechanical Brownian noise which is amplified mechanically in the same manner as the functional input signal. The thermoacoustic noises are of the smaller importance in the architecture of presented microphones, however the noise of the couplers may disturb the microphone performance as its value is relatively important at low frequencies.

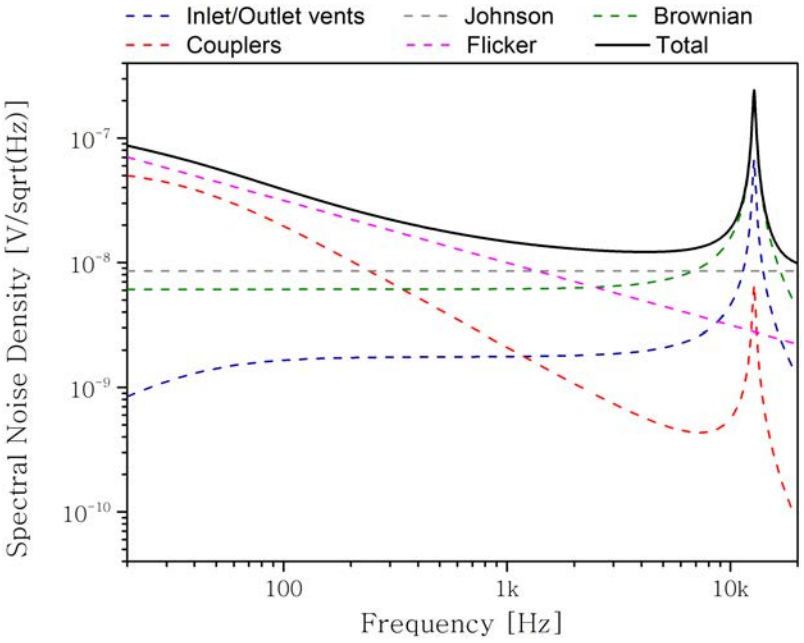

Figure 4.40: Overall contributions of noises.

On figure 4.41 we present once again the importance of the backvolume for the microphone performance. The scale of this figure has been adjusted to the scale of figure 4.40 to facilitate the comparison. To trace this noise contributions we have assumed that the backvolume is infinite. We see that the backvolume has an impact only on the thermoacoustic noises. It is important information for the future optimization of the sensor and shows that in the miniaturization of the sensor, the reduction of backvolume is one of the most challenging limitations.

Noise floor

Typically the noise floor of every sensor is given at the output of the readout electronics. The value of the noise floor is given in V and more common in dBV which is a voltage relative to 1 V. Therefore to obtain the noise floor of the sensor we need to integrate the value of the noises over the bandwidth:

$$V_{tot_n} = \sqrt{\int_{f_{min}}^{f_{max}} V_{V_n}^2 + V_{B_n}^2 + V_{F_n}^2 + V_{J_n}^2 \, \mathrm{d}f}. \tag{4.42}$$

Equivalent input noise (EIN)

The value of EIN provides the information on the detection threshold of the microphone. Namely the signal with magnitude below the EIN will not be detected since it will be

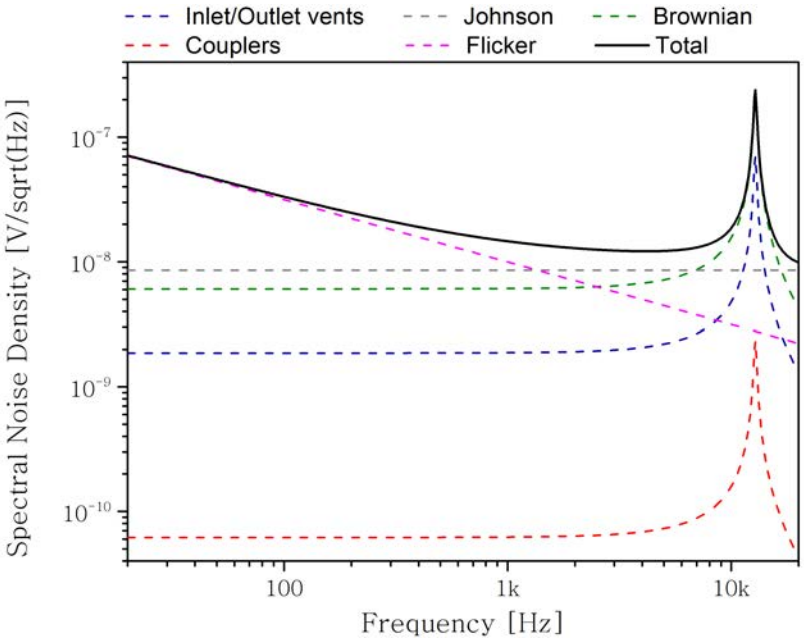

Figure 4.41: Overall contributions of noises under assumption of infinite backvolume.

hidden below the intrinsic noise of the sensor. The equivalent input noise is presented in $\mathrm{dB_{SPL}}$ which is the sound pressure level referenced to the threshold of hearing. In order to obtain EIN, first we obtain its value in Pa:

$$EIN_{Pa} = \frac{\sqrt{\int_{f_{min}}^{f_{max}} V_{V_n}^2 + V_{B_n}^2 + V_{F_n}^2 + V_{J_n}^2 \,\mathrm{d}f}}{S(\omega)}, \tag{4.43}$$

then we convert it to dB_{SPL} by the following formula:

$$EIN = 20 \log_{10} \left(\frac{EIN_{Pa}}{p_{ref}} \right), \tag{4.44}$$

where p_{ref}, the threshold of hearing equals 20 µPa.

4.9 Influence of overetch on the microphone response

MEMS structure is obtained in dry etching process (see section 5.1). The dry etching is a very precise process, however depending on the specification of the geometry and the process parameters the dimensions of final structure slightly vary [76]. This derogation (example of overetch effect is shown on fig. 4.42) is introduced into the transduction chain at the level of acoustic system (overetch of acoustic vents) and at the level of mechanical structure.

Observations of cleaved wafer with SEM suggests the overetch of 9 µm in case of acoustic vents and 125 - 200 nm for the mechanical structure. However this measurements certainly suffer of error and give rough approximation. According to the author experience, the overetch value for micromechanical structure may reach 300 nm and the final value has to be measured by use of built-in structures used for technological process characterization. Overetch of the mechanical structure appears in the shift of

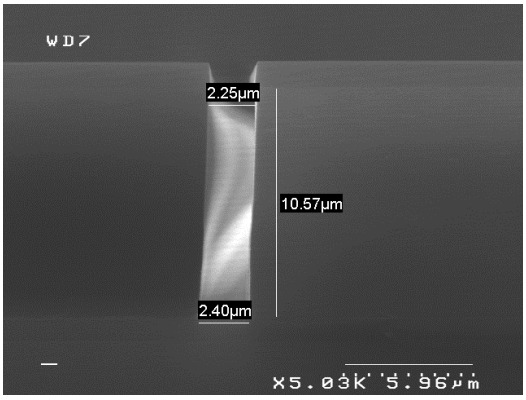

Figure 4.42: Overetch issue in DRIE. The 2 µm intended width varies from 2.25 to 2.40 µm over the thickness of epitaxial layer.

mechanical resonance (MEMS mass will vary) and in critical cases it may affect the integrity of mechanical structure (in case of truss and microhinge the initial sizes goes down to 1 µm).
We have investigated the the consequences of overetch on acoustic transfer function. The results are compared to the nominal sensitivity response on fig. 4.43 and 4.44. Size dispersion of inlets and outlets affects the sensitivity value at the mechanical resonance while the overetch of the truss beam marginally shifts the low cut-off frequency of the microphone (overetched truss beam has lower viscous resistance).

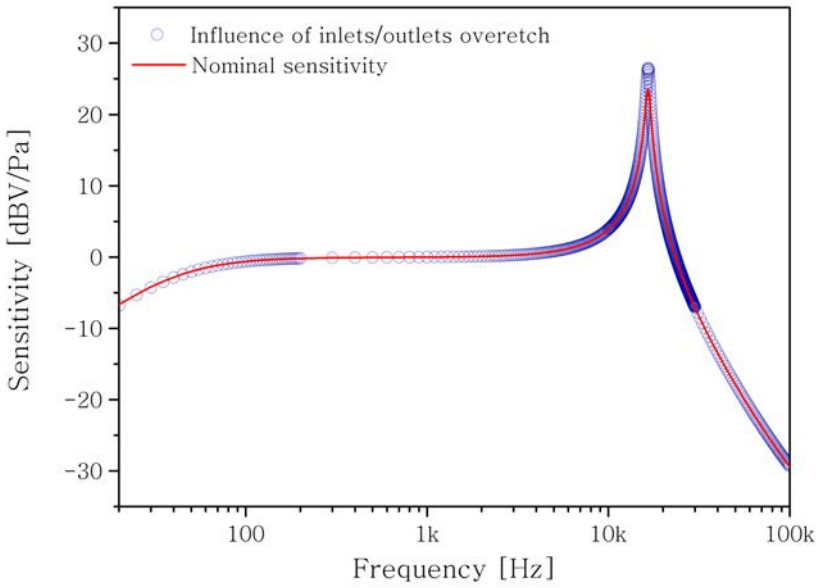

Figure 4.43: Influence of inlets and outlets overetch on the response of the microphone.

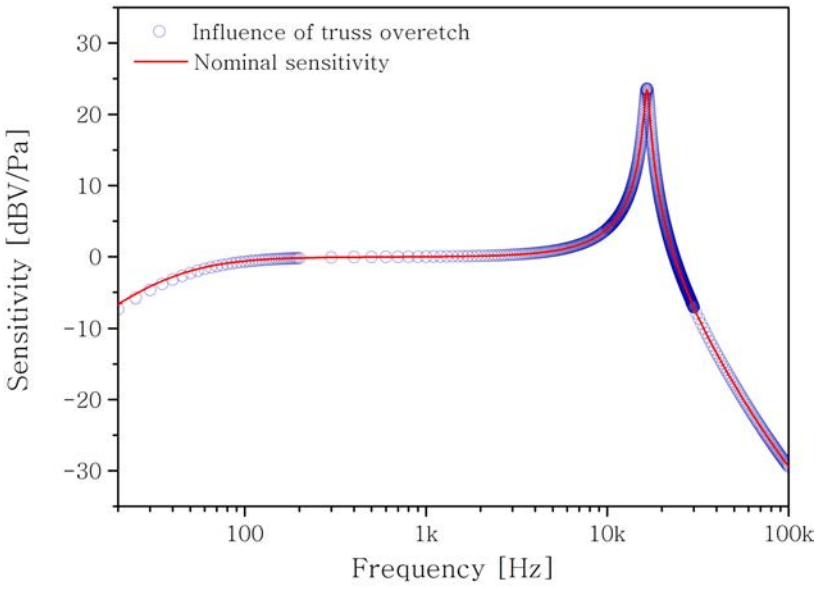

Figure 4.44: Influence of the truss beam overetch on the response of the microphone.

4.10 Tolerance to mechanical shocks and sound pressure overload

Mechanical shock

MEMS microphones are most commonly used in portable devices. This type of applications impose the challenging requirements in terms of mechanical shock reliability since the hand held devices frequently suffer of drop impacts. Typical failures in MEMS devices are:

- fracture,
- stiction,
- short-circuit,
- package failure.

Maximum ratings usually consider the acceleration of 10 000 g. MEMS that are already in advanced phase of development are simulated and simultaneously undergoes the drop tests together with their assembly (chip-scale package). Mechanical shock studies [77,78] of commercial MEMS microphones shows the highest fragility (membrane rupture) in Z-axis. It is not surprising for the out-of plane moving membrane.

Our investigations are limited to the fracture inside the MEMS chip. Furthermore we may already assume that the crucial element that suffers the highest stress is the nanogauge. Lets now consider the type of numerical studies that simulates the drop impact. The device is dropped on the hard surface and the generated stress will be studied, thus we need to perform transient studies with acceleration in form of the pulse [79]. We have chosen the half-sine pulse (fig. 4.45) expressed as:

$$G_s(t) = G_{s0} \sin \frac{\pi}{T} t, \tag{4.45}$$

where G_{s0} and T are the peak acceleration and the width of the pulse. The shock is

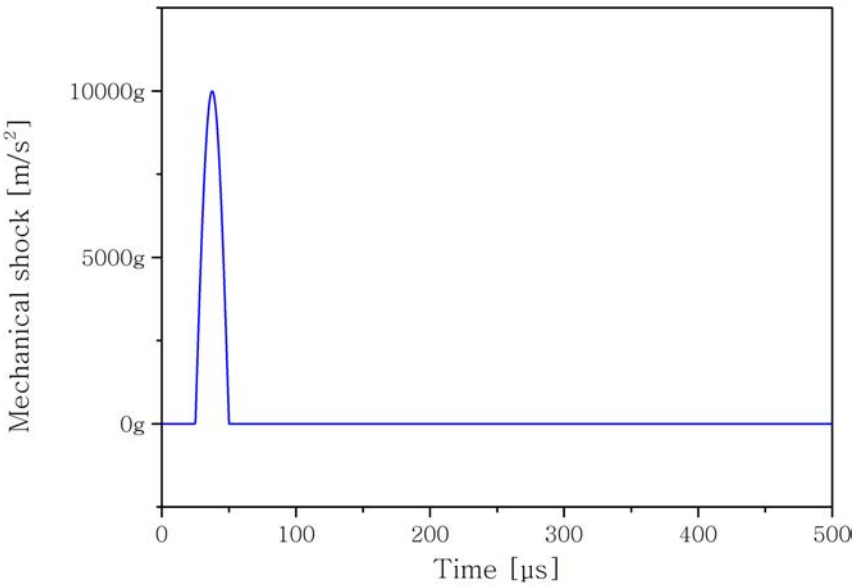

Figure 4.45: Characteristic of the mechanical shock applied to the MEMS.

applied as a body load to the whole mechanical structure sequentially in each spatial direction. The highest stress corresponds to the e_1 direction (fig. 4.46) which is relevant since it is the sensor working orientation. Regarding the fig. 4.46 one might be concerned of the high von Mises stress. In e_1 direction stress spans to nearly 10 GPa while the crystalline Silicon fracture stress adopted by [46] is 2.8 GPa.
If we trace the spatial displacement generated at he beam extremity by the acceleration (fig. 4.47) it oscillates with amplitude of 20 µm in case of e_1 direction and 10 µm in case of e_2 direction. In fact the MEMS has embedded stops that restrain the displacement to 1 µm in case of e_1 and e_3 directions. For the e_2 direction the displacement is restrained by the gaps above (2 µm) and below (1 µm) the beam. Keeping in mind the stops we

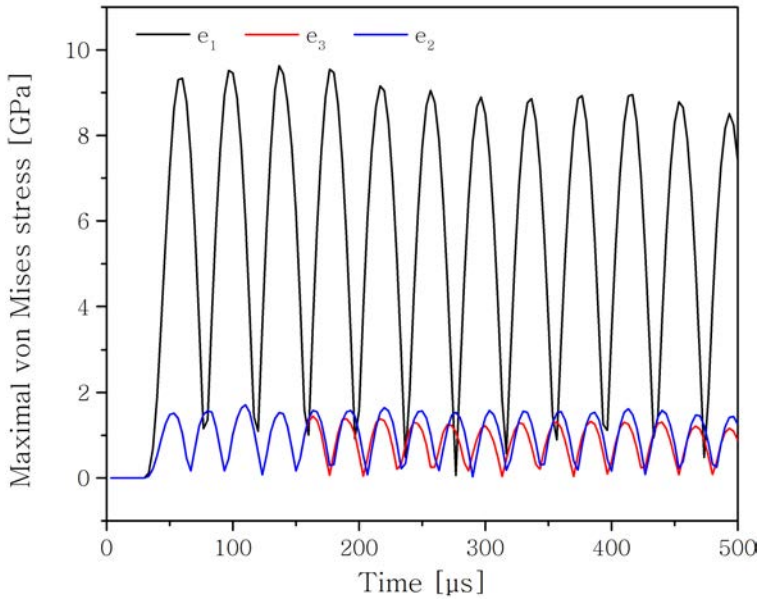

Figure 4.46: Maximal von Mises stress in the nanogauge.

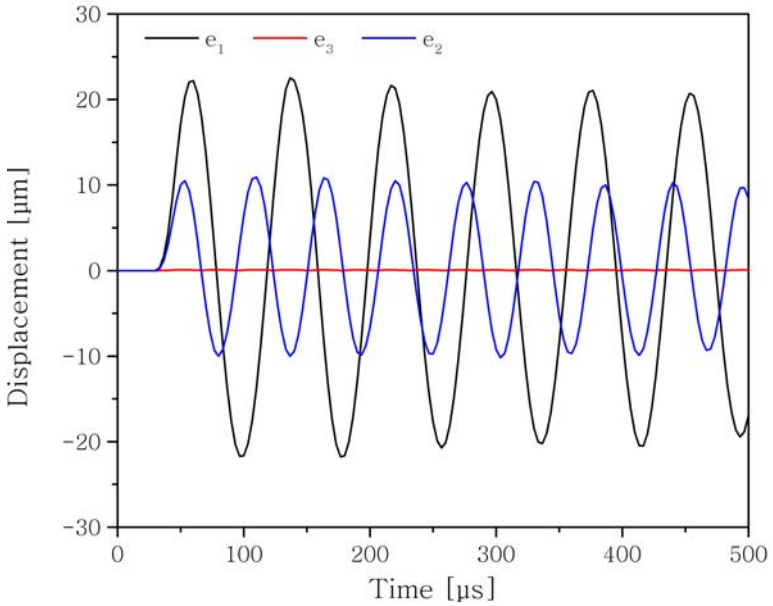

Figure 4.47: Spatial displacements of the beam extremity.

may say that the shock-generated stress in real structure will be largely reduced.

Maximum acoustic input

Maximum acoustic input it is a maximum sound pressure level that can be transduced by the M&NEMS microphone within the linear range. After [46] the maximal stress in the gauge that assures the linear behavior equals 100 MPa. From 100 MPa we can designate the maximum input pressure (Δp_{max}) by combining equations 4.11 and 4.12:

$$\Delta p_{max} = \sigma_{gmax} \left[\frac{s_g}{K_g d}\right] \left[\frac{2}{L}\right] \left[\frac{C_h + dK_g d}{S_d^*}\right]. \tag{4.46}$$

If we express the maximum input pressure in dB, we obtain the maximum acoustic input of 115 dB.

Summary of sensor specifications and discussion

Sensor specifications

In this chapter we have investigated the new architecture of the microphone. Those investigations resulted in the prevision of the sensor specifications that are gathered in table 4.5.

We can not squarely compare this specifications to the commercial products because we give the specifications of the MEMS dice without the ASIC. Normally the ASIC will amplify the output signal and the sensitivity of designed microphone will reach the one given by commercial products (typically -38 dBV). The given SNR is much lower than the best results of the commercial and state of the art sensors. We can accept this value for the prototype, however for the future designs this value has to be optimized. It can be done by splitting the noise sources and investigating the problem in two fields:

Table 4.5: Evaluated specifications of MADNEMS microphone (without signal conditioning).

Parameter	Value		Conditions
Performance			
Sensitivity	-56.4	dBV	1 kHz, 94 dB SPL
Signal-to-Noise Ratio (SNR)	44	dB	
Equivalent Input Noise (EIN)	50	dB SPL	bandwidth 20 Hz - 20 kHz
Frequency response	0.04 to 20	kHz	limited by -3 dB point
Maximum acoustic input	115	dB SPL	limited by the linearity
Power supply			
Supply voltage	0.46	V	supply current 100 μA
Output characteristics			
Maximum output voltage	16.9	mV	115 dB SPL input

Electrical noises consist of the intrinsic noises of the nanogauge - the Flicker noise and the Johnson noise. First of this noises can be decreased by the optimization of technological process and improving the crystal lattice quality. The second one is proportional to the electric resistance.

Acousto-mechanical noises are placed together since both: thermoacoustic noise and Brownian noise depends on the architecture of the acoustic system. We have shown that the viscous effects allow to establish the pressure gradient across the beam and enable the functioning of the microphone. However the same effects introduce the viscous resistance which generates the thermoacoustic and Brownian noise. To decrease these noises we need to optimize the architecture of the acoustic system (cavities in MEMS and the backvolume). This type of noises seems to be even more challenging than the electrical noises since the noises optimization and further miniaturization do not come along.

As for the rest of the specifications, it corresponds to the ones of the commercial products. We have been aware that matching all of the specifications to the commercial products is challenging in terms of the sensor design, however we want our microphone to be competitive. Therefore our design corresponds to the commercial products in such critical aspects as the overall chip-package size and the power consumption.

Tools for design of a MEMS microphone

Another aspect of this chapter was the application of FLNS and Lumped Element model to the sensor design. Both of this models are valuable in the design process. Initial design and especially the dimensioning of the microphone were prepared basing on the FLNS model with fluid-structure interaction. This model is efficient if prepared in 2D and it is essential to understand the acoustic phenomena at the microscale. Afterward we have used the Lumped Element model for the analysis of the noises in the microphone. Moreover the frequency response of the microphone obtained with both of the models shows a good match. Despite the high computational cost we have prepared simplified 3D model to verify if 2D representation of the microphone is correct. The

sensitivity value obtained with 3D model is in slightly lower than the one obtained with approximative models, however it is in the same scale.

These tools have to be validated with the measurements of the fabricated device. Unfortunately the technological problems have postponed the fabrication of the prototype, however the fabrication process has been already optimized and the prototype should be available shortly. Anyway the presented models are proven to be a powerful tools for the MEMS microphone designer.

Chapter 5

Technological implementation

Basic M&NEMS process flow is presented at the end of chapter 2. This basic process flow has been adapted to fulfill the requirements of the designed microphone architecture and it is presented in the first section of this chapter. Afterward we discuss the MEMS microphone packaging approaches based on the commercial products review to finally propose our in-house solution. Due to the problems that have been encountered, the MEMS fabrication is still in progress, however at the end of the chapter we present the microscope images of the MEMS elements and the measurements of MEMS vertical deflection.

5.1 Process flow

Basic M&NEMS technological platform has been described in chapter 2. The same platform is used in the first steps of MEMS wafer fabrication, however the further process is different from the one described in chapter 2 - the electrical connections are not realized by direct metalization of the MEMS wafer but they are realized on the sealing wafer. Both wafers are fabricated simultaneously, their process flow presented on fig. 5.1 consists of the following steps:

MEMS wafer :

(a) we start with the SOI wafer,
(b) nanogauges are defined,
(c) nanogauges are covered with protective Silicon Oxide layer,
(d) Silicon epitaxial layer is grown,
(e) mechanical structures are defined in the epitaxial layer.

Sealing wafer :

(f) we start with a standard silicon wafer which is oxidized and the metal layer for the electrical network is deposited,
(g) electrical network is realized in the metal layer,
(h) the electrical network is isolated with the oxide layer and the vias for electric connections are realized,
(i) finally the metal which is used in eutectic bonding is deposited.

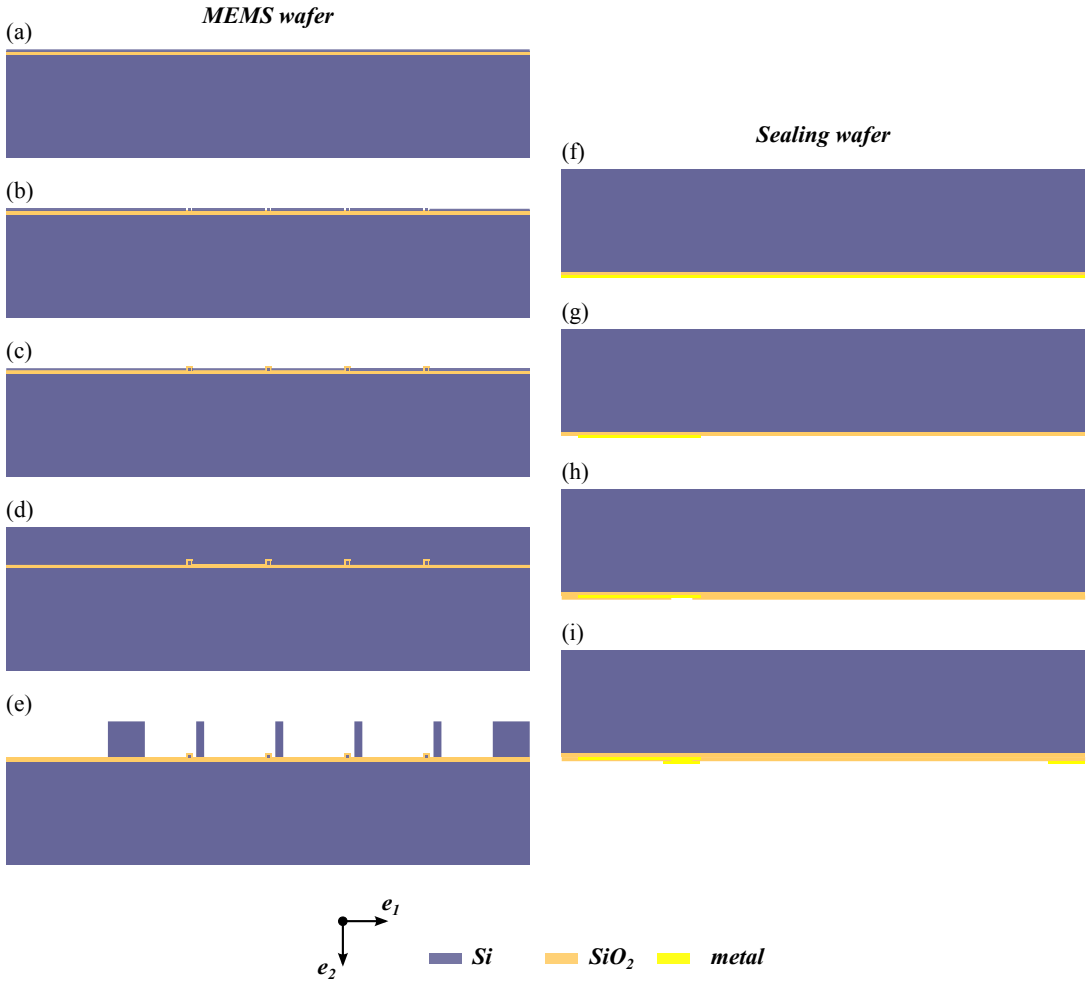

Figure 5.1: Side view of MEMS wafer process flow (not to scale).

Metal patterns on the sealing wafer that are used in eutectic bonding have two functions: they provide electric connections to MEMS and they form the sealing ring around the MEMS structures to provide the mechanical attachment and hermeticity. With both MEMS and sealing wafers prepared, we pursue the process (fig. 5.2):

Sealing and process finish :

(a) surfaces of both wafers are prepared and the eutectic bonding in vacuum is realized,

(b) both wafers, that are initially 725 μm thick are thinned down to 300 μm with use of grinding. High quality surface is then obtained with use of CMP (Chemical Mechanical Polishing) process,

(c) the inlet and outlet acoustical vents are etched in DRIE process, the oxide is used as an etch-stop layer. At the same time we etch the cavity that enables the access to the electric pads (left side of the chip),

(d) The last step involves the vapor HF etching of the oxide to open the acoustic vents and then to release the MEMS structures.

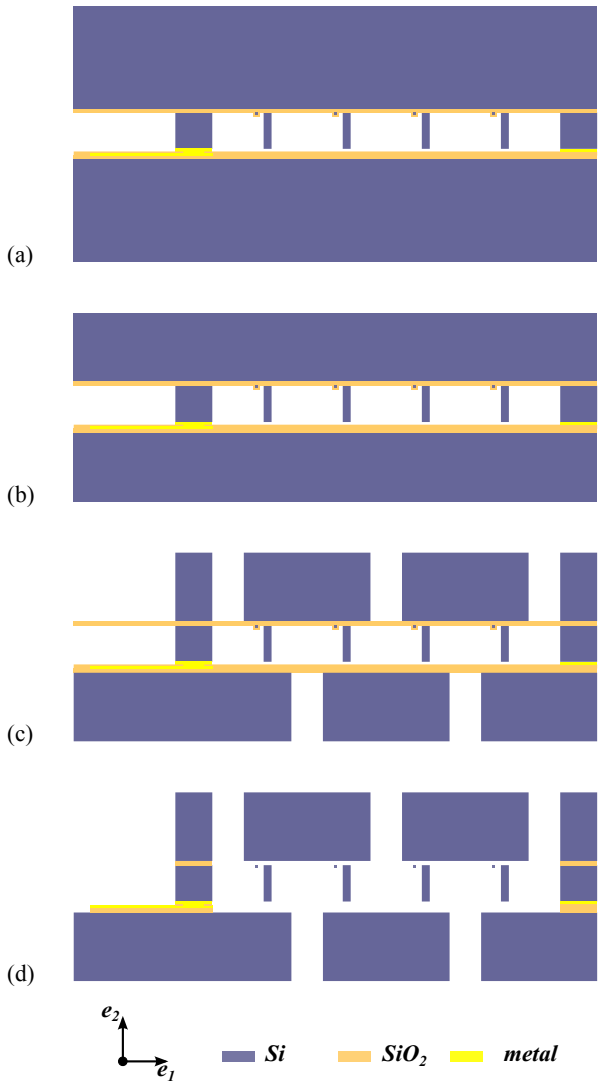

Figure 5.2: Side view of wafer bonding and process finish (not to scale).

5.2 Advances and difficulties encountered in microfabrication

Fabrication process is carried out at CEA-LETI. Figure 5.3 illustrates the final shape of MEMS part with zoom on nanogauge and ellipses indicating the future positions of the inlets (red) and the outlets (blue). One of the MEMS wafers has been withdrawn from the process at this point, then the mechanical structures have been released with HF to investigate the out-of-plane deflection of the beams (see section 5.3).

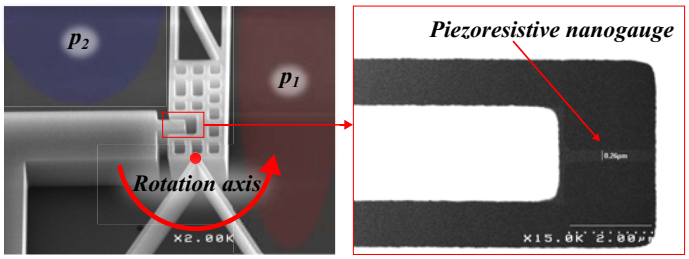

Figure 5.3: SEM image: top view of the microbeam and the nanogauge.

On figure 5.4 we present the patterns on finished sealing wafer: the sealing ring that assures hermeticity, the electrical pads for wire bonding and the paths that distribute the signal (Wheatstone bridge wiring: power supply and signal acquisition; wiring of test electrode for MEMS electrostatic activation test). The electrical and sealing metal layers are isolated with use of the oxide layer and the vias are prepared to connect the paths with the nanogauges.

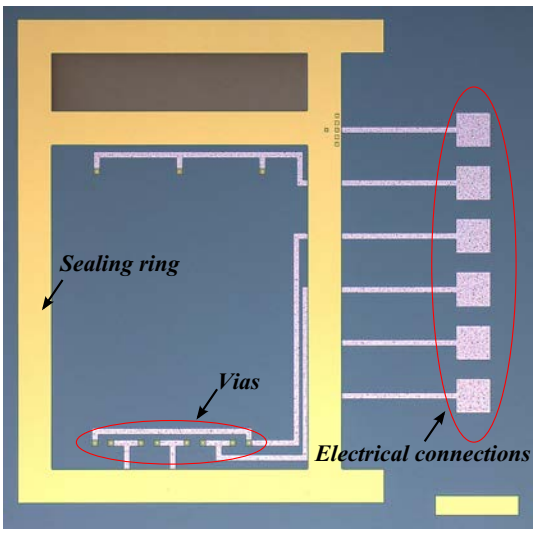

Figure 5.4: Optical microscope image: top view of the sealing wafer with the sealing ring, the electrical connections and the vias used for Wheatstone bridge wiring.

Both MEMS and sealing wafer have been bonded, the infrared inspection (fig. 5.5) showed that the electrical paths are well aligned with the corresponding patterns on MEMS wafer.

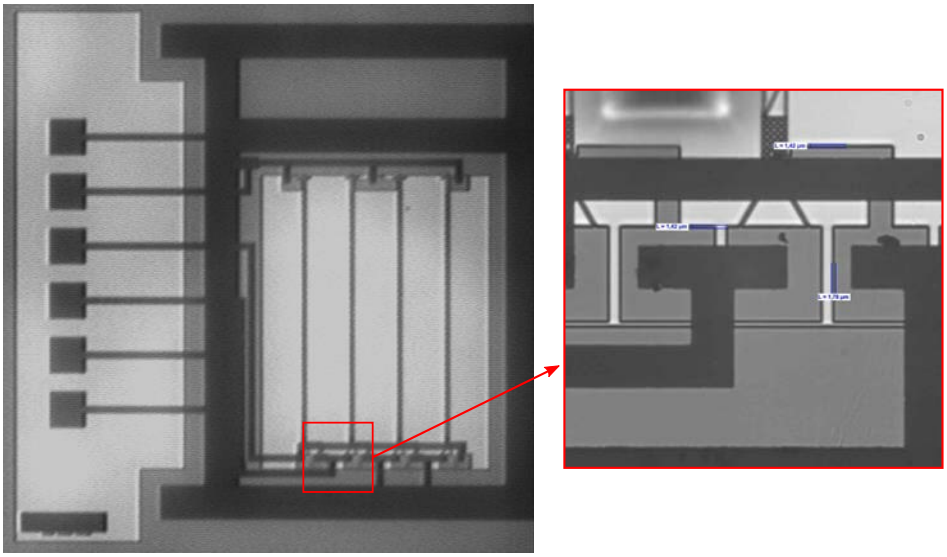

Figure 5.5: Infrared microscope image of the bonded wafers. Zoom reveals the points where the electrical connection is provided to the nanogauges.

Encountered difficulties

Designed MEMS microphone requires the modification of standard M&NEMS process flow. Some of processes prepared for previous M&NEMS sensors contain the wafer eutectic bonding, however it is the last step in fabrication process. On the contrary the process flow of the microphone continues after the eutectic bonding and includes grinding and essential step: etching of acoustic vents.
Several of the assembled wafers were damaged in the steps following the bonding. The possible causes are associated to the poor bonding strength combined with the fact that the wafers are weakened because of the grinding. This process have been already optimized and the prototype should be ready shortly.

5.3 Out-of-plane deflection of MEMS

Mechanical architecture of discussed microphone includes relatively long structures anchored at one of the extremities. Because of that one may suspect that the released structures tend to deflect in vertical (out-of-plane) direction (fig. 5.6). Vertical deflection is a known problem in MEMS, the most common origin of long structures deflections comes from the mismatch between the thermal expansion coefficients of the various materials of MEMS stack. It is true for the multilayered MEMS, however in our case the MEMS beam is fabricated entirely from the crystalline Silicon and the foregoing interpretation is no longer valid.
However if we study the process flow (see section 5.1) we see that the beam is in fact composed of two crystalline Silicon layers: first one which is 250 nm thick in which the nanogauges are defined and the second layer which is 10 µm thick. The first layer is the one of SOI wafer whereas the second layer is grown in epitaxial process. We do not know if the both process were done under the same conditions (temperature, pressure), therefore we presume that the interface of both layers is not free of the crystal lattice defects. This defects may lead to the internal stress and finally (after the release of the structure) the stress relaxation leads to the vertical deflection of the beam.

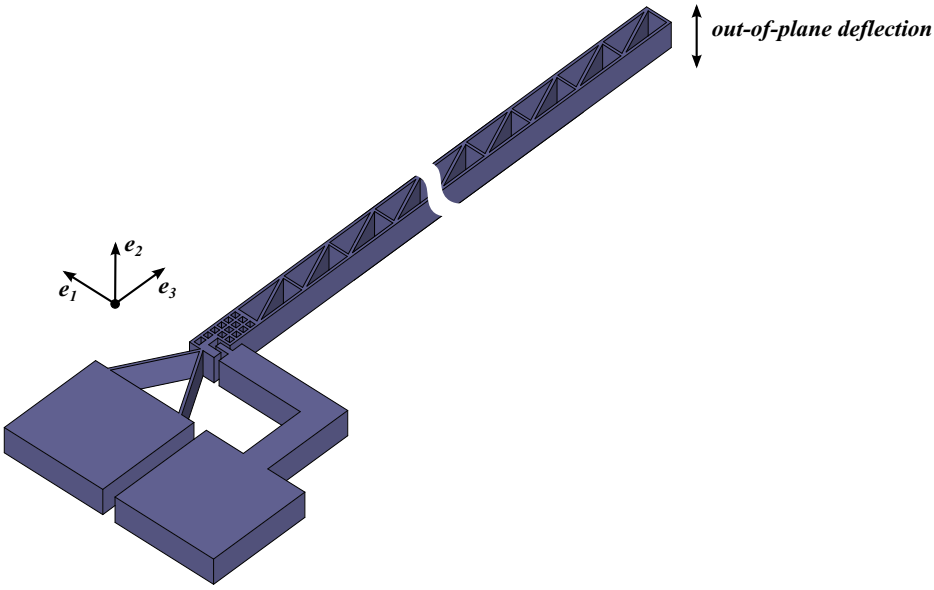

Figure 5.6: Schematic of out-of-plane deflection of the microphone beam.

Examination of the internal stress is not in the scope of the presented thesis, however there is a need of such statistical studies (with focus on different geometries and process parameters) for further development of the M&NEMS microphone. The considerations of stress-induced deflection in this thesis are restricted to the designation of the overall trends. The measurements (fig. 5.7) were made with use of optical profilometer Veeco Wyko NT9100 (white light interferometer) on the MEMS wafer withdrawn from the fabrication process before the wafer level packaging and released with vapor HF.

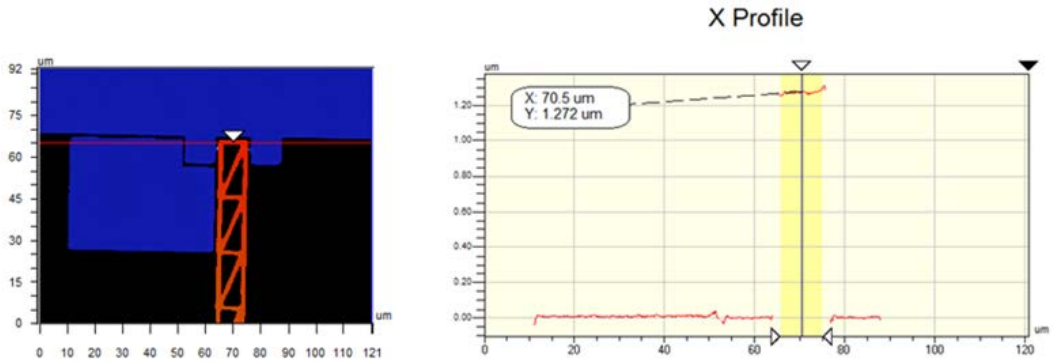

Figure 5.7: Optical interferometry measurements sketch.

We have tested the beams with length of 500, 740 and 1000 µm. The results gathered on the fig. 5.8 shows that the deflection does not depend on the width of the hinge (cd_h) and beam (cd_m) members (for the description of geometric parameters see section 4.1), however we see clearly that the deflection increases with the beam length and it is within the range 0.50 - 2.75 µm. The designs where the deflection exceeds 2 µm (distance between the beam and the sealing wafer) should be avoided since the beams will get in contact with the sealing wafer and the microphones with such beams will not work.

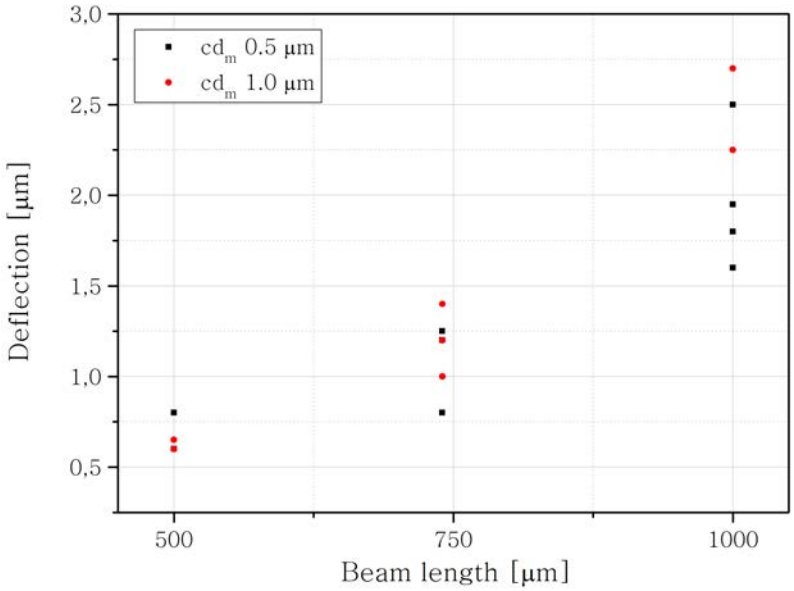

Figure 5.8: Deflection of the beam extremity depending on the beam length.

5.4 Chip scale packaging

As shown in section 4.3, the MEMS dice housing remains an equal element of the microphone that influences its final performance. Therefore for the final functional test, the MEMS dice should be packaged in the same manner as the existing commercial products. Such solution has been foreseen for the presented M&NEMS microphone, however our package will be introduced after the overview of the popular packages used in the industry.

5.4.1 Technology overview

MEMS microphones are typically assembled in LGA (land grid array) package that is compatible with surface mount technology. It can be soldered under the same conditions as the other SMD elements. Depending on the sound port position we distinguish two package types called the top and the bottom port. Although the bottom port architecture is more problematic (inlet vent must be drilled in the PCB laminate - fig. 5.9), it is more common since it enables increase of the package backvolume.

Knowles SPU0410LR5H
Most of the MEMS microphones packages resemble this of Knowles SPU0409LE5H microphone. The packages are in form of thin rectangular cuboids (typical dimensions are around 4 x 3 x 1 mm^3) where the electric pads are located on the surface of the PCB (see fig. 5.9). The surface with electric pads that after soldering comes into contact with PCB indicates the bottom of the package. The embodiment consists of PCB card equipped with soldering pads and sound port. MEMS and ASIC dies are covered with metal lid which is attached to the PCB with the conductive adhesive. Thanks to System Plus Consulting report [16] we may have a look on the cross-section of the Knowles microphone package (fig. 5.10). MEMS die is aligned with the PCB sound port so the sound propagation path is reduced to the minimum. The connections between MEMS and ASIC (that is placed aside) are realized with wire-bonding (fig. 5.11), then the

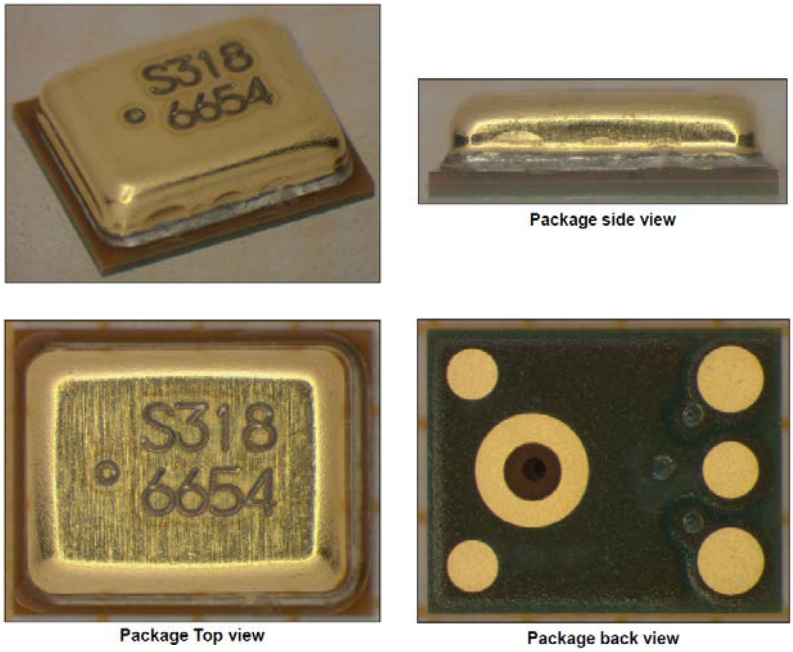

Figure 5.9: Overview of Knowles SPU0409LE5H bottom port package [16].

connections and ASIC are covered with protective resin. Cross-sectional view reveals additionally the vias in PCB that provide the integrated circuit output signal to the PCB soldering pads.

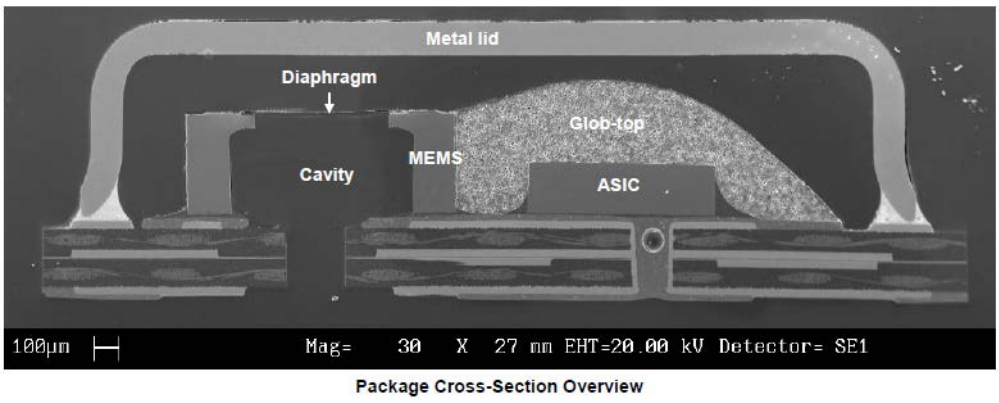

Figure 5.10: Cross-section of Knowles SPU0409LE5H package [16].

Epcos T4000 and T4060

Epcos presents another approach for MEMS microphone packaging (fig. 5.12). It is still bottom port package, however the MEMS and ASIC are upside-down (microphone diaphragm is facing the substrate while the back volume cavity is created only with internal MEMS cavity). The dies are placed side by side and the electrical connections are provided with golden bumps. Epcos uses the ceramic substrate and the sealing is first realized with the elastic films and then it is finished with metal layer (fig. 5.13). This approach reduces drastically the volume of the package, which in case of T4060 model is 2.65 x 1.81 x 0.95 mm^3.

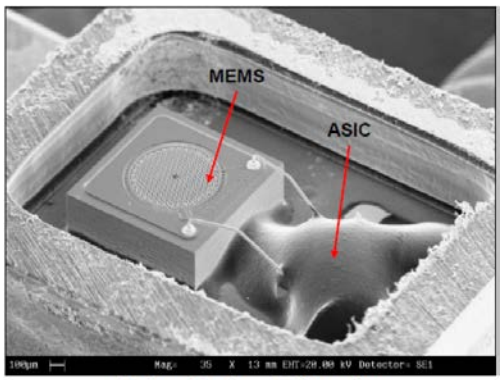

Figure 5.11: Wire-bond connections in Knowles SPU0409LE5H package [16].

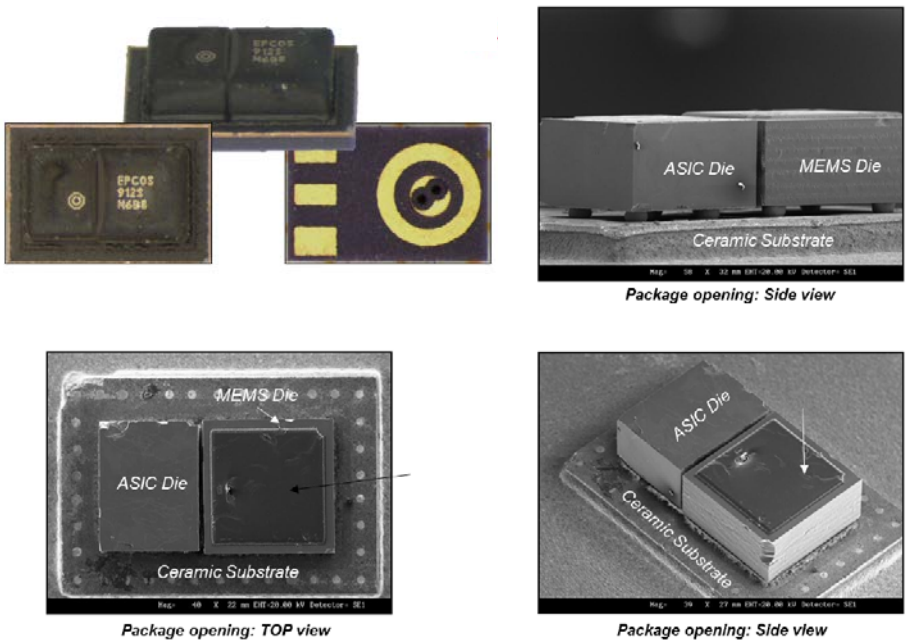

Figure 5.12: Overview of Epcos T4060 bottom port package [80].

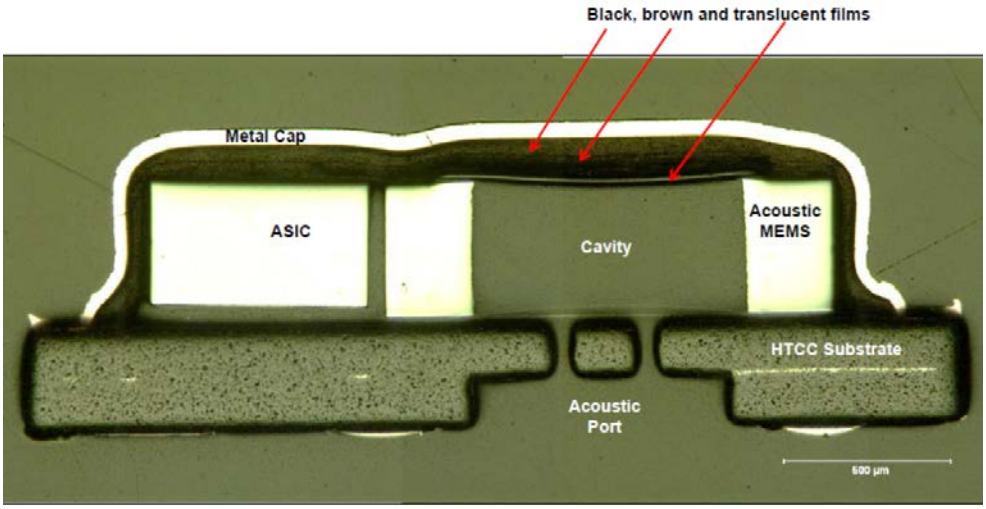

Figure 5.13: Cross-section of Epcos T4000 package [81].

Akustica AKU230

Akustica is the only company that managed to integrate the readout electronics directly into the MEMS microphone dice (fig. 5.14:Die Overview). This asset facilitates

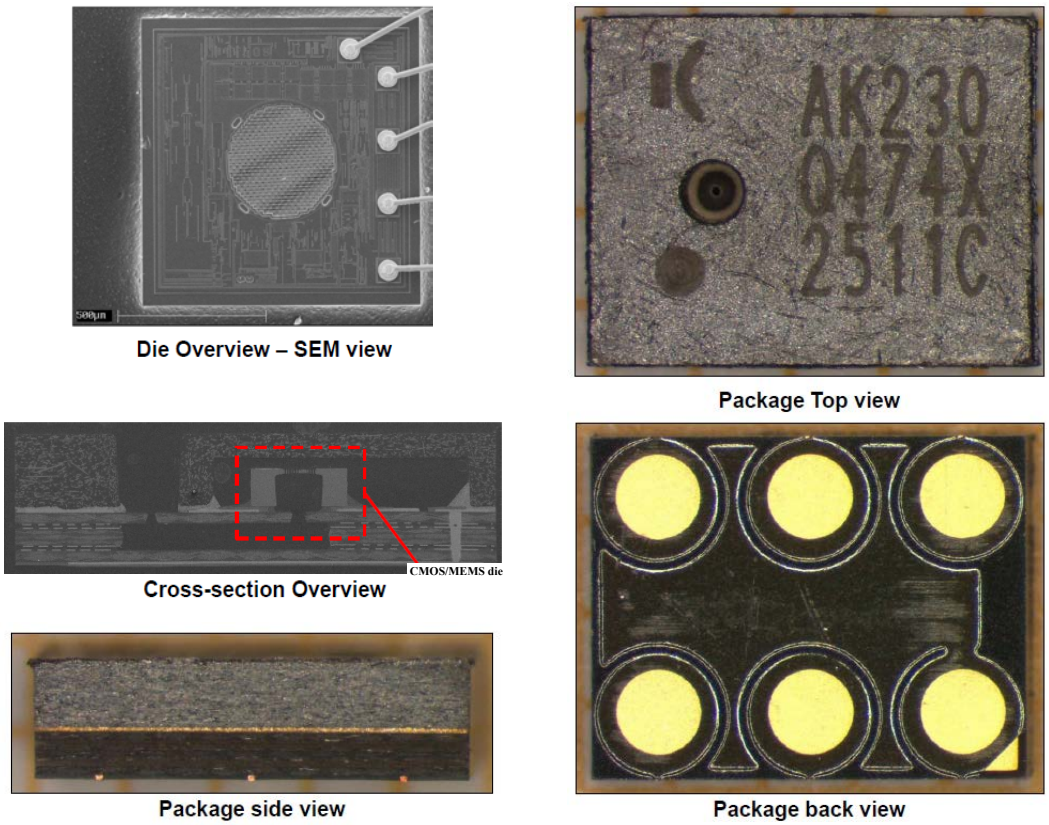

Figure 5.14: Overview of Akustica AKU230 top port package [82].

the chip-scale packaging and (as shown by Akustica) broaden the packaging possibilities. The problem of top port packages is a small backvolume which is problematic

for low frequency response. This issue has been resolved by Akustica with the sophisticated package that contains the acoustic system shown on package cross-section (fig. 5.14:Cross-section Overview). This advanced inlet vent assures that MEMS is working roughly under the same acoustic conditions as in bottom port package.

5.4.2 Proposed solution

While selecting the most suitable packaging for the considered microphone we must take into account that it is a device under development and it is currently fabricated on a small-scale. Under such circumstances the prepared package must fulfill the following requirements:

- package back volume have to correspond to the one used in commercial MEMS microphones,
- for the first tests the MEMS and ASIC dies wont be integrated into one package,
- during first tests the readout is realized by use of standard laboratory equipment or the dedicated discrete electronics,
- package has to provide simple interface for the tests instruments (preferred coaxial connections),
- to facilitate testing of several chips, MEMS has to be integrated with one of the standard packages (for example DIP - *Dual In-line Package*).

Regarding the above requirements we have decided to prepare the interface that consists of three elements: the PCB card (support) with coaxial connections and socket for the DIP 16 (fig. 5.15), the DIP 16, and the microphone package that is similar to the one used by Knowles (fig. 5.16). The Knowles package made of miniature PCB and the metal lid was chosen as a model because it is a package relatively easy to prepare for the small-scale fabrication.

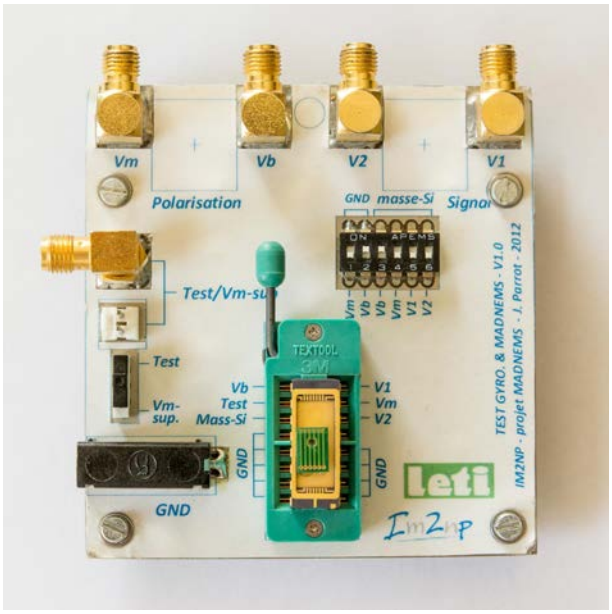

Figure 5.15: Support board designed and fabricated by IM2NP.

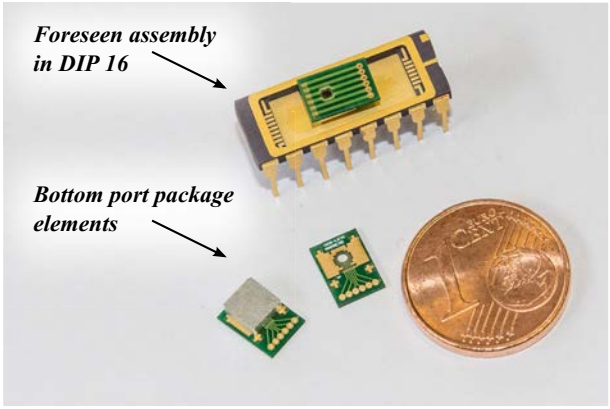

Figure 5.16: Elements of package and interface for M&NEMS microphone tests.

Two types of PCB were prepared: dedicated for top and bottom port configurations, however we will focus on bottom port type (fig. 5.17). PCB is prepared basing on double sided, 400 µm thick FR 4 substrate with electric pads surface finished accordingly to the requirements of wire bonding process.
Acoustic sound port of 1 mm diameter is situated below the MEMS die. The "cross" and "L" alignment marks are for MEMS and metal lid assembly. This marks along with adjacent rectangular fields are not covered with solder mask in order to ground MEMS die and the lid. Finally PCB has two sets of electric pads - one for MEMS-PCB wire bonding and the second for PCB-DIP 16 wire bonding connections.

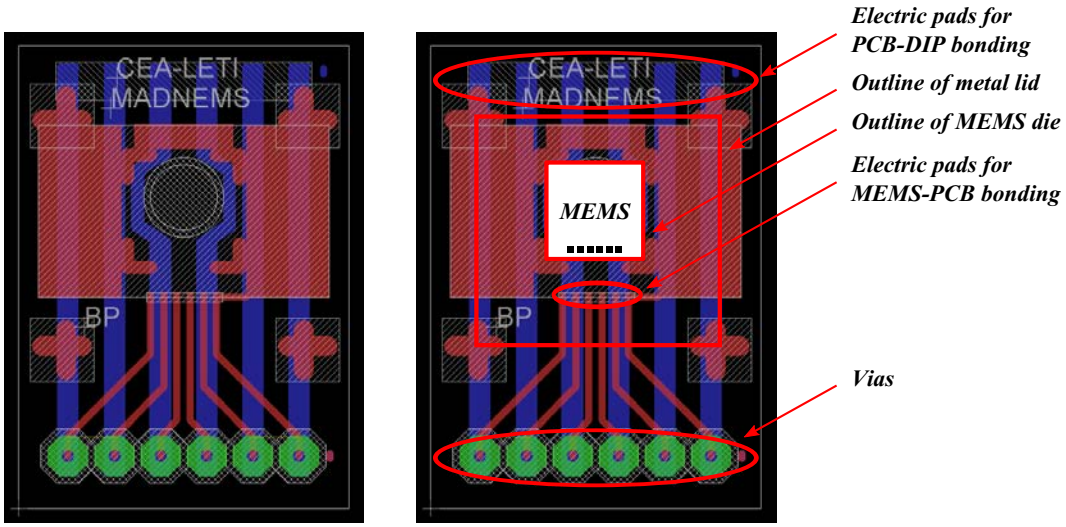

Figure 5.17: PCB substrate prepared for M&NEMS microphone chip-scale packaging (bottom port). Left side presents the PCB layout while the right side indicates the specific elements of the PCB.

Miniature substrates prepared for the MEMS packaging are problematic in terms of PCB depaneling (fig. 5.18). The overall size of the individual PCB is 5 x 7 mm^2 and the spacing between the copper paths and the cut line is around 200 µm, while the standard methods of depaneling such as V-Scoring and break-routing [83,84] impose the minimum spacing between the board and cut path of 200-500 µm and the minimum PCB size of 5 mm.

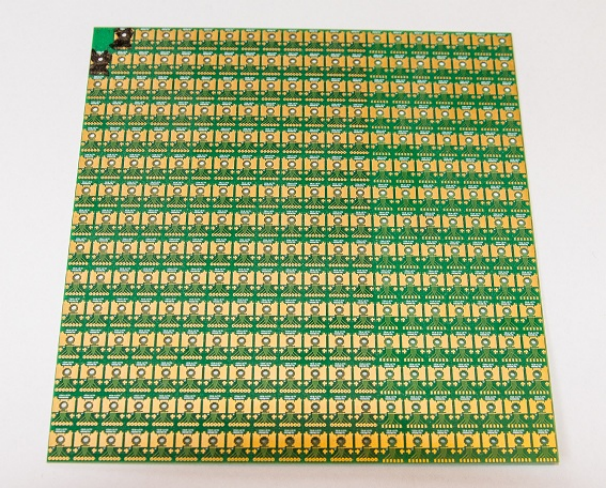

Figure 5.18: Panel with 300 miniature substrates for M&NEMS microphone. Panel overall size is 10.0 x 10.5 cm^2.

Depaneling with popular CO_2 laser is not suitable either since it damages the PCB due to generation of high temperature. Finally the depaneling was realized with use of UV laser that reduces the cutting path and the generated heat ("cold ablation") [85].

Summary

In this chapter we have presented the technology prepared for the fabrication of the new type of MEMS microphone. The fabrication revealed couple difficulties, however the process has been already optimized.
The specification of the microphone makes it problematic in terms of packaging. There are no standard packages available for MEMS microphones, therefore the in-house solution has been prepared. Our packaging solution ensures that the designed MEMS prototype will work in the similar conditions to the ones of the commercial products.

Chapter 6

Approach to MEMS microphone calibration

While the designed microphone is under fabrication, the functional test approach has been developed and validated on a commercial MEMS microphone. The chapter begins with discussion on a suitable methods for MEMS microphone sensitivity determination. Impedance tube and anechoic chamber are appointed to characterize the microphone under pressure-field and free-field conditions. Moreover it is shown that the anechoic chamber experimental setup is suitable for microphone noise measurements.

6.1 Selection of suitable calibration methods

By term of calibration we mean the investigations of the microphone frequency response (typically from single hertz to 100 kHz) and the sensitivity at 1 kHz. Numerous calibration methods are standardized by the International Electrotechnical Commission (IEC). The method depends on the microphone which can have the laboratory (LS) or working (WS) standard and on the working environment (see the work of R. Barham, V. Nedzelnitsky or E. Frederiksen for further details [86–88]). The most precise microphones (laboratory standard), which are then used as a standards for the most important measurements and for the calibration of the less precise microphones (working standard) are calibrated with primary calibration techniques. However we need to remember that the goal of this thesis is to work on the microphone that is in early stage of development. That is why we will not discuss the primary calibration methods and we will go directly to the secondary calibration methods.
Secondary calibration is usually made by comparison of tested microphone to the reference microphone that have higher precision. It can be done simultaneously with reference microphone placed next to the tested microphone or the measurements of two microphones may be done one after another. At this point we need to consider the working environment which has an influence on the frequency response of the microphone at higher frequencies (see fig. 6.1). Working environment (after L.L. Beranek [89]) corresponds to the type of sound field in the vicinity of the diaphragm:

- *pressure-field* - sound pressure is distributed uniformly over the diaphragm (microphone is introduced into the coupler),
- *free-field* - this type of field is obtained inside the anechoic chamber where the sound waves reflected from the walls are negligible in comparison to the sound waves coming directly from the source,

- *diffuse-field* - where the sound wave of similar amplitude may arrive from the arbitrary direction.

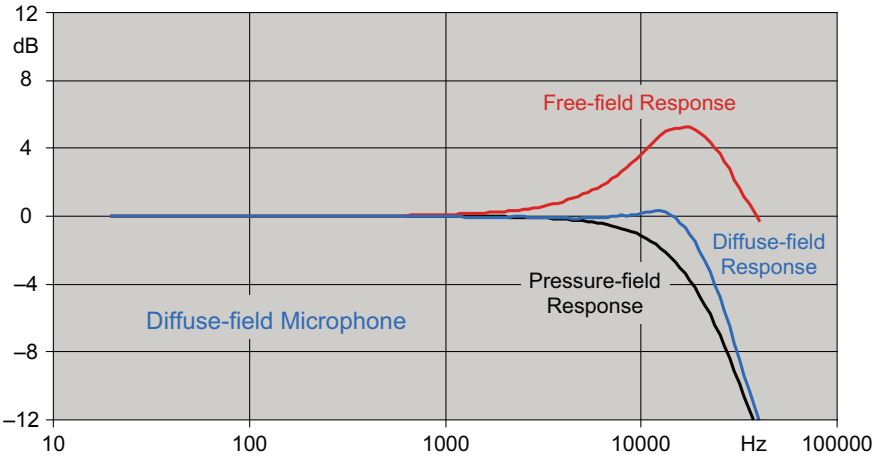

Figure 6.1: Example of pressure-field, free-field and diffuse-field frequency responses of diffuse-field microphone given by E. Frederiksen [88].

6.2 Specimen description

Approach to functional characterization of MEMS microphone is presented with use of commercial INMP504ACEZ microphone. It is an analog MEMS microphone in bottom port configuration. It was designed by Analog Devices as a part of MEMS microphone line that was lately purchased by InvenSense (Q4 2013).

Microphone specification

Selection of the microphone was done based on its features (table 6.1, fig. 6.2) and the asset of a wide range of associated application notes.

Acquisition chain prerequisites and architecture

The acquisition chain starts with MEMS microphone which is a capacitive sensor with integrated impedance converter and output amplifier. Eventually the signal is digitized by OROS analyzer, however the microphone has to be connected to the analyzer through the additional discrete electronics which provide the signal conditioning.
Requirements for the discrete electronics are as following:

- provide relevant gain of the output signal for efficient use of the ADC,
- cut-off the redundant signal (signal below and above sensor bandwidth, unwanted signal coming from impedance tube setup),
- self noise of discrete electronics has to be lower than the microphone noise.

We have chosen to feed the signal coming from the microphone to the amplifier prepared with use of operational amplifier in non-inverting configuration (see fig. 6.3). Preliminary measurements in impedance tube done with use of laboratory reference

Table 6.1: Specifications of INMP504 MEMS microphone [90]

Parameter	Value		Conditions
Performance			
Sensitivity	-38	dBV	1 kHz, 94 dB SPL
Signal-to-Noise Ratio (SNR)	65	dBA	
Equivalent Input Noise (EIN)	29	dBA SPL	
Frequency response	0.1 to 20	kHz	limited by -3 dB point
Maximum acoustic input	120	dB SPL	
Power supply			
Supply voltage	1.6 - 3.3	V	
Output characteristics			
Maximum output voltage	0.35	V	120 dB SPL input
Noise floor	-103	dBV	20 Hz - 20 kHz, A-weighted, rms

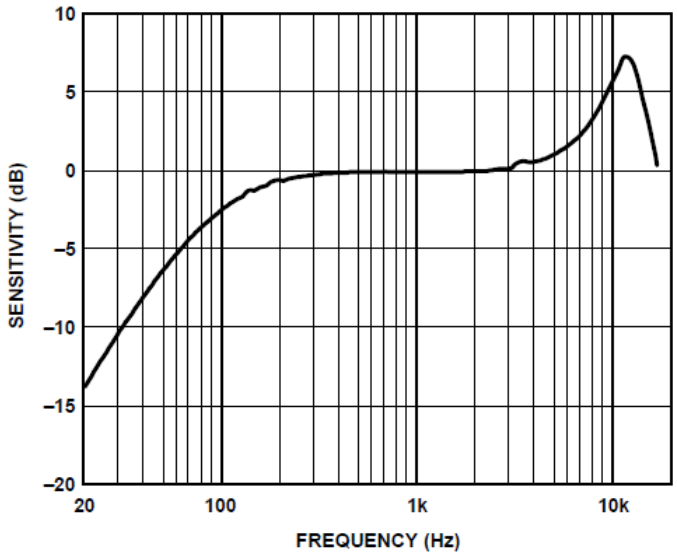

Figure 6.2: Typical frequency response of INMP504 MEMS microphone [90].

microphone (B&K) have shown that the sound pressure level inside the tube is in range of 60 - 120 dB. Therefore the amplification has been set by the ratio of the resistors $R1$ and $R2$ and adjusted for the expected SPL. All of the components are situated on

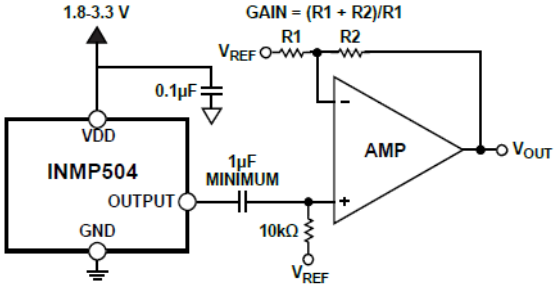

Figure 6.3: Readout electronics selected for INMP504 microphone [90].

the same side of PCB while the sound port is on the opposite side (see fig. 6.4). This

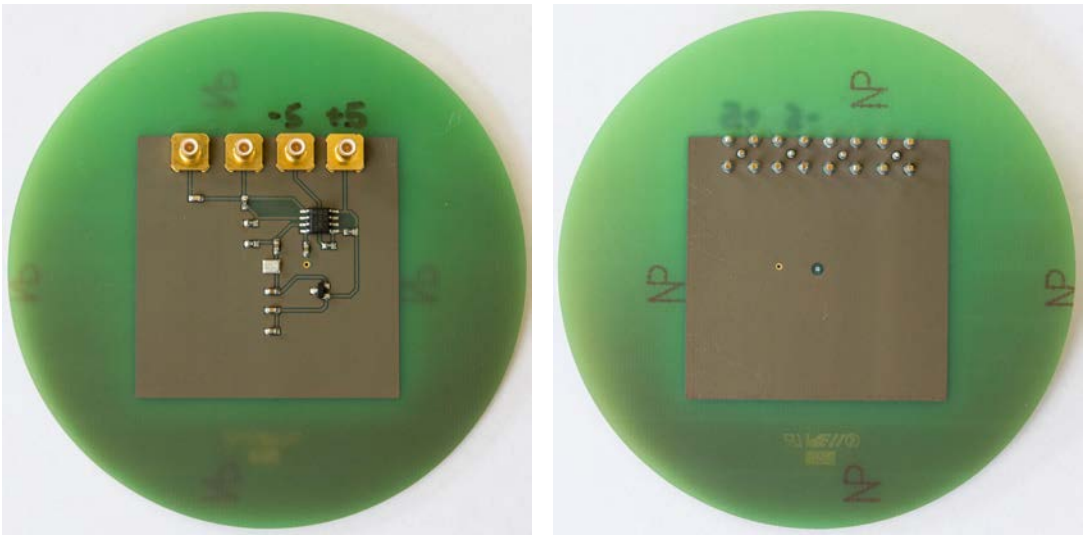

(a) Top view - this side of PCB is contains discrete electronics

(b) Bottom view - this side of PCB is exposed to sound pressure

Figure 6.4: PCB prepared for INMP504 MEMS microphone.

configuration was chosen to eliminate the perturbation of sound field in the vicinity of the microphone sound port. SMB connectors have been chosen for the pcb interface. The bias voltage 5 V which is used for operational amplifier is dropped to 1.8 V by the voltage regulator to power the MEMS microphone.

6.3 Influence of experimental setup on microphone response

Before starting the characterization of the microphone let us examine the measurements chain of the experimental setup (fig. 6.5). It consists of:

- the generator that introduces the signal driving the loudspeaker u_{exc},

- the loudspeaker that transduces the voltage signal into the acoustic pressure according to its transfer function $H_L(s)$,
- the acoustic pressure that propagates inside the acoustic domain and introduces transfer function $H_A(s)$,
- the MEMS microphone (marked dut - device under test) and the reference microphone(s) that capture(s) the pressure fluctuations according to their sensitivities S_{dut} and S_{ref}.

Figure 6.5: Block diagram of experimental setup.

Figure 6.6 represent the experimental setup used for MEMS microphone characterization. This representation is valid regardless of the sound field type (pressure-field and

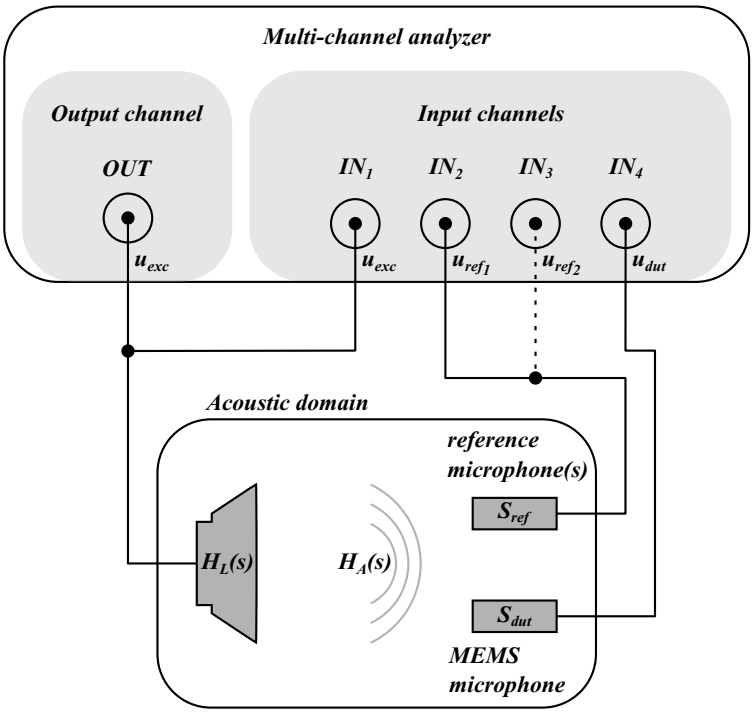

Figure 6.6: Graphic representation of experimental setup.

free-field) and the only distinction is the amount of reference microphones. Pressure-field investigations described in section 6.4 need two reference microphones - microphone x_1 with signal u_{ref_1} connected to the second input channel of the analyzer and microphone x_2 with signal u_{ref_2} connected to the third input channel of the analyzer. On the contrary the free-field investigations (section 6.5) require only one reference microphone with signal identified as u_{ref} and connected to the second input channel of the analyzer.

If we consider all of the elements of of the experimental setup, the signal coming from MEMS microphone becomes:

$$u_{dut} = u_{exc} \left[H_L H_A S_{dut} \right]. \tag{6.1}$$

To extract the sensitivity of the microphone we need to suppress the excitation signal along with the loudspeaker and the acoustic domain transfer functions. This is feasible if we use one reference microphone placed next to the investigated microphone. In such case the responses of both microphones are linked to the same transfer functions H_L and H_A. The reference microphone signal u_{ref} is:

$$u_{ref} = u_{exc} \left[H_L H_A S_{ref} \right]. \tag{6.2}$$

Knowing the sensitivity S_{ref} of reference microphone (that is given for the frequency of 1 kHz and is assumed to be equal over the range given by the manufacturer), we may appoint the sensitivity of characterized microphone:

$$S_{dut} = \frac{u_{dut}}{u_{ref}} S_{ref}. \tag{6.3}$$

Measurements described in section 6.4 employ two reference microphones located on different positions than the investigated microphone. The sound pressure applied to the MEMS microphone is then calculated analytically. This calculations suffer from the error introduced by the different acoustic transfer functions (H_{Adut}, H_{Aref1} and H_{Aref2}) measured by all three microphones:

$$u_{dut} = u_{exc} \left[H_L H_{Adut} S_{dut} \right], \tag{6.4}$$

$$u_{ref1} = u_{exc} \left[H_L H_{Aref1} S_{ref} \right], \tag{6.5}$$

$$u_{ref2} = u_{exc} \left[H_L H_{Aref1} S_{ref} \right]. \tag{6.6}$$

Suppression of transfer function mismatch in case of response from three microphones is not trivial. Therefore in our considerations we assume that the resulting error is negligible and we proceed with measurements. The method for pressure-field characterization is validated subsequently in subsection 6.4.1.

6.4 Pressure-field investigations with use of impedance tube

Presented technique of microphone sensitivity investigation is based on the impedance tube (fig. 6.7). It is measuring instrument build of a cylindrical waveguide with acoustic pressure source placed at one of the extremities. For the purpose of a measurements, the opposite extremity is considered to be rigid with investigated microphone mounted at the $x = 0$. Impedance tube considerations are true only in case of planar propagation of sound waves inside the tube; to ensure planar wave propagation the following condition must be fulfilled:

$$f_{max} < \frac{c_0}{2D_{IT}}. \tag{6.7}$$

We will now show, that with use of two well known, calibrated microphones (x_1 and x_2) integrated to the border of a waveguide we can express the pressure field $p(x)$ over the entire length of a impedance tube:

$$p(x) = p_i(x) + p_r(x) = Ae^{jkx} + Be^{-jkx}, \tag{6.8}$$

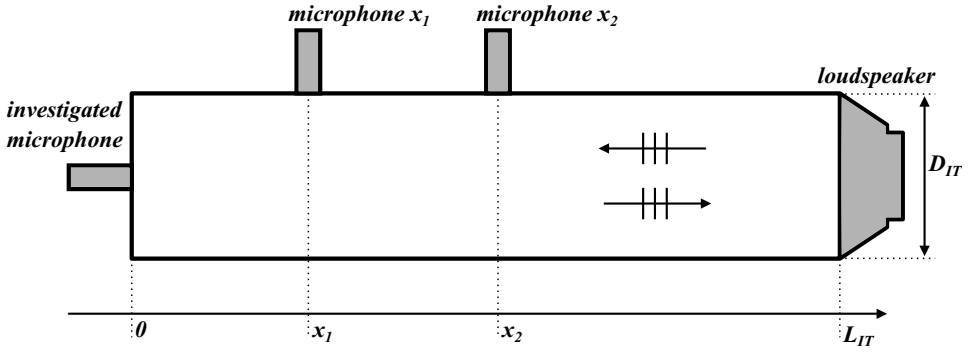

Figure 6.7: Sketch of impedance tube test set.

where $p_i(x)$ and $p_r(x)$ are the pressure of incident and reflected waves, A and B are the complex amplitudes, and k is a wave number ($k = \frac{2\pi f}{c_0}$). In order to determine $p(x)$, unknown variables A and B has to be found; for that purpose we prepare set of two equations with use of microphones x_1 and x_2:

$$\begin{bmatrix} p(x_2) \\ p(x_1) \end{bmatrix} = \begin{bmatrix} e^{jkx_2} & e^{-jkx_2} \\ e^{jkx_1} & e^{-jkx_1} \end{bmatrix} \begin{bmatrix} A \\ B \end{bmatrix}. \tag{6.9}$$

Please note that A and B can be found from equation 6.9 if the square matrix standing before A and B is invertible:

$$\begin{vmatrix} e^{jkx_2} & e^{-jkx_2} \\ e^{jkx_1} & e^{-jkx_1} \end{vmatrix} \neq 0. \tag{6.10}$$

To meet the foregoing condition $\sin k(x_2 - x_1) \neq 0$, thus $\Delta x \neq 0$, it means that the frequency has to in the range:

$$0 < f < \frac{c_0}{2\Delta x}. \tag{6.11}$$

Reproduction of pressure field inside the tube with use of two microphones is possible if Δx is shorter than the shortest wavelength; according to Shannon sampling theorem [91]:

$$\Delta x < \frac{\lambda_{min}}{2} = \frac{1}{2}\frac{c_0}{f_{max}}. \tag{6.12}$$

With the assumptions from equations 6.11 and 6.12, A and B are described by the following relation:

$$\begin{bmatrix} A \\ B \end{bmatrix} = \frac{1/2j}{\sin k(x_2 - x_1)} \begin{bmatrix} e^{-jkx_1} & -e^{-jkx_2} \\ -e^{jkx_1} & e^{jkx_2} \end{bmatrix} \begin{bmatrix} p(x_2) \\ p(x_1) \end{bmatrix}, \tag{6.13}$$

For further consideration we will introduce velocity field with use of Euler equation:

$$\rho_0 \frac{\partial v(x)}{\partial t} = -\frac{\partial p(x)}{\partial x}, \tag{6.14}$$

thus:

$$Z_0 v(x) = -Ae^{jkx} + Be^{-jkx}. \tag{6.15}$$

We may now describe pressure and velocity fields inside the tube:

$$\begin{bmatrix} p(x) \\ Z_0 v(x) \end{bmatrix} = \begin{bmatrix} e^{jkx} & e^{-jkx} \\ -e^{jkx} & e^{-jkx} \end{bmatrix} \begin{bmatrix} A \\ B \end{bmatrix}, \tag{6.16}$$

finally pressure and velocity at $x = 0$ equals:

$$\begin{bmatrix} p(0) \\ Z_0 v(0) \end{bmatrix} = \frac{1}{\sin k(x_2 - x_1)} \left\{ \begin{bmatrix} -\sin kx_1 \\ j \cos x_1 \end{bmatrix} p_2 - \begin{bmatrix} -\sin kx_2 \\ j \cos x_2 \end{bmatrix} p_1 \right\}. \tag{6.17}$$

By introducing $x_m = \frac{x_1+x_2}{2}$ and $d = \frac{x_2-x_1}{2}$ into equation 6.16, we obtain:

$$\begin{bmatrix} p(x) \\ Z_0 v(x) \end{bmatrix} = \frac{1}{\sin kd} \begin{bmatrix} \sin k(x - x_m) \\ j \cos k(x - x_m) \end{bmatrix} \frac{p_2 - p_1}{2} + \frac{1}{\cos kd} \begin{bmatrix} \cos k(x - x_m) \\ -j \sin k(x - x_m) \end{bmatrix} \frac{p_2 + p_1}{2} \tag{6.18}$$

$$\begin{bmatrix} p(0) \\ Z_0 v(0) \end{bmatrix} = \frac{1}{\sin kd} \begin{bmatrix} -\sin k(x_m) \\ j \cos k(x_m) \end{bmatrix} \frac{p_2 - p_1}{2} + \frac{1}{\cos kd} \begin{bmatrix} \cos k(x_m) \\ j \sin k(x_m) \end{bmatrix} \frac{p_2 + p_1}{2} \tag{6.19}$$

Alternative measurement set
The foregoing measurement set and the presented analytical sound pressure designation may suffer of some incertitude's. This incertitude's, identified in equation 6.19 are:

- value of speed of sound c_0,
- misalignment of the reference microphones (x_1, x_2) ,
- frequency response of the x_1 and x_2 microphones (sensitivity is calibrated only for $f = 1$ kHz).

Moreover the reposes of reference microphones placed at different positions inside the tube manifest different transfer functions of the tube (see section 6.3). Possible solution of this inaccuracies is to use of single reference microphone placed at the end of a tube together with investigated microphone (see fig. 6.8).

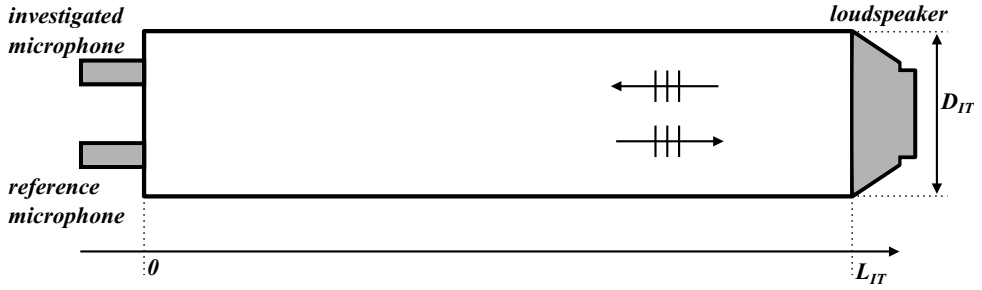

Figure 6.8: Alternative configuration of measurement set.

6.4.1 Pressure-field experimental setup and measurements

The experimental setup for pressure-field investigations is presented on figure 6.9. We may see the impedance tube build of PVC with the loudspeaker attached on the right side and the tested microphone (MEMS or the reference microphone) at the opposite extremity of the tube. Two calibrated reference microphones x_1 and x_2 are positioned at the side of the tube.

The aim of the first type of measurements was to validate the method presented at the beginning of the section. For that purpose we have used three well known, calibrated microphones. Two of them were used to identify the pressure at the end of the tube with

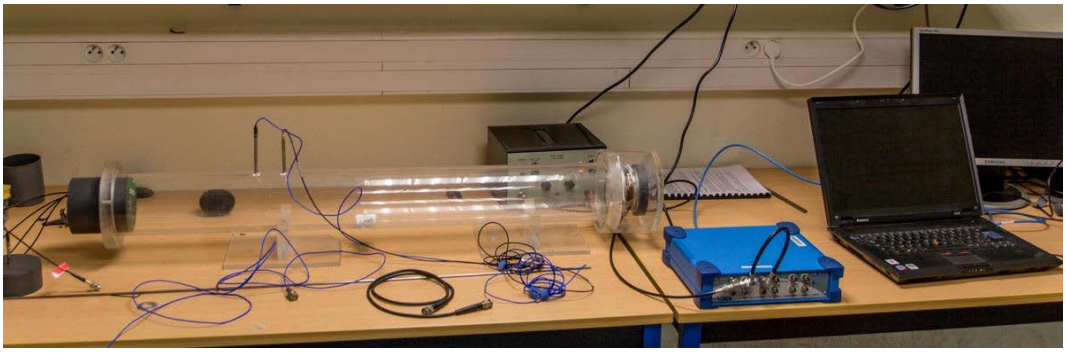

Figure 6.9: Experimental setup used for pressure-field measurements.

use of equation 6.18 while the third one measured the pressure at the end of the tube directly. Comparison of experimental data and identified data is shown on fig. 6.10. Both of this results show a good match and confirm the utility of prepared method.

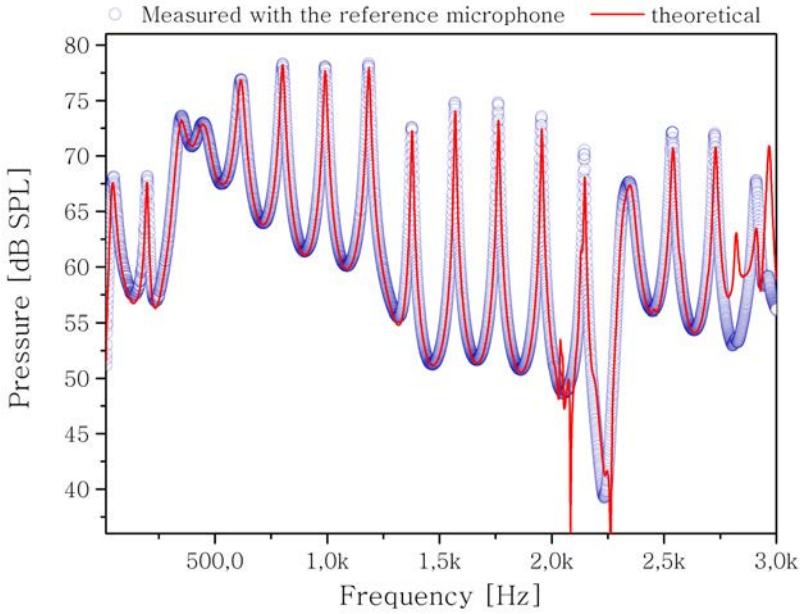

Figure 6.10: Comparison of experimental and identified data for impedance tube setup.

However the data start do diverge from the 2 kHz. In fact the application of impedance tube for frequency response measurements is limited by its diameter (D_{IT}) and the distance between microphones x_1 and x_2:

$$f_{max} < \frac{c_0}{2D_{IT}}, \tag{6.20}$$

$$x_2 - x_1 < \frac{1}{2}\frac{c_0}{f_{max}}. \tag{6.21}$$

The first limitation concerns planar wave propagation criteria (on fig 6.10 we observe the disorders coming from the radial mode starting from 2 kHz) while the second one is set by the Shannon sampling theorem. Nevertheless we will continue the investigations of this method keeping in mind that the high frequency performance can be improved by use of the tube with smaller diameter. The second results show the comparison

between the response of the reference and the MEMS microphones (fig. 6.11). Both microphones were placed at the end of the tube and the measurements were made by the exchange, with equal sound pressure level. The responses of both microphones shows a good match.

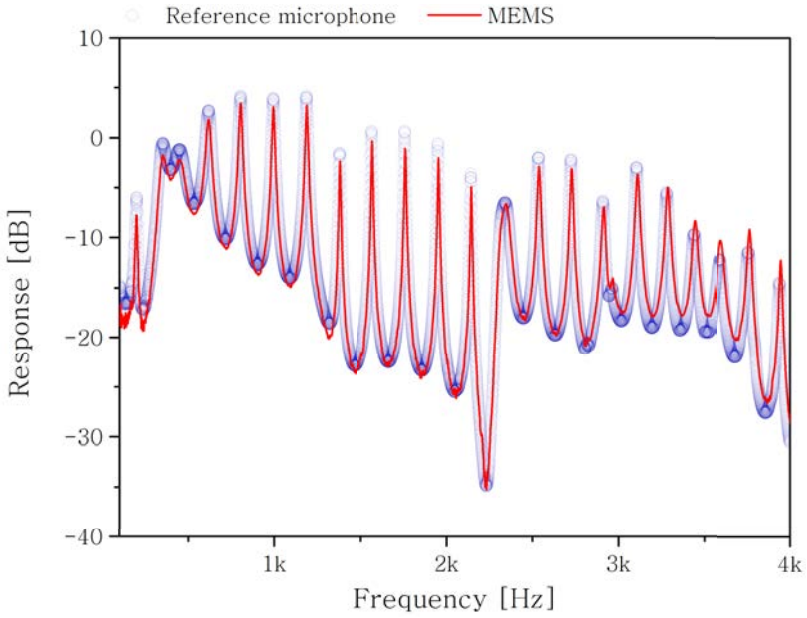

Figure 6.11: Comparison of normalized responses of the reference microphone and the MEMS.

Finally we have prepared the normalized pressure-field response of the MEMS microphone. Figure 6.12 shows the results obtained by the rapport of signal coming from the MEMS and the laboratory microphone placed at the end of the tube (consecutive measurements). This figure corresponds to the low frequency response of the specimen showed on figure 6.2. We may observe the influence of the packaging and approximate the low cut-off by giving the frequency value for -3 dB. We estimate it to be around 70 Hz while the MEMS data sheet gives 100 Hz. Finally the sensitivity of the MEMS microphone has been estimated to -37.4 dBV/Pa which agrees with the datasheet value where the limit values are -41 to -35 dBV/Pa.

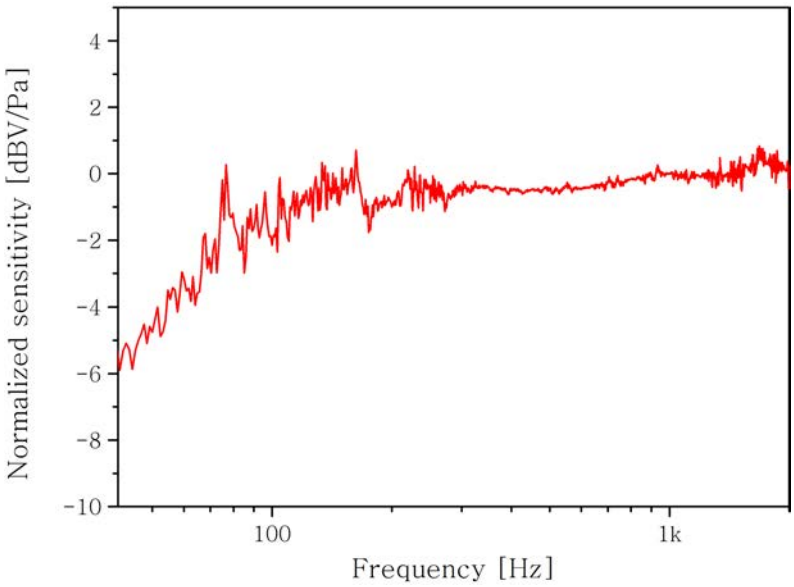

Figure 6.12: Normalized pressure-field response of INMP504ACEZ microphone.

6.5 Free-field investigations in anechoic chamber

We use the anechoic chamber to provide the conditions that are close to the free-field. The experimental set is presented on the figure 6.13; it consists of the loudspeaker, the reference microphone and the MEMS microphone. All the elements are placed on the stands to adjust their vertical positions, then the loudspeaker is placed at a distance of 70 cm from the tested microphones.

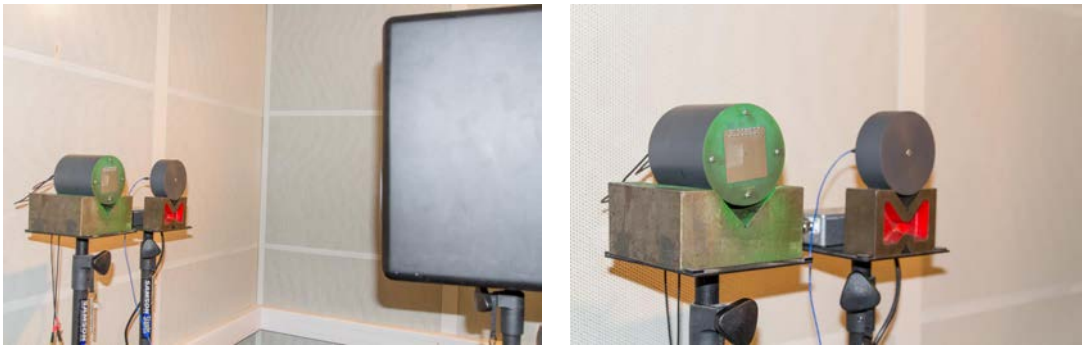

Figure 6.13: Experimental setup used in free-field investigations.

We have compared the frequency response of the reference and the MEMS microphone on figure 6.14. It shows that the MEMS microphone if fully operational. We have estimated the MEMS sensitivity at 1 kHz to -34.8 dBV/Pa. The difference between the sensitivity -37.4 dBV/Pa obtained in impedance tube may come from the experimental setup used in anechoic chamber. To verify it one should prepare the measurements where the reference and the MEMS microphones are tested one after another while placed exactly in the same distance from the loudspeaker to assure the equal sound pressure level.

It is problematic to retrieve the sensitivity of the MEMS microphone over the whole frequency band. Normally it can be done with use of formula 6.3. Nevertheless the

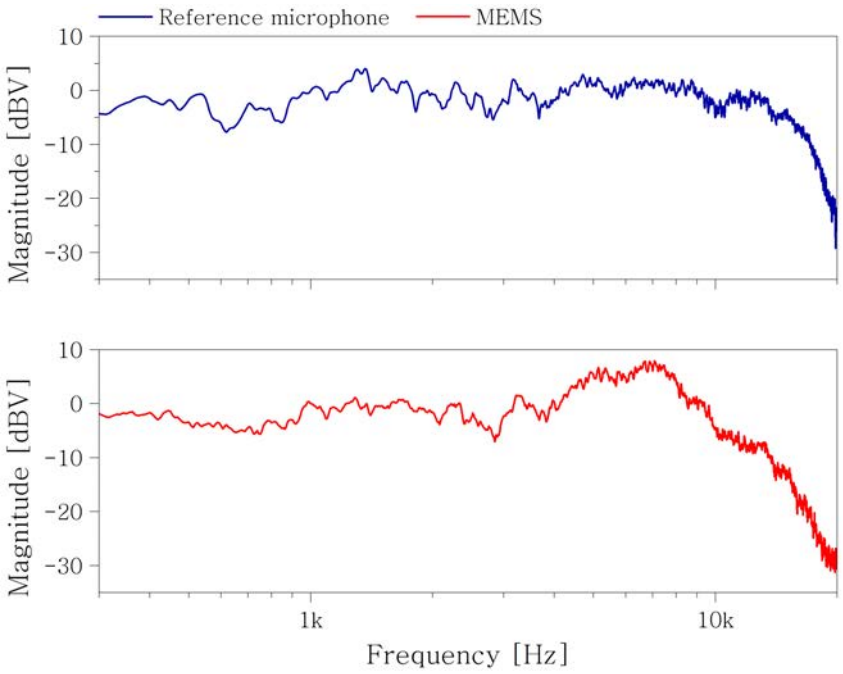

Figure 6.14: Normalized frequency response measured in anechoic chamber.

sensitivity of the reference microphone is calibrated only at 1 kHz and we see that the response of reference microphone is not ideally uniform over the bandwidth. Therefore use of proposed formula can introduce large error in the MEMS microphone sensitivity response, especially between 10 and 20 kHz where the reference microphone response decreases.

Calm environment of anechoic chamber enabled us to analyze the noise of the microphones. In this measurements the loudspeaker was removed from the chamber and the signals presented on the fig. 6.15 results from the inherit noise sources of the microphones. The MEMS noise is higher however we need to remember that this noise is amplified by the discrete electronics. If we suppress the gain of the electronics, the noise decreases (fig. 6.16(a)). Both of the figures (6.16(a) and 6.16(b)) present the noise of MEMS microphones with acoustic signal capacitive detection based on perforated membrane. According to the paper of A. Dehe [26] at low frequencies the noise level is defined by the Flicker noise coming from the ASIC, then the noise level is set by two thermal noises: thermomechanical noise of the membrane and thermoacoustic noise of the membrane perforations.
Moreover the noise measurements unveil the mechanical resonance of the MEMS microphone that for measured microphone occurs close to 7 kHz. It is slightly lower than the value that may be read from the typical frequency response given in the data sheet where the resonance is announced above 10 kHz (fig. 6.2).

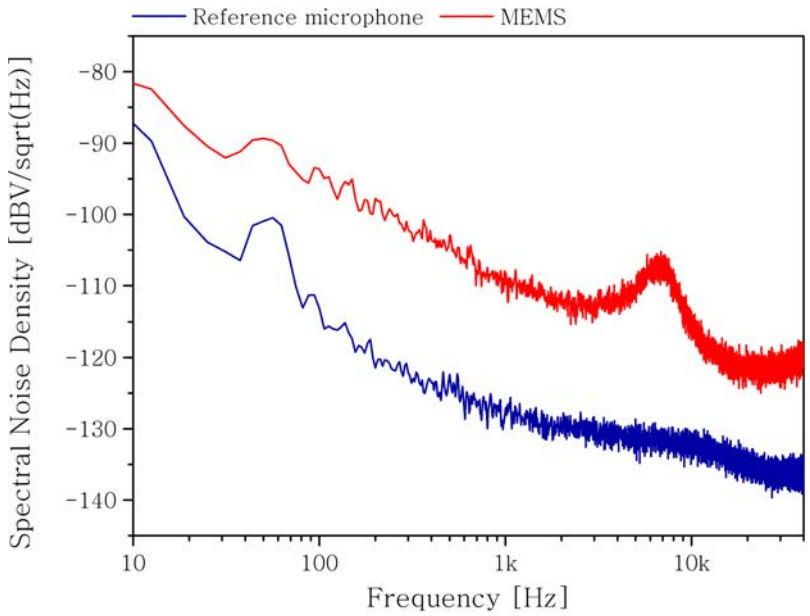

Figure 6.15: Noise spectral density of reference microphone and the MEMS microphone with discrete readout circuit.

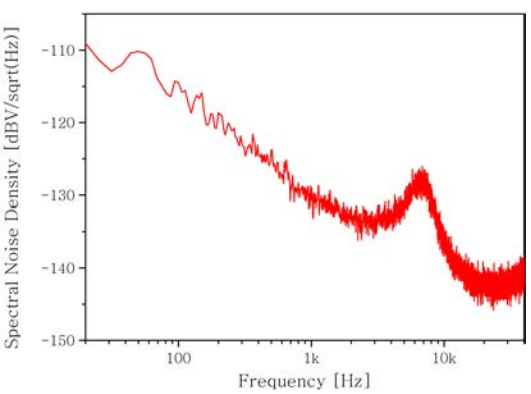

(a) Noise of INMP504ACEZ microphone.

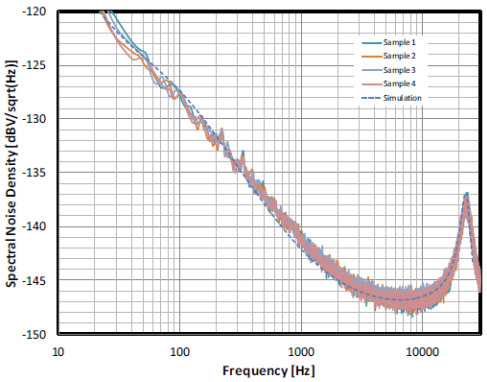

(b) Noise measurements od the Infineon MEMS microphone [26].

Figure 6.16: Comparison of the identified noise with the state of the art example.

Summary

We have selected and validated two methods to extract the crucial characteristics of the MEMS microphone. First method use the impedance tube and it allowed us to trace the low frequency response of the microphone which is shaped by the viscous resistance and the backvolume. The backvolume of used commercial microphone is unknown, however for the future tests of the new prototype we will be able to deduct the viscous resistance of the whole acoustic system of the MEMS and compare it to the one obtained with the FEM and Lumped Elements models. Moreover both pressure-field and free-field characterization techniques allowed us to find the sensitivity of characterized MEMS. Both values: -37.4 and -34.8 dBV/Pa are comparable, however the sensitivity obtained in pressure-field seems to be more reliable and shows good match with -38 dBV/Pa given in the datasheet.
We have managed to measure the noise floor of the MEMS in the anechoic chamber. This measurement gave us additional information on the mechanical resonance of the membrane which is slightly lower comparing to the frequency response given by the manufacturer (measured value is around 7 kHz while in the datasheet the resonance is announced above 10 kHz).

Conclusion and outlook

This work aimed the fabrication of the MEMS microphone for the hearing aids and consumer electronics. Designed microphone is supposed to complement the existing sensor line at the MEMS sensors laboratory at CEA-LETI with particular interest in future fabrication of multi-sensor chips. Realization of this project called the MAD-NEMS was possible with support of the French National Research Agency. Since it was the first microphone realized in the laboratory, this work covered the search for suitable solutions that may be now applied in future work. The work included: the concept considerations, the technological platform, the simulations with acoustical, mechanical and electrical behavior and finally the approaches to the MEMS microphone characterization.

As a result of this work it has been demonstrated that FEA and equivalent circuit representation are the powerful tools for comprehensive design considerations of the MEMS microphone. Both models are complementary and were used to understand the acoustic phenomena at the microscale and the evaluation of noise sources in the sensor respectively. Initial design and the dimensioning of the microphone were prepared basing on the FLNS model with fluid-structure interaction. Afterward we have used the Lumped Element model for the analysis of the noises in the microphone. The frequency response of the microphone obtained with both of the models shows a good match. Despite the high computational cost we have prepared simplified 3D model to verify if 2D representation of the microphone is correct. The sensitivity value obtained with 3D model is in slightly lower than the one obtained with approximative models, however it is in the same scale.

The evaluated performance of the first M&NEMS Microphone prototype can not be squarely compared to the commercial products because we give the specifications of the MEMS dice without the ASIC. Normally the ASIC will amplify the output signal and the sensitivity of designed microphone (-56.4 dBV) will reach the one given by commercial products (typically -38 dBV). The given SNR is much lower than the best results of the commercial and state of the art sensors. We can accept this value for the prototype, however for the future designs this value has to be optimized. M&NEMS technology offers high sensitivity, however the optimization of SNR is challenging in terms of electrical noises of the piezoresistive nanogauge (1/f and Johnson noises) and the thermoacoustic noise generated in small acoustic cavities.

As for the rest of the specifications, it corresponds to the ones of the commercial products. We have been aware that matching all of the specifications to the commercial products is challenging in terms of the sensor design, however our design corresponds to the commercial products in such critical aspects as the power consumption and the overall chip-package size. It is worth mentioning that there are no standard packages available for MEMS microphones and the in-house solution has been prepared.

While the designed microphone is under fabrication, the functional test approach has been developed and validated on a commercial MEMS microphone. Two methods to extract the crucial characteristics of the MEMS microphone have been selected and validated. First method use the impedance tube and it allowed us to trace the low frequency response of the microphone which is shaped by the viscous resistance and the backvolume. The backvolume of used commercial microphone is unknown, however for the future tests of the new prototype we will be able to deduct the viscous resistance of the whole acoustic system of the MEMS and compare it to the one obtained with the FEM and Lumped Elements models. Moreover both pressure-field and free-field characterization techniques allowed us to find the sensitivity of characterized MEMS. Both values: -37.4 and -34.8 dBV/Pa are comparable, however the sensitivity obtained in pressure-field seems to be more reliable and shows good match with -38 dBV/Pa given in the datasheet.

M&NEMS microphone improvement

In order to enable prompt fabrication of the microphone, the prototype which is presented in this work was prepared during the first six months of this thesis. This early design which is not free of errors may be now improved basing on the experience that the author has gathered during a later period. The microfabrication of the designed microphone did not finish due to technological problems, however the overall concept of the microphone seems to be promising and the first prototype that will prove the concept of this new architecture is highly expected.

Design optimization:

- the acoustic system of the MEMS dice should be rearranged in order to be symmetrical (equal overall volume of the inlets and outlets).
- The truss-structured beam has to be very rigid in the vicinity of the microhinge and the nanogauge, however its stiffness might be decreased on the other extremity. Therefore the mass of truss-structured beam may still be decreased by use of the truss members with variable dimensions.
- The angle between the microhinge members may be adjusted to obtain lower angular stiffness of the hinge. In the first design the angle of 30 degrees has been chosen, while for the crystalline Silicon the minimal Young's modulus is obtained for the angle of 45 degrees relative to the <110> crystallographic direction.

Technology optimization:

- the Flicker noise of the nanogauges may be decreased by the optimization of the fabrication process (improvement of Silicon crystal lattice quality).
- The piezoresistive coefficient π_{pzr} might be increased by reduction of nanogauge section or reduction of the doping level.
- Improvement of the DRIE ratio from 20 to 40 can lead to the fabrication of the beam with doubled lateral surface while maintaining low mass.
- Optimization of the epitaxial growth of MEMS layer can lead to lower stress between the NEMS and MEMS layer. With lower stress the out-of-plane deflection will be decreased and longer beams with larger lateral surface might be used.

Appendix A

How COMSOL implements FLNS

Documentation of COMSOL Acoustic module and especially documentation of Thermoacoustic branch [92] do not present the actual implementation of the viscothermal problem. However one can conclude that Comsol use the set of full linearized Navier-Stokes equations (see chapter 3).
Inquisitive COMSOL user may access the exact weak formulation of the problem through the equation view. Therefore we find the set of three weak formulations used in Comsol Thermoacoustic branch (for the sake of simplicity we consider 2D problem):

$$\begin{aligned}0 =&((-2*ta.mu*ux+(2*ta.mu/3-ta.muB)*(ux+vy)+p)*test(ux)\\&-ta.mu*(uy+vx)*test(uy)-ta.mu*(uy+vx)*test(vx)\\&+(-2*ta.mu*vy+(2*ta.mu/3-ta.muB)*(ux+vy)+p)*test(vy)\\&-ta.iomega*ta.rho0*u*test(u)\\&-ta.iomega*ta.rho0*v*test(v))*ta.delta\_ta,\end{aligned} \tag{A.1}$$

$$0 = -(ta.iomega*ta.rho+ta.rho0*(ux+vy))*test(p)*ta.delta\_ta, \tag{A.2}$$

$$\begin{aligned}0 =&(-ta.kcond*(Tx*test(Tx)+Ty*test(Ty))\\&+ta.iomega*(ta.alpha0*ta.T0*p-ta.rho0*ta.Cp*T)*test(T))*ta.delta\_ta.\end{aligned} \tag{A.3}$$

Lets now change the notation to match the one in section 3.3. We see that the foregoing equations correspond respectively to the velocity, pressure and temperature fields:

$$0 = \int_{\mathcal{D}} \left(\overline{\overline{\nabla \mathbf{v}^*}} \colon \bar{\bar{\sigma}}_v + p(\nabla \cdot \mathbf{v}^*) - \left(\rho_0 \frac{\partial \mathbf{v}}{\partial t} \right) \mathbf{v}^* \right) \cdot ta.delta\_ta \, \mathrm{d}V, \tag{A.4}$$

$$0 = \int_{\mathcal{D}} -\left(\frac{\partial \rho}{\partial t} + \rho_0 \left(\nabla \cdot \mathbf{v} \right) \right) p^* \cdot ta.delta\_ta \, \mathrm{d}V, \tag{A.5}$$

$$0 = \int_{\mathcal{D}} \left(-\kappa \nabla \tau + \frac{\partial p}{\partial t} - \rho_0 c_P \frac{\partial \tau}{\partial t} \right) \tau^* \cdot ta.delta\_ta \, \mathrm{d}V, \tag{A.6}$$

the term $ta.delta\_ta$ has been introduced by COMSOL as a scaling factor and it denotes $1/(j\omega)$.

Bibliography

[1] G.W. Elko and K.P. Harney. A history of consumer microphones: The electret condenser microphone meets micro-electro-mechanical-systems. *Acoustic Today*, 5:4–13, 2009.

[2] E.W. Siemens. Improvement in magneto-electric aparatus, 1874.

[3] T.A. Edison. Speaking telegraph, 1879.

[4] E.C. Wente. A condenser transmitter as a uniformly sensitive instrument for the absolute measurement of sound intensity. *Physical Review*, 10(1):39–63, 1917.

[5] G.M. Sessler and J.E. West. Self-biased condenser microphone with high capacitance. *The Journal of the Acoustical Society of America*, 34:1787–1788, 1962.

[6] D. Hohm and G. Sessler. Kapazitive wandler auf siliziumbasis mit siliziumdioxid-elektret (silicon-based capacitive transducer with silicon dioxide electret), 1983.

[7] A.G. Bell. Improvement in telegraphy, 1876.

[8] J. Lewis. Understanding microphone sensitivity. *Analog Dialogue*, 46(2):14–16, 2012.

[9] J. Lewis. *Microphone specifications explained.* Analog Devices. Application Note AN-1112.

[10] Microphone handbook vol.1. Technical report, Brüel & Kjær, 1996.

[11] Knowles Electronics. *Zero-Height SiSonic^{TM}Microphone With Enhanced RF Protection.*

[12] F.A. Everest and K.C. Pohlmann. *Master Handbook of Acoustic.* McGraw-Hill, 2009.

[13] S. Temme. *Audio Distortion Measurements.* Brüel & Kjær. Application Note.

[14] F. Laermer and A. Schilp. Method of anisotropically etching silicon, 03 1996.

[15] F. Laermer and A. Schilp. Method of anisotropically etching of silicon, 03 2003.

[16] R. Fraux. Knowles SPU0410LR5H MEMS microphone - reverse costing analysis. Technical report, System Plus Consulting, 2011.

[17] Y.B. Ning, A.W. Mitchell, and R.N. Tait. Fabrication of a silicon micromachined capacitive microphone using a dry-etch process. *Sensors and Actuators A: Physical*, 53(1–3):237 – 242, 1996. Proceedings of The 8th International Conference on Solid-State Sensors and Actuators.

[18] W. Kronast, B. Muller, W. Siedel, and A. Stoffel. Single-chip condenser microphone using porous silicon as sacrificial layer for the air gap. *Sensors and Actuators A: Physical*, 87(3):188 – 193, 2001.

[19] M.L. Kuntzman, C.T. Garcia, A.G. Onaran, B. Avenson, K.D. Kirk, and N.A. Hall. Performance and modeling of a fully packaged micromachined optical microphone. *Microelectromechanical Systems, Journal of*, 20(4):828–833, 2011.

[20] P. Rombach, M. Mullenborn, U. Klein, and K. Rasmussen. The first low voltage, low noise differential silicon microphone, technology development and measurement results. *Sensors and Actuators A: Physical*, 95(2–3):196 – 201, 2002. Papers from the Proceedings of the 14th IEEE Internat. Conf. on MicroElectroMechanical Systems.

[21] A. Torkkeli, O. Rusanen, J. Saarilahti, H. Seppä, H. Sipola, and J. Hietanen. Capacitive microphone with low-stress polysilicon membrane and high-stress polysilicon backplate. *Sensors and Actuators A: Physical*, 85(1–3):116 – 123, 2000.

[22] J.W. Weigold, T.J. Brosnihan, J. Bergeron, and X. Zhang. A MEMS condenser microphone for consumer applications. In *Micro Electro Mechanical Systems, 2006. MEMS 2006 Istanbul. 19th IEEE International Conference on*, pages 86–89, 2006.

[23] A. Dehe. Silicon microphone development and application. *Sensors and Actuators A: Physical*, 133(2):283 – 287, 2007. Selected Papers from the 9th International Conference on Materials for Advanced Technologies.

[24] T. Kasai, S. Sato, S. Conti, I. Padovani, F. David, Y. Uchida, T. Takahashi, and H. Nishio. Novel concept for a MEMS microphone with dual channels for an ultra-wide dynamic range. In *Micro Electro Mechanical Systems (MEMS), 2011 IEEE 24th International Conference on*, pages 605–608, 2011.

[25] Chun-Kai Chan, Wei-Cheng Lai, Mingching Wu, Ming-Yung Wang, and Weileun Fang. Design and implementation of a capacitive-type microphone with rigid diaphragm and flexible spring using the two poly silicon micromachining processes. *Sensors Journal, IEEE*, 11(10):2365–2371, 2011.

[26] A. Dehe, M. Wurzer, M. Fuldner, and U. Krumbein. The Infineon silicon MEMS microphone. In *Proceedings SENSOR 2013*, pages 95–99, 2013.

[27] Yoshinori Iguchi, Masahide Goto, Masakazu Iwaki, Akio Ando, Kenkichi Tanioka, Toshifumi Tajima, Futoshi Takeshi, Susumu Matsunaga, and Yoshinobu Yasuno. Silicon microphone with wide frequency range and high linearity. *Sensors and Actuators A: Physical*, 135(2):420 – 425, 2007.

[28] M. Mullenborn, P. Rombach, U. Klein, K. Rasmussen, J.F. Kuhmann, M. Heschel, M.Amskov Gravad, J. Janting, J. Branebjerg, A.C. Hoogerwerf, and S. Bouwstra. Chip-size-packaged silicon microphones. *Sensors and Actuators A: Physical*, 92(1–3):23 – 29, 2001. Selected Papers for Eurosensors XIV.

[29] J.J. Neumann Jr. and K.J. Gabriel. A fully-integrated CMOS-MEMS audio microphone. In *TRANSDUCERS, Solid-State Sensors, Actuators and Microsystems, 12th International Conference on, 2003*, volume 1, pages 230–233, 2003.

[30] G.W. Elko, F. Pardo, D. Lopez, D. Bishop, and P. Gammel. Capacitive MEMS microphones. *Bell Labs Technical Journal*, 10(3):187–198, 2005.

[31] Cheng-Ta Chiang and Chia-Yu Wu. A CMOS digitized silicon condenser microphone for acoustic applications. *Sensors Journal, IEEE*, 11(2):296–304, 2011.

[32] M. Sheplak, J.M. Seiner, K.S. Breuer, and M.A. Schmidt. A MEMS microphone for aeroacoustics measurements. In *37th AIAA Aerospace Sciences Meeting & Exhibit, AIAA Paper 99-0606*, Reno, NV, January 1999.

[33] M.D. Williams, B.A. Griffin, T.N. Reagan, J.R. Underbrink, and M. Sheplak. An AlN MEMS piezoelectric microphone for aeroacoustic applications. *Microelectromechanical Systems, Journal of*, 21(2):270–283, 2012.

[34] P. Robert and A. Walther. MEMS dynamic pressure sensor, in particular for applications to microphone production, 06 2011.

[35] V. Rochus. *Finite Element Modelling of Strong Electro-Mechanical Coupling in MEMS*. PhD thesis, The University of Liege, Faculty of Applied Sciences, 2006.

[36] Chien-Hung Wu, C.A. Zorman, and M. Mehregany. Fabrication and testing of bulk micromachined silicon carbide piezoresistive pressure sensors for high temperature applications. *Sensors Journal, IEEE*, 6(2):316–324, April 2006.

[37] C. Liu. *Foundations of MEMS*. Pearson Prentice Hall, 2006.

[38] A.A. Barlian, Woo-Tae Park, J.R. Mallon, A.J. Rastegar, and B.L. Pruitt. Review: Semiconductor piezoresistance for microsystems. *Proceedings of the IEEE*, 97(3):513–552, March 2009.

[39] G. Blazquez, P. Pons, and A. Boukabache. Capabilities and limits of silicon pressure sensors. *Sensors and Actuators*, 17(3–4):387 – 403, 1989.

[40] R.H. Johnson, S. Karbassi, U. Sridhar, and B. Speldrich. A high-sensitivity ribbed and bossed pressure transducer. *Sensors and Actuators A: Physical*, 35(2):93 – 99, 1992.

[41] Ahmed A S Mohammed, Walied A Moussa, and Edmond Lou. Optimization of geometric characteristics to improve sensing performance of mems piezoresistive strain sensors. *Journal of Micromechanics and Microengineering*, 20(1):015015, 2010.

[42] Sea-Chung Kim and K.D. Wise. Temperature sensitivity in silicon piezoresistive pressure transducers. *Electron Devices, IEEE Transactions on*, 30(7):802–810, Jul 1983.

[43] Yi Cai Sun, Zhenbin Gao, Li Qiang Tian, and Yi Zhang. Modelling of the reverse current and its effects on the thermal drift of the offset voltage for piezoresistive pressure sensors. *Sensors and Actuators A: Physical*, 116(1):125 – 132, 2004.

[44] Rongrui He and Peidong Yang. Giant piezoresistance effect in silicon nanowires. *Nature Nanotechnology*, 1:42–46, Oct 2006.

[45] W. Kester. *Practical design techniques for sensor signal conditioning*. Analog Devices.

[46] D. Ettelt. *Conception et fabrication d'un magnétomètre à jauge de contrainte*. PhD thesis, Université de Grenoble, 2012.

[47] Y. Deimerly. *Vers des centrales inertielles compactes basées sur des nanojauges piezorésistives : problématique de co-intégration*. PhD thesis, Université Paris-Est, 2013.

[48] P. Robert, V. Nguyen, S. Hentz, L. Duraffourg, G. Jourdan, J. Arcamone, and S. Harrisson. M&NEMS: A new approach for ultra-low cost 3d inertial sensor. In *Sensors, 2009 IEEE*, pages 963–966, Oct 2009.

[49] D. Ettelt, P. Rey, M. Savoye, C. Coutier, M. Cartier, O. Redon, M. Audoin, A. Walther, P. Robert, Y. Zhang, F. Dumas-Bouchiat, N. M. Dempsey, and J. Delamare. A new low consumption 3d compass using integrated magnets and piezoresistive nano-gauges. In *Solid-State Sensors, Actuators and Microsystems Conference (TRANSDUCERS), 2011 16th International*, pages 40–43, June 2011.

[50] D. Ettelt, P. Rey, G. Jourdan, A. Walther, P. Robert, and J. Delamare. 3d magnetic field sensor concept for use in inertial measurement units (imus). *Microelectromechanical Systems, Journal of*, PP(99):1–1, 2013.

[51] A. Walther, M. Savoye, G. Jourdan, P. Renaux, F. Souchon, P. Robert, C. Le Blanc, N. Delorme, O. Gigan, and C. Lejuste. 3-axis gyroscope with si nanogage piezoresistive detection. In *Micro Electro Mechanical Systems (MEMS), 2012 IEEE 25th International Conference on*, pages 480–483, Jan 2012.

[52] A. Walther, C. Le Blanc, N. Delorme, Y. Deimerly, R. Anciant, and J. Willemin. Bias contributions in a mems tuning fork gyroscope. *Microelectromechanical Systems, Journal of*, 22(2):303–308, April 2013.

[53] Y. Deimerly, P. Robert, G. Jourdan, P. Rey, and T. Bourouina. Ultra-compact absolute pressure sensor based on mechanical amplification coupled to a suspended piezoresistive nanogauge. In *Solid-State Sensors, Actuators and Microsystems (TRANSDUCERS EUROSENSORS XXVII), 2013 Transducers Eurosensors XXVII: The 17th International Conference on*, pages 1767–1770, June 2013.

[54] M. Bruneau. *Manuel d'acoustique fondamentale*. Hermes, 1998.

[55] A.D. Pierce. *Acoustics: An Introduction to Its Physical Principles and Applications*. Acoustical Society of America, 1989.

[56] W.R. Kampinga. *Viscothermal acoustics using finite elements : analysis tools for engineers*. PhD thesis, Enschede, June 2010.

[57] A. Lallemand. Écoulement des fluides dynamique des fluides réels. *Techniques de l'ingénieur Fluides et combustion*, base documentaire : TIB213DUO.(ref. article : be8157), 2014. fre.

[58] N. Joly. Finite element modeling of thermoviscous acoustics on adapted anisotropic meshes: Implementation of the particle velocity and temperature variation formulation. *Acta Acustica united with Acustica*, 96(1):102–114, January 2010.

[59] W.R. Kampinga, Y.H. Wijnant, and A. de Boer. Performance of several viscothermal acoustic finite elements. *Acta Acustica united with Acustica*, 96:115 – 124, 2010.

[60] O.C. Zienkiewicz, R.L. Taylor, and P. Nithiarasu. *The Finite Element Method for Fluid Dynamics (Sixth Edition)*. Butterworth-Heinemann, 2005.

[61] C. Guianvarc'h, T. Verdot, J. Czarny, E. Redon, K. Ege, J.-L. Guyader, A. Walther, and P. Robert. New planar nano-gauge detection microphone: analytical and numerical acoustic modeling. *Proceedings of International Congress on Acoustics*, 19(1):–, 2013.

[62] T. Verdot, C. Guianvarc'h, J. Czarny, E. Redon, K. Ege, and J.L. Guyader. Modélisation d'une architecture innovante de microphone MEMS à détection par nano jauges. In *Actes du XXIe Congrès Français de Mécanique, CFM2013*, Bordeaux, France, 2013.

[63] Comsol. *Comsol Multiphysics, Reference Manual: Equation-Based Modeling*.

[64] N. Joly, M. Bruneau, and R. Bossart. Coupled equations for particle velocity and temperature variation as the fundamental formulation of linear acoustics in thermoviscous fluids at rest. *Acta Acustica united with Acustica*, 92:202–209, 2006.

[65] N. Joly and Durand S. Modélisation numérique de l'acoustique en fluides thermovisqueux: application à l'étude de micro-systèmes. *18ème Congrès Français de Mécanique, Grenoble, 27-31 août 2007*, 2007.

[66] H. Tijdeman. On the propagation of sound waves in cylindrical tubes. *Journal of Sound and Vibration*, 39(1):1 – 33, 1975.

[67] W.M. Beltman. Viscothermal wave propagation including acousto-elastic interaction, part I: Theory. *Journal of Sound and Vibration*, 227(3):555 – 586, 1999.

[68] Joel Voldman. Course materials for 6.777J / 2.372J Design and Fabrication of Microelectromechanical Devices, Spring 2007. MIT OpenCourseWare (http://ocw.mit.edu/).

[69] S. Adhikari. *Damping Models for Structural Vibration*. PhD thesis, Cambridge University, Engineering Department, 2000.

[70] A. Preumont. *Vibration Control of Active Structures*. Springer, 2011.

[71] T.B. Gabrielson. Fundamental noise limits in miniature acoustic and vibration sensors. Report, Naval Air Development Center, Dec 1991.

[72] T.B. Gabrielson. Mechanical-thermal noise in micromachined acoustic and vibration sensors. *Electron Devices, IEEE Transactions on*, 40(5):903–909, May 1993.

[73] F.N. Hooge. 1/f noise is no surface effect. *Physics Letters A*, 29(3):139 – 140, 1969.

[74] F. N. Hooge. 1/f noise sources. *Electron Devices, IEEE Transactions on*, 41(11):1926–1935, Nov 1994.

[75] P.Y. Kwok, M.S. Weinberg, and K.S. Breuer. Fluid effects in vibrating micromachined structures. *Microelectromechanical Systems, Journal of*, 14(4):770–781, Aug 2005.

[76] Y.B. Gianchandani, O. Tabata, and H.P. Zappe. *Comprehensive Microsystems*, volume 1 of *Comprehensive Microsystems*. Elsevier Science & Technology Books, 2007.

[77] J. Meng, T. Mattila, A Dasgupta, M. Sillanpaa, R. Jaakkola, K. Andersson, and E. Hussa. Testing and multi-scale modeling of drop and impact loading of complex mems microphone assemblies. In *Thermal, Mechanical and Multi-Physics Simulation and Experiments in Microelectronics and Microsystems (EuroSimE), 2012 13th International Conference on*, pages 1/8–8/8, April 2012.

[78] J. Li, J. Makkonen, M. Broas, J. Hokka, T.T. Mattila, M. Paulasto-Krockel, J. Meng, and A DasGupta. Reliability assessment of a mems microphone under shock impact loading. In *Thermal, Mechanical and Multi-Physics Simulation and Experiments in Microelectronics and Microsystems (EuroSimE), 2013 14th International Conference on*, pages 1–6, April 2013.

[79] Jing en Luan and Tong Yan Tee. Effect of impact pulse parameters on consistency of board level drop test and dynamic responses. In *Electronic Components and Technology Conference, 2005. Proceedings. 55th*, pages 665–673 Vol. 1, May 2005.

[80] M. Sahmimi. Epcos T4060 MEMS microphone - reverse costing analysis. Technical report, System Plus Consulting, 2012.

[81] S. Hallereau. Epcos T4000 MEMS microphone - reverse costing analysis. Technical report, System Plus Consulting, 2011.

[82] R. Fraux. Akustica AKU230 MEMS microphone - reverse costing analysis. Technical report, System Plus Consulting, 2011.

[83] *http://www.eurocircuits.com/index.php/technology-guidelines/pcb-panel-guidelines/94-how-to-panelise-small-pcbs.*

[84] *http://www.multi-circuit-boards.eu/en/pcb-design-aid/design-parameters.html.*

[85] S. Stafford. Avoid overlooking depaneling step in the PCB manufacturing process. *Electronic Products and Technology*, Dec 2013.

[86] R. Barham, S. Barrera-Figueroa, and J.E.M. Avison. Secondary pressure calibration of measurement microphones. *Metrologia*, 51(3):129, 2014.

[87] V. Nedzelnitsky. Calibration of pressure and gradient microphones. In *Encyclopedia of Acoustics*, pages 1869–1879. John Wiley & Sons, Inc., 2007.

[88] E. Frederiksen. Microphone calibration. In *Handbook of Signal Processing in Acoustics*, pages 1293–1312. Springer New York, 2008.

[89] L.L. Beranek. *Acoustic measurements.* John Wiley & Sons, Inc., 1949.

[90] *Ultra-Low Noise Microphone with Bottom Port and Analog Output.* INMP504 MEMS microphone datasheet.

[91] C.E. Shannon. Communication in the presence of noise. *Proceedings of the IEEE*, 86(2):447–457, Feb 1998.

[92] Comsol. *Acoustics Module, User's Guide: Theory Background for the Thermoacoustic Branch.*